Universität Rostock

Traditio et Innovatio

Particle acceleration at collisionless shocks

Hybrid Simulations in the Era of High-Precision Cosmic Ray Observations

Dissertation

zur Erlangung des akademischen Grades

doctor rerum naturalium (Dr. rer. nat.)

der Mathematisch-Naturwissenschaftlichen Fakultät

der Universität Rostock

Vorgelegt von: Adrian Hanusch

Geboren am: 30.01.1992 in Berlin

Rostock: 19. Mai 2020

Mathematisch-Naturwissenschaftliche Fakultät

Abstract

The question of cosmic ray (CR) origin has captivated physicists for more than a hundred years. Already in 1934, shortly after the discovery of these highly energetic particles, W. Baade and F. Zwicky concluded that only extreme astrophysical events such as supernovae could be potential sources. This hypothesis was encouraged in the 1970s when the theory of diffusive shock acceleration (DSA) was developed, which predicts particle energization, potentially up to 10^{15} eV, at supernova remnant (SNR) shocks. While the DSA is remarkably insensitive to many shock parameters and able to predict the general shape of the cosmic ray spectra, there are several aspects that remain unsolved. One serious challenge is connected to the initial phase of the acceleration, the so-called "injection", which is still not fully understood. Additionally, the recent high-precision measurements of CR spectra have revealed features that are not accounted for by the "standard" DSA theory, not to mention, that anomalies in the CR spectra and composition are becoming a general trend in modern CR observations.

The interplay between observations, theory, and much improved numerical simulations gives further insights into the physics of cosmic rays and the physics of injection in particular by disentangling the processes at work. However, as the numerical simulations approach more realistic conditions, their physical understanding becomes more challenging as well. The foundation of the theoretical work presented in this thesis is the application of advanced numerical methods in the form of a hybrid code, in which the ion component is described kinetically while the electrons are treated as a charge neutralizing fluid. Simulations of nonrelativistic collisionless shocks have been carried out with a focus on particle injection into the DSA. The studies can be divided into three research topics: (i) specific elemental selectivity of the initial phase of the DSA; (ii) steepening of CR spectra in shocks with varying magnetic field direction; (iii) energization of electrons at quasi-parallel shocks. The first two items are directly related to the "anomalies" in the CR spectra revealed by the recent precise measurements of galactic CRs. These are a remarkable difference between the rigidity spectral indices of protons and helium ions as well as significantly steeper CR spectra with respect to the "standard" DSA theory predictions. The last item is devoted to the notoriously difficult problem of the *electron* injection into the DSA and to the exploration of the possibility, that protons accelerated to high energies create sufficient wave turbulence necessary for the electron injection.

Zusammenfassung

Die Suche nach dem Ursprung der kosmischen Strahlung (cosmic rays, CRs) fesselt Wissenschaftler seit mehr als einhundert Jahren. Bereits kurz nach der Entdeckung dieser hochenergetischen geladenen Teilchen folgerten W. Baade und F. Zwicky, dass nur extreme astrophysikaliche Ereignisse, wie etwa Supernovae, als Ursprung infrage kommen können. Diese These wurde Ende der 1970er Jahr durch die Entwicklung der Theorie der "diffusiven Stoßwellenbeschleunigung" (diffusive shock acceleration, DSA) bestärkt. Nach dieser Theorie können Ionen an den Stoßwellen von Supernovaüberresten zu hohen Energien, möglicherweise bis zu 10^{15} eV, beschleunigt werden. Während die Theorie unempfindlich gegenüber den genauen Bedingungen in diesen Stoßwellen ist und Aussagen über die allgemeine Form der zu erwartenden Energiespektren der kosmischen Strahlung erlaubt, bleiben einige Aspekte ungelöst. Insbesondere die Anfangsphase der Beschleunigung ist noch nicht vollständig verstanden. Weiterhin zeigen sich durch die immer genauer werdenden Beobachtungen Besonderheiten in den Spektren (Dies ist inzwischen ein allgemeiner Trend bei hochpräziesen modernen Messungen). Diese Anomalien erweisen sich zum Teil als Herausforderung für die DSA-Theorie.

Das Zusammenspiel von Beobachtungen, Theorie und verbesserten Simulationen erlaubt neue Erkenntnisse über die kosmische Strahlung und ihre Entstehung zu gewinnen. Je mehr sich die numerischen Simulationen jedoch realistischen Bedingungen nähern, desto schwieriger wird es auch sie zu verstehen und die zugrunde liegenden physikalischen Prozesse zu identifizieren. Die Interpretation von heutigen Simulationen ist daher nicht unbedingt einfacher als die von realen Beobachtungen. Die Grundlage der hier vorgestellten theoretischen Arbeit, liegt in der Anwendung moderner numerischer Methoden, in Form eines hybriden Simulationscodes, in dem die Ionen kinetisch betrachtet werden, während die elektronische Plasmakomponente als ladungsneutralisierendes Fluid beschrieben wird. Im Rahmen der Untersuchungen wurden Simulationen von nicht-relativistischen, kollisionsfreien Stoßwellen mit einem Fokus auf die Teilcheninjektion in die DSA durchgeführt. Insgesamt kann die Arbeit in drei Schwerpunkte unterteilt werden: (i) Abhängigkeit der Anfangsphase der DSA vom Masse-zu-Landungs Verhältnis; (ii) Einfluss von Stoßwellen mit variabler Ausrichtung des magnetischen Feldes auf den Anstieg der Energiespektren der kosmischen Strahlung; (iii) Beschleunigung von Elektronen an quasi-parallelen Stoßwellen. Die ersten beiden Punkte stehen in direktem Zusammenhang mit "Anomalien" in den CR-Spektren, die durch die jüngsten präzisen Messungen galaktischer CRs aufgedeckt wurden. Dies sind ein bemerkenswerter Unterschied zwischen den Spektren von Protonen und Heliumionen sowie deutlich steilere Spektren verglichen mit den "Standard"-Vorhersagen der DSA-Theorie. Der letzte Punkt ist dem schwierigen Problem der Elektroneninjektion in die DSA und der Erforschung der Möglichkeit gewidmet, dass auf hohe Energien beschleunigte Protonen genügend Turbulenz erzeugen, die für die Elektroneninjektion notwendig ist.

Publications in peer-reviewed journals

- **A. Hanusch**, T. Liseykina, and M. Malkov, *Acceleration of Cosmic Rays in Supernova Shocks: elemental selectivity of the injection mechanism*, Astrophysical Journal 872, 108 (2019) [arXiv:1803.00428]

- **A. Hanusch**, T. V. Liseykina, M. Malkov, and F. Aharonian, *Steepening of Cosmic Ray Spectra in Shocks with Varying Magnetic Field Direction*, Astrophysical Journal 885, 11 (2019) [arXiv:1907.09226]

- **A. Hanusch**, T. Liseykina, and M. Malkov, *Chemistry of ion injection in supernova remnant shocks: hybrid simulations in the light of He/C/O data from AMS-02*, Journal of Physics: Conference Series 1336, 012010 (2019)

- **A. Hanusch**, T. Liseykina, and M. Malkov, *Electron energization in quasi-parallel shocks - Test-particle electrons in a proton-driven turbulence*, Astronomy & Astrophysics, 642, A47 (2020) [arXiv:2007.06478]

Additional publications which are not related to the work presented in this thesis:

- **A. Hanusch**, J. Rapp, M. Brics, and D. Bauer, *Time-dependent renormalized-natural-orbital theory applied to laser-driven H_2^+*, Phys. Rev. A 93, 043414 (2016)

Other publications

- **A. Hanusch**, T. Liseykina, and M. Malkov, *Anomalies in Cosmic Ray Composition: Explanation Based on Mass to Charge Ratio*, 35th International Cosmic Ray Conference; Proceedings of Science 301, PoS(ICRC2017)260; (2017)
DOI: https://doi.org/10.22323/1.301.0260

- **A. Hanusch**, T. V. Liseykina, M. Malkov, *Electron Injection into Fermi Acceleration in Quasiparallel Collisionless Shocks: Combining Hybrid Simulations with Test Particle Acceleration*, 36th International Cosmic Ray Conference; Proceedings of Science 358, PoS(ICRC2019)338; (2019)
https://pos.sissa.it/358/338/

- **A. Hanusch**, T. Liseykina, and M. Malkov, *Mass to charge dependence of particle injection into DSA* 45th EPS Conference on Plasma Physics, EPS 2018, pp. 1392-1395

Conference talks and seminars

- **A. Hanusch**, M. Malkov, T. Liseykina, *Proton and Helium Injection Into First Order Fermi Acceleration at Shocks: Hybrid Simulation and Analysis*, DPG Spring Meeting 2017 Bremen, March 13-17

- **A. Hanusch**, *Anomalies in Cosmic Ray Composition: Explanation Based on Mass to Charge Ratio*, AMCP-Seminar, Universität Rostock, June 13th 2017

- **A. Hanusch**, T. Liseykina, M. Malkov, *Anomalies in Cosmic Ray Composition: Explanation Based on Mass to Charge Ratio*, 35th International Cosmic Ray Conference 2017(ICRC2017), Busan, South Korea, July 12-20

- **A. Hanusch**, T. Liseykina, M. Malkov, *Acceleration of Cosmic Rays in Supernova Shocks: mass to charge selectivity,* DPG Spring Meeting 2018 (SAMOP) Erlangen, March 4-9

- **A. Hanusch**, T. Liseykina, M. Malkov, *Acceleration of Cosmic Rays in Supernova Remnant Shocks: mass to charge selectivity,* COSPAR 2018, Pasadena, USA, July 14-22

- **A. Hanusch**, *Chemistry of ion injection in SNR shocks: hybrid simulations in the light of He/C/O data from AMS-02,* Leibniz-Institut für Astrophysik Potsdam, Seminar "Recent results in theoretical Astroparticle Physics", 29.04.2019

- **A. Hanusch**, T. Liseykina, M. Malkov, F. Aharonian, *Spot-like Proton Acceleration in Supernova Remnant Shocks: Implications for the Energy Spectra*, EPS 2020 Plasma Physics, Sitges, Spain, June 22-26 (scheduled as invited talk, the conference has been postponed to 2021)

Other Conference Contributions

- A. Hanusch, T. Liseykina, *Modelling of ion-acoustic shocks with reflected ions*, 58th Annual Meeting of the APS Division of Plasma Physics, San Jose, California, October 31–November 4 2016;

- A. Hanusch, M. Malkov, R. Sagdeev, T. Liseykina, *Proton and Helium Injection Into First Order FermiAcceleration at Shocks: Hybrid Simulation and Analysis*, 58th Annual Meeting of the APS Division of Plasma Physics, San Jose, California, October 31–November 4 2016;

- A. Hanusch, T. Liseykina, M. Malkov, *Mass to charge dependence of particle injection into DSA*, 45th EPS Conference on Plasma Physics, Prague, Czech Republic, July 2-6 2018

- A. Hanusch, T. Liseykina, M. Malkov, *Electron-Ion Temperature Ratio in Collisionless Shocks*, DPG Spring Meeting 2019 (SMuK) München, March 17-22

- A. Hanusch, T. Liseykina, M. Malkov, *Electron Injection into Fermi Acceleration in Quasiparallel Collisionless Shocks: Combining Hybrid Simulations with Test Particle Acceleration*, 36th International Cosmic Ray Conference 2019 (ICRC2019), Madison, USA, July 12-20 2019

- T. Liseykina, A. Hanusch, M. Malkov and F. Aharonian, *Spot-like Proton Acceleration in SNR Shocks: Implications for the Energy Spectra*, 36th International Cosmic Ray Conference 2019 (ICRC2019), Madison, USA, July 12-20 2019

CONTENTS

Abbreviations

CR	Cosmic ray
DSA	Diffusive shock acceleration
ISM	Interstellar medium
MHD	Magneto-hydrodynamic
MPI	Message Passing Interface
NLDSA	Non-linear diffusive shock acceleration
PIC	Particle-in-cell
SDA	Shock drift acceleration
SN	Supernova
SNR	Supernova remnant
SSA	Shock surfing acceleration
UHECR	Ultra-high-energy cosmic ray

List of Figures

LIST OF TABLES

CHAPTER 1

INTRODUCTION

In order to make further progress, particularly in the field of cosmic rays, it will be necessary to apply all our resources and apparatus simultaneously and side-by-side.

— Victor Hess, Nobel Lecture, 1936

These words from the lecture given by Victor Hess during the awarding of the Nobel prize in physics for the discovery of cosmic rays (CRs) show that the collaboration of different experiments and methods was deemed important already in the early days of the CR observations.

From the early experiments with simple detectors onboard of balloons [1] the measurements of cosmic rays have evolved to intricate observations either with balloon-borne detectors [2, 3, 4] or even space based instruments [5, 6, 7] allowing to measure element-specific energy spectra with high accuracy [8, 9]. Additionally, the highest energy CRs are observed by ground based detectors that measure the secondary particles and radiation that are created when an energetic ion interacts with the atoms and molecules in the atmosphere [10, 11]. Today, we live in an era of multi-messenger astrophysics [12], which has also become noticeable in CR observation. For example, the CR measurements are supported by neutrino detection from the IceCube experiment [13, 14][1]. Further information can be gained from multi-wavelength observations of putative[2] CR acceleration sites [17]. The combination of observations of CRs, neutrinos and electromagnetic radiation has yielded a much clearer picture of CR acceleration than in the early days of Hess. However, what has been probably beyond Hess' imagination, but became possible due to the development of powerful computers, is that besides experiments and theoretical considerations also numerical simulations can greatly contribute to the progress in the field of cosmic rays.

Observations as well as theoretical considerations strongly support the popular hypothesis that galactic CRs are accelerated at supernova remnant (SNR) shocks. Turning to the possible mechanisms of their production, observations favor the diffusive shock acceleration (DSA) [18, 19, 20, 21, 22], a modern development of a theory in the spirit of Fermi's initial idea of CR energization. The basic version of the DSA theory is remarkably

---

[1]   IceCube is more important in the range of ultra-high-energy cosmic ray (UHECR), which are not considered in this thesis. However, recent observations of the background CR anisotropy by Milagro and IceCube [15, 16] are also instrumental in understanding particle escape and propagation from supernova remnants (SNRs) and thus for establishing the connection of these particles with their accelerators.

[2]   Generally, it is impossible to trace CRs back to their accelerators because magnetic fields deflect the particles as they race across the galaxy, and this interaction scrambles their paths and masks their origins.

insensitive to most shock parameters. It is able to explain the acceleration and predicts a power-law spectrum in momentum (p), $f \propto p^{-q}$, where the index, $q = 3r/(r-1)$, depends only on the shock compression, r. According to the DSA, the charged particles gain energy while being scattered by converging plasma flows upstream and downstream of SNR shocks. While this mechanism is conceptually simple and robust, its precise outcome for the energy spectra and chemical composition of accelerated particles is difficult to determine under realistic shock conditions, see, e.g., [23, 24]. In particular, the initial part of the acceleration, i.e., the "injection" of different species into the DSA remains largely unsolved. Injection is a complicated process whereby the shock selects a tiny fraction of particles to keep on crossing its front and gain more energy. It ensures a smooth transition between the thermal plasma and the power-law spectrum at high energies. Modern, revolutionary improved observations, while answering important questions, pose new ones, thus challenging the theory. In particular, the energy spectrum of accelerated particles is now measured with unprecedented accuracy revealing significant variations of the spectral index, in contrast to the simple theoretical prediction. Although the theory does provide room for such variations by including the back-reaction from accelerated particles, shock geometry and environmental phenomena, the quantitative predictions are limited to oversimplified models operating in highly idealized shock environments.

Numerical simulations provide a great tool to improve the understanding of the initial acceleration phase as *in situ* observations, at least at SNR shocks, are not possible. Particularly hybrid simulations, in which the ion component of the plasma is treated kinetically, while the light electrons are described as a fluid, have proven to be very useful, see, e.g., [25, 26, 27]. A principle advantage of the hybrid modeling is the possibility to address the important waves and instabilities on the ion timescale, neglecting the high-frequency modes associated with electrons.

In this work we investigate particle acceleration at collisionless shocks in the context of CR energization by means of analytical and numerical modeling. We perform hybrid simulations with a focus on the initial phase of CR acceleration. Our aim is to improve the understanding of CR energization, which is only possible by a combination of experimental observations with numerical simulations and theory. As mentioned above, the recent high-precision observations indicate serious deviations from the standard DSA prediction for galactic CRs in the $1 - 500$ GeV energy range, challenging the hypothesis of CR origin in SNRs and raising doubts regarding the DSA as a viable explanation of the observed spectra. These deviations call to be explained by a consistent theory of CR acceleration.

One prominent example is the ≈ 0.1 difference observed in the spectral index of proton and helium rigidity spectra[3] first indicated in the baloon-born experiment ATIC-2 [28] and later confirmed with high accuracy by the PAMELA and AMS-02 measurements [5, 7]. Many earlier explanations for this "anomaly" have invoked additional assumptions about the SNR environment such as variable ionization states of He or inhomogeneous p/He mixtures in the upstream medium, which are difficult to verify, or, in the case of a

---

[3]   CR spectra are usually expressed in terms of kinetic energy, kinetic energy per nucleon, or particle rigidity, $\mathcal{R} = pc/Ze$, where p denotes the momentum, c is the speed of light and Ze the charge of the ion.

proposed multi-SNR origin, are not testable at all. The newest high-precision measurements challenge most past models, as the recently measured C/He and O/He AMS-02 flux ratios are independent of rigidity. This similarity of the spectra of three different elements with the same mass-to-charge (A/Z) ratio clearly points towards an A/Z-based selection mechanism, which is an intrinsic property of the injection into the DSA. Self-consistent simulations focused on the injection phase of the DSA, where elemental similarity does not apply, combined with analytic modeling allowed us to demonstrate that special conditions are, in fact, not vital for explaining the observed CR rigidity spectra [29].

Another prominent example for the deviation of the precise observations from the standard picture of CR origin is the significantly steeper source spectrum of CR compared to the prediction of the standard DSA theory. In recent high-precision observations by the CALET team [30], the spectral index was measured to be in the range $q = 2.87 \pm 0.06$ below 500 GeV. Although different CR propagation models predict an offset of the local spectra measured on Earth compared to the source spectra, thereby removing the difference to the DSA prediction partly, there is a growing consensus in the CR community that the corrections to the spectra only due to propagation effects fail to explain the newest high-precision data. Most of the DSA treatments are limited to homogeneous shock environments. In this thesis we investigate, whether inhomogeneity can produce the necessary extra steepening. We assume that the magnetic field changes its angle along the shock front and study the influence of a variable orientation of magnetic field on ion acceleration by means of two-dimensional hybrid modeling [24].

Besides ions also electrons are accelerated in SNR shocks, which can be observed remotely via the synchrotron radiation of these particles in the (amplified) magnetic fields [31, 32]. While the ion injection into the DSA is not fully understood, the injection of electrons is even more complicated and puzzling. It is still unresolved whether electrons drive the waves necessary to facilitate injection themselves or whether protons can generate the required turbulence to assist the electron injection. Moreover, also the thermalization of electrons in these shocks has to be understood. Here observations of Balmer-dominated shocks[4] can provide valuable insights into the downstream temperature ratios of electrons and ions [33]. While the electron kinetics are typically neglected in hybrid simulations, the addition of electron test-particles allows to analyze their behavior in the ion generated turbulence. This model has been used in the past [34] but also recently [35, 36] to investigate electron acceleration at quasi-perpendicular shocks, and we apply it to a parallel shock setup.

The material presented below is organized as follows. In Chapter 2 we review the basic concept of shocks in collisionless astrophysical plasmas and possible particle acceleration mechanisms in these environments. We introduce the hybrid model and give details about the underlying assumptions as well as particulars of the numerical implementation and parallelization strategy in Chapter 3. In Chapter 4 we discuss the results of hybrid simulations focused on the injection of different ion species into the DSA and confirm earlier theoretical predictions that the injection is a mass-to-charge dependent process. By

---

[4]   Balmer-dominated shocks are collisionless, non-radiative shocks in warm partially ionized gas, whose spectra are dominated by Balmer hydrogen lines.

combining the injection dependence obtained in the simulations with the shock evolution during the Sedov-Taylor phase of the SNR we obtain time-integrated spectra for protons and helium ions. In the rigidity range $\mathcal{R} > 10\,\mathrm{GV}$ our results are consistent with the rigidity dependent proton-to-helium flux ratio measured recently [5, 7]. In Chapter 5 we present the results of two-dimensional hybrid simulations aimed to investigate the acceleration of ions in shocks with variable obliquity. However limited in resources, these simulations have captured a new physical phenomenon in the DSA: the spectrum steepening at low energies associated with the variation of shock obliquity along its face. In Chapter 6 we investigate the possibility that protons accelerated to high energies create sufficient wave turbulence necessary for electron injection into the DSA. To that end we introduce in our one-dimensional hybrid simulation an additional test-particle electron population, aiming to see how these electrons are energized by the "hybrid" electromagnetic fields. Finally, a summary is given in Chapter 7.

CHAPTER 2

Theoretical Basics

2.1 Cosmic Rays and Their Origin

Cosmic rays (CRs) were discovered in 1912 by Victor Hess, who found during balloon experiments that the amount of ionizing radiation increases with altitude and deduced that it has to be of extraterrestrial origin [1]. This discovery was awarded with the Nobel prize in 1936. While initially this radiation was thought to be of electromagnetic nature (Millikan was an advocate of this hypothesis [37]), it was later found to consist of charged particles as measurements indicated an interaction of the CRs with the geomagnetic field [38]. In the following years it was discovered that atomic nuclei make up the main part of CRs impinging on Earth, while electrons contribute only little, with about 1 %. Among the nuclei protons are the most abundant species, alpha particles add with $\sim 10\%$ and heavier nuclei with less than 1% to the CR composition. Positrons and other anti-particles such as antiprotons [39] make up only a marginal fraction of CRs.

Nowadays, not only the composition of CRs can be analyzed, but also energy spectra are measured with great accuracy using various instruments. The energies and CR composition are either obtained directly using spectrometers on high altitude balloon flights [2, 3, 4] or by space based instruments like PAMELA [5] or AMS-02 [6, 7, 8, 9]. In these experiments the combination of different measurement methods, such as time-of-flight measurements, the deflection of charged particles in a magnetic field as well as calorimetric measurements, allow an accurate evaluation of the particle energy as well as excellent charge separation. Furthermore, the high-altitude observations mitigate the influence of secondary particles.

In contrast to the direct measurements outlined above the very high energy CRs are detected indirectly by large detector arrays on Earth. These indirect measurements rely on the observation of air showers, which are created when energetic ions interact with the molecules in the atmosphere [40]. The subsequent cascade of different particles that are created as well as the Cherenkov radiation can be detected by ground based detectors, and the initial energy of the CR particles can be estimated [10, 11].

The energy density of CRs with energies above 1 GeV is approximately 1eV cm^{-3}, which is comparable to the energy density of stellar photons or the energy density of the intergalactic field [41]. These particles have pronounced effects in the galaxy. They provide additional heating and ionization and play a crucial role in the dynamics of the interstellar medium (ISM). In this way CRs have an impact on the chemistry of molecular clouds [42] and can influence star formation [43]. Hence, the understanding of CR escape from supernova remnants (SNRs) and their post-acceleration into the ISM is important to understand elementary processes in the Universe.

A fundamental requirement for any theory trying to describe CR acceleration is the

correct reproduction of the CR energy spectrum. A CR energy spectrum composed of data obtained from various detectors is presented in Fig. 1. The spectrum extends over more than ten orders of magnitude in energy and thirty in flux. For energies above $E \approx$ 1 GeV, where the spectrum is not affected by the particle propagation through the solar wind, it follows a power law,

$$N(E)\, dE = a\, E^{-\gamma}\, dE. \tag{1}$$

Here γ is the power-law exponent or spectral index and a is a normalization constant. The measured spectrum indicates that there are several breaks, at which the spectral index changes. The first break occurs at an energy of $\sim 10^{15}$ eV and is referred to as "knee". Another break is visible at even higher energy ($\sim 10^{18}$ eV) and is called "ankle". The most energetic particle event being recorded so far has been a particle with an energy of 320 EeV [44].
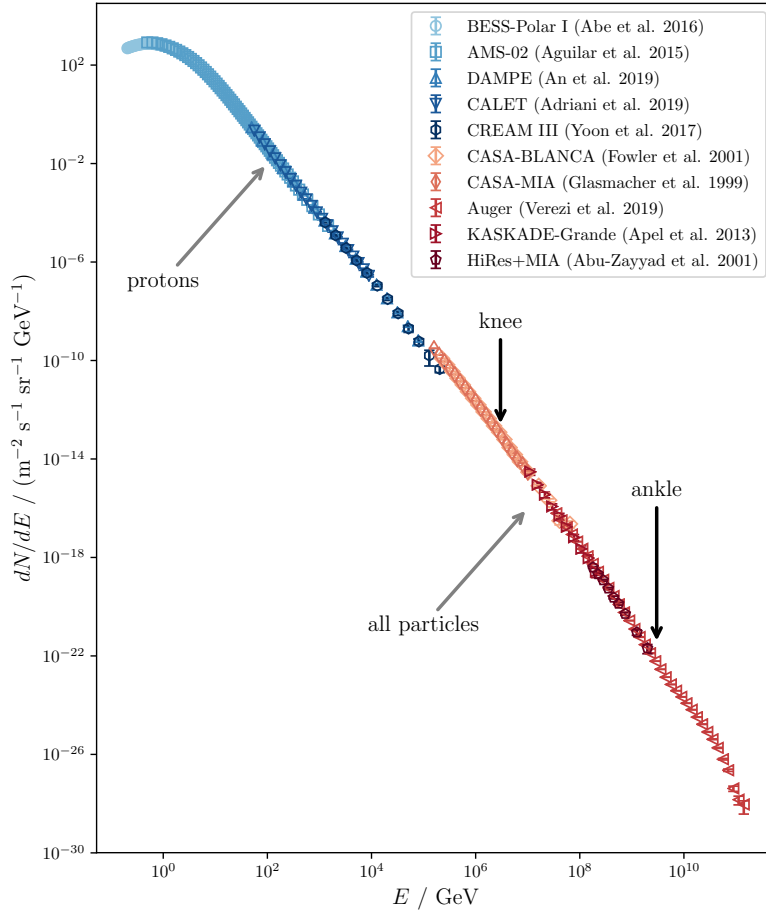
FIGURE 1: Energy spectrum of cosmic rays measured directly [7, 3, 45, 30, 46] and indirectly [47, 48, 49, 50, 51] with different detectors. The data of the direct measurements was obtained from the cosmic ray database [52].

While the question of the mechanism capable to accelerate ions to these extreme energies is very intriguing, we will focus in this work on CRs with energies below the "knee". They are much more abundant and thought to mainly originate from within our galaxy,

while the most energetic particles are supposed to be of extragalactic origin. The simple reasoning behind this statement follows from the motion of charged particles in the galactic magnetic field. As the Lorentz force is acting on charged particles moving through a magnetic field, they perform a gyration around the field lines. The Larmor radius can be defined as,

$$r_L = \frac{p_\perp c}{|q| B}, \tag{2}$$

where $p_\perp$ is the particle's momentum perpendicular to the background magnetic field, B, and q is the particle's charge, while c denotes the speed of light. For a proton with energy $E = 10^{18}$ eV the Larmor radius has a value of $r_L = 360$ pc, which is already on the order of the height of the galactic disk ($h \approx 600$ pc). Hence, such an energetic particle cannot be confined to the galactic disk. While this argument allows to distinguish between CRs of galactic and extragalactic origin, pinpointing the sources of CRs is nearly impossible. Due to the diffusive motion of CRs in the turbulent magnetic field in the ISM they reach Earth almost isotropically (see, e.g., [53]). Only for ultra-high-energy cosmic rays (UHECRs) significant indications of anisotropy have been reported [54, 55].

The question of the origin of CRs has engaged physicists since their discovery and hundreds of papers have been published on the topic in over eight decades. Although every now and then also other sources are proposed (see, e.g., [56]), observations as well as most theoretical considerations support a hypothesis that galactic CRs originate from SNRs. Already in 1934 Baade and Zwicky [57] connected the production of CRs to supernovae (SNe) explosions. This initial idea was based on energetic arguments, and until today SNe are thought to be the most probable sources of CRs, however, not the explosions themselves but SNRs. The arguments put forward more than 80 years ago are still valid and supported by the increasing precision of observations. The power necessary to maintain the measured CR energy density can be estimated as [41]

$$P_{\mathrm{CR}} \sim 2 \cdot 10^{41} \ \mathrm{erg \ s^{-1}}. \tag{3}$$

The energy released in a SN is on the order of

$$E_{\mathrm{SN}} \sim 10^{51} \ \mathrm{erg} = 10^{44} \ \mathrm{J}. \tag{4}$$

When combining this with the rate of SNe observed in the Milky Way, which is approximately one in every 50 years [58], a conversion of $\sim 10\%$ of the energy into CRs is necessary to obtain the required CR power. Additional clues pointing towards SNRs as sources of CRs are provided by observations of these objects in different bands of the electromagnetic spectrum. By X-ray observations, for example using the Chandra X-ray Observatory, the synchrotron radiation of accelerated electrons can be measured. The synchrotron emission from SNRs indicates the presence of GeV to TeV particles [59]. Hence, SNRs provide an environment for active and rapid particle acceleration. However, these observations do not allow to finally discriminate whether the emission originates from leptonic and hardronic acceleration. γ-ray measurements can help to resolve this issue. Protons become visible only when they illuminate dense ambient gas producing neutral pions (π^0) that, in turn,

decay into γ-photons which are finally detected. The resulting "pion bump" in the γ-ray spectra is thus a direct indication of CR acceleration. This feature, detected in the γ-ray observations of the middle-aged SNRs IC 443 and W44, provided a first direct observation of proton acceleration at SNRs [60]. However, the posibility of re-acceleration of pre-existing galactic CRs cannot be ruled out [61].

While these arguments already point towards SNRs as possible sources of CRs, they cannot answer which mechanism is responsible for the acceleration of the charged particles to enormous energies. A potential acceleration mechanism has to be able to explain the measured spectral shape and also has to be fast enough to achieve energies up to the "knee" during the lifetime of a SNR.

Before introducing the mechanisms thought to be responsible for CR acceleration, it is worthwhile to consider the environment, in which the acceleration occurs. In the following we briefly describe the conditions of the plasma in the ISM and the properties of the waves related to SN explosions.

2.2   Shocks in Collisionless Plasmas

Shock waves or shocks are abrupt transitions in bulk flow velocity, density, and temperature. They can be observed on Earth as well as at various sites and scales in the Universe, such as Earth's bow shock, the solar wind termination shock, supernova remnant shocks or shocks in clusters of galaxies. However, since the conditions in astrophysical environments differ considerably from the conditions on Earth, shocks in astrophysical environments are also inherently different from shocks observable in our atmosphere.

The density of atoms and molecules in the atmosphere is high and shocks are mediated by binary collisions. In turn, in most astrophysical environments the matter is in the plasma state, as most baryonic matter in the Universe. Hence the motion of charged particles is largely determined by (self-generated) electromagnetic fields. Furthermore, the particle density is many orders of magnitude lower than in the atmosphere and the temperature can be much higher, resulting in large mean free paths between collisions. While there is a fundamental difference between these systems, it is worthwhile to consider some aspects of gasdynamic (collisional) shocks before turning to collisionless shocks, which are generally associated with astrophysical environments.

Gasdynamic shocks

Gasdynamic shocks were discovered already at the end of the 19$^{\text{th}}$ century by Ernst Mach, who observed the formation of shocks if an obstacle was moving in the ambient medium with a velocity that is larger than the velocity of sound in this medium. This velocity ratio is now known as the (sonic) Mach number,

$$M_s = \frac{v}{c_s}, \tag{5}$$

where $c_s = \sqrt{\gamma\, p/\rho}$ denotes the velocity of sound with γ being the adiabatic index, p and ρ being the pressure and the mass density of the ambient medium, respectively. Such

situation occurs, for example, if a jet is flying with supersonic velocity. In this case a shock in form of a Mach cone with an opening angle that depends on M_s is formed.

Generally, two components are needed for the formation of a shock: a non-linearity that can cause a steepening of a wave or perturbation and some form of dissipation that limits the steepening and prevents wave breaking. The combination of these two factors can lead to a propagating, almost jump-like transition that is maintained over time. Upon the shock transition the flow speed of the medium is reduced from supersonic to subsonic. Hence, part of the bulk kinetic energy has to be transformed to thermal energy in the thin region of the shock transition. As this yields an increase in entropy, this process is irreversible and demands a dissipation mechanism at the shock front. In gasdynamic (collisional) shocks binary collisions are responsible for this dissipation. Hence, the length of the shock transition is determined by the mean free path,

$$\lambda_{\mathrm{mfp}} = \frac{1}{n\,\sigma}, \tag{6}$$

where n is the number density of the medium and σ is the collisional cross section.

The decrease of the bulk velocity of the shocked medium is accompanied by an increase in density and temperature; therefore, also the pressure increases. The region in which the velocity in the shock rest frame is supersonic, i.e., the unshocked medium is referred to as *upstream*, while the region of the hot shocked gas is referred to as *downstream*. The shock transition is shown schematically in Fig. 2 in different reference frames[5]. In the following, index "1" is used for the upstream region and "2" for the quantities measured in the downstream, as also indicated in the first panel of Fig. 2.

The quantities far upstream and downstream can be related via the Rankine-Hugoniot jump conditions. Assuming a plane parallel shock, i.e., the velocity is perpendicular to the shock front, the problem can be reduced to one dimension. The jump conditions can be derived from the conservation of mass, momentum and energy upon the shock transition:

mass conservation: $$\rho_1\,u_1 = \rho_2\,u_2 \tag{7}$$

momentum conservation: $$\rho_1\,u_1^2 + p_1 = \rho_2\,u_2^2 + p_2 \tag{8}$$

energy conservation: $$\rho_1\,u_1\left(\varepsilon_1 + \frac{1}{2}u_1^2 + \frac{p_1}{\rho_1}\right) = \rho_2\,u_2\left(\varepsilon_2 + \frac{1}{2}u_2^2 + \frac{p_2}{\rho_2}\right). \tag{9}$$

Here $\rho_{1,2}$ denotes the mass density, $u_{1,2}$ is the bulk velocity, $p_{1,2}$ is the pressure and $\varepsilon_{1,2}$ the specific internal energy. By inserting the specific enthalpy, h, of the ideal gas,

$$h = \varepsilon + \frac{p}{\rho} = \frac{\gamma}{\gamma - 1}\frac{p}{\rho}, \tag{10}$$

in Eq. (9), the shock compression ratio can be calculated as function of the upstream Mach number, $M_1 = u_1/c_{s,1}$,

$$r = \frac{\rho_2}{\rho_1} = \frac{u_1}{u_2} = \frac{(\gamma + 1)\,M_1^2}{2 + (\gamma - 1)\,M_1^2}. \tag{11}$$

---

[5] Often shocks are considered in the frame where the shock is at rest. In this thesis, if not stated otherwise, we will be using the downstream rest frame.
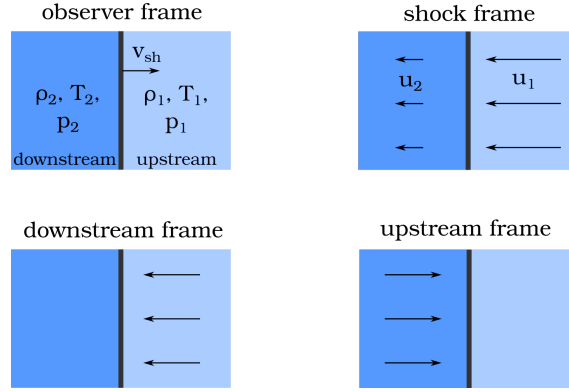
Figure 2: Schematic of a shock transition in different rest frames.

In the case of the ideal atomic gas the adiabatic index equals $\gamma = 5/3$. In the limit $M = 1$ the compression ratio becomes $r = 1$, so no shock exists. For very high Mach numbers, $M \to \infty$[6], the compression ratio approaches the value $r = 4$. The temperature ratio as function of the upstream Mach number, M_1, reads

$$\frac{T_2}{T_1} = \frac{[2\gamma\, M_1^2 - (\gamma + 1)]\,[2 + (\gamma - 1)M_1^2)]}{(\gamma + 1)^2 M_1^2}. \tag{12}$$

In the case of a strong shock ($M \gg 1$) the downstream temperature, T_2, scales proportionally to the square of the upstream velocity,

$$k_B\, T_2 \approx \frac{3}{16}\, m\, u_1^2, \tag{13}$$

where k_B denotes the Boltzmann constant. When considering a plasma, the jump conditions are altered due to the possible presence of a magnetic field, that has to be considered in the conservation laws. In this case the jump conditions can be derived with the help of magneto-hydrodynamic (MHD) equations, see, e.g., [62, Chapter 2].

Collisionless shocks

In astrophysical systems the possibility of the formation of shocks might seem surprising at first glance. Typically these environments consist of a hot and dilute gas, which is often even ionized and hence in the plasma state. The ISM, for example, is composed of matter with a density on the order of one particle per cubic centimeter and temperature of $T \approx 10^4\,\mathrm{K}$ in the warm ionized medium and $T \approx 10^6\,\mathrm{K}$ in the hot ionized medium [63]. In these environments the collisional mean free path becomes extremely large as it is inversely proportional to the particle density. Note that for a plasma the collisional cross section in Eq. (6) has to be replaced by the Coulomb cross section. Since collisions are negligible in these environments the plasma is termed collisionless. Naturally the question arises whether and how a shock can be maintained in these systems in the absence of dissipation via binary collisions. The existance of shocks in collisionless plasmas was experimentally established with the discovery of Earth's bow shock [64, 65], a standing

---

6   However, still only the nonrelativistic case is considered.

shock wave which is created due to the interaction of the solar wind with Earth's magnetic field. The mean free path with respect to Coulomb collisions for the solar wind plasma is on the order of one astronomical unit (AU) which considerably exceeds the size of the shock [66]. The collisionless plasma is well described by the collisionless Vlasov-Maxwell system of equations,

$$\frac{\partial}{\partial t} f_\sigma + \vec{v}_\sigma \nabla_{\vec{r}} f_\sigma + \frac{q_\sigma}{m_\sigma} \left(\vec{E} + \frac{\vec{v}_\sigma}{c} \times \vec{B} \right) \nabla_{\vec{v}} f_\sigma = 0 \tag{14a}$$

$$\nabla \times \vec{E} = -\frac{1}{c} \frac{\partial}{\partial t} \vec{B} \tag{14b} \qquad \nabla \times \vec{B} = \frac{4\pi}{c} \vec{J} + \frac{1}{c} \frac{\partial}{\partial t} \vec{E} \tag{14d}$$

$$\nabla \vec{E} = 4\pi \rho \tag{14c} \qquad \nabla \vec{B} = 0, \tag{14e}$$

where Eq. (14a) is the Vlasov equation[7], describing the evolution of the distribution function, $f_\sigma(\vec{x}, \vec{v}, t)$, of particles of species σ with mass and charge of m_σ and q_σ, respectively. Equations (14b–14e) are the Maxwell equations for the electromagnetic fields, $\vec{E}(\vec{x}, t)$ and $\vec{B}(\vec{x}, t)$. The sources of these fields are not the discrete particles that compose the plasma but a continuous distribution of charges and currents, $\rho(\vec{x}, t)$ and $\vec{J}(\vec{x}, t)$,

$$\rho = \rho(\vec{x}, t) = \sum_\sigma q_\sigma \int f_\sigma(\vec{x}, \vec{v}, t) \, d^3v, \tag{15a}$$

$$\vec{J} = \vec{J}(\vec{x}, t) = \sum_\sigma q_\sigma \int \vec{v} f_\sigma(\vec{x}, \vec{v}, t) \, d^3v. \tag{15b}$$

The coupling of charged particles and electromagnetic fields in the plasma allows for the excitation and propagation of a plethora of different plasma waves. Hence, in collisionless plasma the collective particle dynamics as well as wave-particle interactions are extremely important. In these systems, where dissipation due to binary collisions is negligible, the non-linear wave steepening can be balanced by dispersion. Analytic calculations have shown that this balance can lead to the formation of large amplitude soliton structures [67, 68]. These solitons or soliton trains transform into shocks when their widths reach the scale of internal dissipation. Note that while the Vlasov-Maxwell system is time reversible and hence conserves entropy, a statistical description of the wave turbulence introduces irreversibility [68]. For higher Mach numbers the dissipation of energy via reflection of a part of the incoming particles becomes important. The early analytical works, summarized for example in [69], have laid the foundations for the understanding of the microphysics of collisionless shocks, especially the formation of shocks due to dispersion.

With respect to the electrodynamic properties the shocks can be divided into *electrostatic* and *magnetized*. In absence of currents and background magnetic field, the motion of the charged particles is purely determined by electrostatic forces, and shock waves that are formed under these conditions are termed *electrostatic*. Electrostatic shocks are a consequence of non-linear wave steepening and wave breaking of ion-acoustic modes and they are more relevant for laboratory experiments, e.g., in laser-plasma interactions [70, 71]

---

[7] The Vlasov equation is equivalent to the Boltzmann equation with the collision term set to zero.

and fast ignition [72]. In the astrophysical environment they occur only on small scales [66] and therefore do not belong to the regular large scale, genuine shocks. Theoretical studies of electrostatic shocks are instrumental for the understanding of the microphysics of particle reflection off the shock front including CR loaded shocks [73, 74, 75]. Most astrophysical shocks are *magnetized shocks* because the magnetized astrophysical plasma allows the current flows along and across the background magnetic field. These shocks are of macroscopic nature, they behave differently from electrostatic shocks and, because of their abundance, are much more important in astrophysical scenarios than electrostatic shocks [66].

In magnetized environments a number of different plasma waves can be excited. One particular mode is the Alfvén wave, a low frequency, incompressible MHD wave propagating along the magnetic field. The phase velocity of this wave equals to the so-called Alfvén velocity,

$$v_A = \frac{B_0}{\sqrt{4\pi\, n_0\, m_i}} \tag{16}$$

where B_0 is the amplitude of the background magnetic field, n_0 denotes the ion density and m_i is the ion mass. As the Alfvén velocity is a characteristic velocity in a magnetized plasma, one introduces the Alfvénic Mach number to characterize magnetized shocks, similarly to the sonic Mach number in gasdynamics, Eq. (5), as

$$M_A = \frac{v_{\mathrm{sh}}}{v_A}. \tag{17}$$

In the following, we will be mostly dealing with magnetized shocks and waves in magnetized plasmas, and, if not stated differently, we will omit the subscript and denote M as the Alfvénic Mach number. Since in the context of magnetized shocks the direction of the magnetic field with respect to the shock propagation direction plays an important role, one distinguishes (quasi-)parallel and (quasi-)perpendicular shocks according to the angle between shock normal and background magnetic field, θ_{Bn}. For quasi-parallel shocks $\theta_{\mathrm{Bn}} < \pi/4$, while quasi-perpendicular shocks have $\theta_{\mathrm{Bn}} > \pi/4$.

The investigation of collisionless shocks is possible by *in situ* measurements of the shocks in the solar system, e.g., [76, 77], while other astrophysical collisionless shocks, for instance SNR shocks, can only be studied indirectly, e.g., [78]. The experimental realization of collisionless shocks in the laboratory is difficult as the influence of collisions has to be suppressed. However, the advance of laser technologies made it possible to create collisionless shocks in intense laser-plasma interaction experiments [79, 80, 81]. Finally, collisionless shocks can be investigated by means of numerical modeling. The continuous advances in the performance of modern supercomputers over the past decades allowed to increase the dimensionality and "size" of the simulations from one-dimensional calculations on a linear grid with a few hundred numerical cells [82] to present two- and even three-dimensional simulations with $> 10^8$ grid points [83, 84]. This allowed to extend both the spatial and temporal resolution and enabled to follow the evolution of the shocks over long time.

In contrast to shocks in collisional gases or plasmas, where the particle distribution

quickly relaxes to a Maxwellian, collisionless shocks are generally associated with the presence of nonthermal particle populations. These particles can be accelerated in the shock environment and influence the structure and properties of the shock itself via the formation of an extended shock precursor.

2.3 Particle Acceleration in Astrophysical Environments

2.3.1 Stochastic Acceleration

A first idea of a possible mechanism for CR acceleration was presented by Enrico Fermi in 1949 [85]. He proposed an energization mechanism based on scattering of CRs by "magnetic clouds". The mechanism is depicted schematically in Fig. 3. The magnetic clouds (irregularities in the galactic magnetic field) are supposed to move through the galaxy with a velocity, v, and corresponding $\beta = v/c$ and $\gamma = (1-\beta^2)^{-1/2}$. Let us assume that a relativistic particle with energy $E_1 \approx p\,c$ in the galaxy's reference frame reaches the cloud. Its energy in the reference frame of the cloud is given by,

$$E_1' = \gamma E_1(1 - \beta \cos \theta_1), \tag{18}$$

where θ_1 is the angle between the cloud's velocity and the particle propagation direction. Inside the cloud the particle interacts with the magnetic field, scatters and changes the velocity direction. Since the energy in the rest frame of the scattering center is conserved, the energy of the particle does not change, $E_2' = E_1'$. After scattering the particle leaves the cloud and its the energy in the galaxy's rest frame can be written as

$$E_2 = \gamma E_2'(1 + \beta \cos \theta_2), \tag{19}$$

where θ_2 denotes the angle between the velocity of the cloud and the particle escape direction. In this way the particle may either gain or lose energy, depending on whether the collision is head-on or tail-on. Since the particle can interact with many "clouds" during its propagation through the galaxy, only the average energy difference is of interest. It can be obtained by averaging $E_2 - E_1$ over the angles θ_1 and θ_2. Assuming that the particles are isotropized by the scattering inside the cloud we immediately get $\langle \cos \theta_2 \rangle = 0$. Averaging over the angle of incidence, θ_1, yields

$$\langle \cos \theta_1 \rangle = \frac{\int_{-1}^{1} \cos \theta_1 \, (1 - \beta \cos \theta_1) \, d \cos \theta_1}{\int_{-1}^{1} (1 - \beta \cos \theta_1) \, d \cos \theta_1} = \frac{-2\beta/3}{2} = -\frac{\beta}{3}. \tag{20}$$

And the average energy gain reads

$$\left\langle \frac{\Delta E}{E} \right\rangle_\theta = \left\langle \frac{E_2 - E_1}{E_1} \right\rangle_\theta \approx \frac{4}{3}\beta^2, \tag{21}$$

where the assumption $\beta \ll 1$ has been used. The result is on the order of $\mathcal{O}\left((v/c)^2\right)$, and hence the mechanism is termed *second order Fermi acceleration*. At first glance it might be surprising that the random cloud-particle encounters result in an average energy
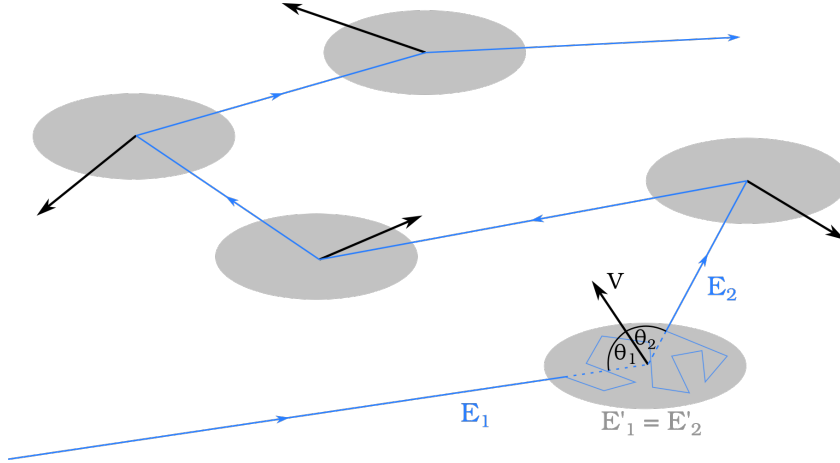
FIGURE 3: Sketch of the second order Fermi acceleration mechanism. Energetic particles (blue) are scattered inside "magnetic clouds" (grey) which move randomly through the galaxy with a characteristic velocity, v. These particle-cloud encounters can result either in an increase or decrease of the particle energy.

gain at all. But consider a simplified analog of a driver on a highway: the driver will see more cars coming towards him than he is passing. Similarly, a particle will experience more head-on than tail-on collisions with magnetic clouds and on average gain energy. However, the energy increase, provided by this mechanism, is only second-order in v/c, and the random velocities of the magnetic clouds in the galaxy are comparatively small, rendering it too slow for particles to ever achieve energies up to the "knee". Nevertheless, this mechanism might be important in the context of CR re-acceleration [86].

2.3.2 DIFFUSIVE SHOCK ACCELERATION

In the 1970s a mechanism of ion acceleration at collisionless shocks was proposed independently by several authors [18, 19, 20, 21, 22]. It is now actively researched under the name diffusive shock acceleration (DSA) (see, e.g., [87, 88, 89] for reviews). The basic idea is presented below. In a nutshell, the charged particles gain energy by crossing the shock front many times while being scattered by magnetic perturbations in the shock vicinity. This process is shown schematically in Fig. 4, where the particle motion is depicted by the blue line and the perturbations in the up- and downstream plasma are plotted in black. Due to the many scattering events the pitch angle, i.e., the angle between the particle velocity and the magnetic field, changes and the particle performs a diffusive motion. In principle, this process can be approached from the macroscopic point of view by considering the transport equation for the distribution function, $f(x, p, t)$,

$$\frac{\partial f}{\partial t} + u\frac{\partial f}{\partial x} = \frac{\partial}{\partial x}\left(\kappa(x, p)\frac{\partial f}{\partial x}\right) + \frac{1}{3}\frac{\partial u}{\partial x}\, p\,\frac{\partial f}{\partial p}, \tag{22}$$

where u denotes the fluid velocity and κ is the spatial diffusion coefficient. A solution for the distribution function can be found by introducing the velocity profile for a shock and considering only stationary solutions. Here we will follow the microscopic approach derived in [20], as this provides a more intuitive description.
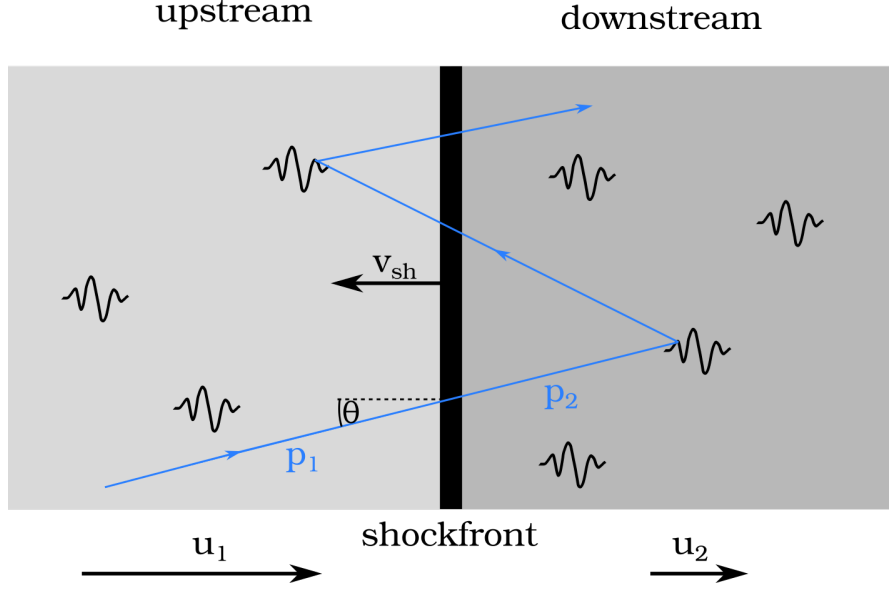
Figure 4: Sketch of the first order Fermi acceleration mechanism. Energetic particles (blue) are scattered by magnetic perturbations in the shock vicinity.

As in the case of the second order Fermi acceleration, we consider an already relativistic particle with $v \approx c$. Suppose it is located initially upstream of the shock and has a momentum p_1 in this frame.[8] Its momentum in the shock frame reads

$$p' = p_1 \left(1 + \frac{u_1 \cos \theta}{v} \right), \tag{23}$$

where θ denotes the angle between the particle velocity and the shock normal, see Fig. 4. With a further transformation to the downstream frame one obtains

$$p_2 = p_1 \left(1 + \frac{(u_1 - u_2) \cos \theta}{v} \right). \tag{24}$$

Again we are interested in the average change in momentum upon shock crossing, so we have to average over the angular distribution of the velocities. We can assume that the velocity distribution is almost isotropic due to the pitch angle scattering at magnetic perturbations in the local fluid frame. The number of particles reaching the shock in the angular interval $[\theta, \theta + \mathrm{d}\theta]$ is proportional to $(2\pi \sin\theta \, \mathrm{d}\theta) \cos\theta$ so the average momentum gain per shock crossing can be calculated as

$$\left\langle \frac{\Delta p}{p} \right\rangle_\theta = \int_0^1 \frac{(u_1 - u_2) \cos\theta}{v} 2 \cos\theta \, \mathrm{d}\cos\theta = \frac{2}{3} \frac{u_1 - u_2}{v}. \tag{25}$$

Since the velocity upstream of the shock is larger than downstream, this gain in momentum is always positive. The same result is obtained for a particle crossing the shock from downstream to upstream. Hence, by every shock crossing the particle gains some energy. The energy increase in this case is on the order $\mathcal{O}(u/c)$ leading to the label *first order*

---

[8] We will use the indices 1 and 2 for upstream and downstream quantities, respectively, as introduced in Sec. 2.2.

Fermi acceleration. However, not all particles get continuously accelerated because not all of them return to the shock, some are advected downstream. The flux of escaping particles can be simply written as

$$u_2 \, n, \tag{26}$$

where n denotes the particle density in the local fluid frame. The flux of particles entering downstream region reads

$$\int_0^1 \frac{n \, v \, \cos \theta}{2} \, \mathrm{d} \cos \theta = \frac{n \, v}{4}. \tag{27}$$

Using the fluxes of particles entering and leaving the downstream region allows to calculate the probability that a particle returns to the shock,

$$P_{\mathrm{ret}} = 1 - \frac{4 \, n \, u_2}{n \, v} = 1 - \frac{4 \, u_2}{v}. \tag{28}$$

In order to obtain a momentum distribution for the accelerated particles let us calculate the probability that a particle crosses the shock $2n$ times (n times crossing and recrossing). This can be obtained from the return probability above,

$$P_n \sim \prod_{i=1}^{n} \left[1 - \frac{4 \, u_2}{v_i} \right]. \tag{29}$$

After $2n$ shock crossings the momentum has increased to

$$p_n \sim \prod_{i=1}^{n} \left[1 + \frac{4}{3} \frac{u_1 - u_2}{v_i} \right] p_0, \tag{30}$$

where p_0 is the initial particle momentum. The probability of a particle being accelerated to p_n is obtained by taking the logarithm of Eqs. (29) and (30) and combining them,

$$P_n = \left(\frac{p_n}{p_0} \right)^{-3 \, u_2 / (u_1 - u_2)}. \tag{31}$$

Hence, the number of particles accelerated to p_n is simply $N(p_0) \, P_n$, and one obtains a power law for the momentum distribution,

$$f(p) \propto p^{-q} \qquad \text{with} \qquad q = \frac{3 \, u_2}{u_1 - u_2} = \frac{3r}{r - 1}, \tag{32}$$

where the exponent depends only on the shock compression ratio $r = \rho_2 / \rho_1 = u_1 / u_2$. For strong shocks with $M \gg 1$ one can make use of the Rankine-Hugoniot conditions to express the power-law index in terms of the shock Mach number as

$$q = \frac{4}{1 - M^{-2}}. \tag{33}$$

For strong shocks ($M \gg 1$) the diffusive shock acceleration hence predicts a $f(p) \propto p^{-4}$ power-law behavior. Transforming this to an energy spectrum one gets $f(E) \propto E^{-2}$ for relativistic and $f(E) \propto E^{-1.5}$ for subrelativistic particles.

While this mechanism is conceptually simple and robust, its precise outcome for the energy spectra and chemical composition of accelerated particles is difficult to determine under realistic shock conditions [23, 24]. In particular, the initial part of the acceleration, i.e., the "injection" of different species into the DSA remains largely unsolved [66, Section 7.4]. It ensures a smooth transition between the thermal plasma and the power-law spectrum at high energies. The question is how the shock selects a tiny fraction of particles to keep on crossing its front and gain energy by the DSA. This and other challenges in the DSA with the focus on the injection phase are the main issues of this thesis. It should be noted that there exist several extensions of the DSA theory. For instance, non-linear diffusive shock acceleration (NLDSA) (see [90] for a review) accounts for the back-reaction of the energetic particles on the shock structure.

The injection problem

One of the big caveats of the theory of diffusive shock acceleration is that it simply assumes the presence of a population of energetic particles that can freely cross the shock many times to gain energy. However, the origin of these energetic particles constitutes one of the burning questions in the physics of particle acceleration at collisionless shocks. The problem of how a population of particles is selected by the shock to keep crossing it and gain energy is very complex and has to be treated self-consistently as the accelerated particles interact with the electromagnetic turbulence in the shock vicinity and can influence the shock structure. Mostly two different kinds of particles have been thought to be a possible seed population: hot particles, evaporating from the downstream plasma[9] [91, 92, 26] or shock reflected particles, originating from the upstream [62]. The ion injection into the DSA has been investigated numerically by means of test-particle calculations [93], Monte Carlo [94], particle-in-cell (PIC) [95] and hybrid simulations [96]. While some of these simulations lead to the development of injection models (see, e.g., [97]) none of those describes the injection process sufficiently accurate. Another related problem is the injection of electrons into the acceleration process, which is even less understood.

An interesting question concerning the injection was already posed 50 years ago in the context of the composition of the plasma (see, e.g., [98, 99]): Does the selection mechanism favor certain ion species? And can the composition of the energetic particles be related to the initial composition of the background plasma? Monte Carlo simulations indicated that the injection is enhanced with increasing mass-to-charge (A/Z) ratio [99, 100]. The analytic theory developed in [101] and extended in [102, 103] also predicts a dependence of the injection efficiency on the mass-to-charge ratio. Very recent measurements by the AMS-02 collaboration have shown a coincidence in the accelerated particle spectral slopes of three different elements with mass-to-charge ratio $A/Z \simeq 2$ (He, C, and O) [8, 9]. This discovery points to an intrinsic, A/Z-based selection mechanism. More details, including our particular contribution to the subject are presented in Chapter 4 of this thesis.

Below we shortly discuss how particles and waves interact in a collisionless plasma, and how electromagnetic turbulence can be generated upstream of the shock.

---

[9]   This is also refered to as "thermal leakage".

2.3.3 SHOCK DRIFT ACCELERATION

A process that can energize charged particles at magnetized collisionless shocks without the requirement of any turbulence is the so-called shock drift acceleration (SDA). It mostly occurs at quasi-perpendicular shocks and is depicted schematically in the left panel of Fig. 5. We consider a planar shock with the magnetic field perpendicular to the shock normal in the shock reference frame. Downstream of the shock the magnetic field is compressed to $\vec{B}_2 = r\,\vec{B}_1$, where $r \geq 1$ is the compression ratio. Upstream of the shock the ion gyrates in the magnetic field and moves towards the shock front due to the $\vec{E} \times \vec{B}$-drift. Here $\vec{E}$ is the motional electric field,

$$\vec{E} = -\frac{1}{c}\,\vec{u}_1 \times \vec{B}_1 = -\frac{1}{c}\,\vec{u}_2 \times \vec{B}_2. \tag{34}$$

When the ion reaches the shock, it enters the downstream region with a stronger magnetic field which tightens the radius of its orbit. The new orbit may still be large enough to allow the particles to pass back into the upstream for parts of several gyrations as the particle gyrates in the magnetic field and the shock transition is smaller than the ion Larmor radius. Since the Larmor radius in the upstream is larger than in the downstream, the ion drifts along the shock in the direction of the electric field and gains some energy before it is finally advected in the downstream medium. The same mechanism also works for electrons, which will drift along the shock anti-parallel to the electric field, because their gyromotion is driven in opposite direction with respect to ions. In the case of a perpendicular shock the particle cannot return to the shock front after it has fully passed the shock. Hence, the energy gain is limited and no power law in the energy spectrum can be expected. However, SDA might be important to energize particle above the thermal distribution, allowing them to be injected into the DSA [97].

A variation of this mechanism is the shock surfing acceleration (SSA), where the cross shock potential (see red area in the right panel of Fig. 5) is accounted for. The electric field connected to this potential can cause a specular reflection of the ion. As for the SDA the ion gains energy as it moves in the direction of the motional electric field along the shock. The motion is, however, restricted to the upstream region as long the particle is reflected by the cross shock potential.

2.3.4 PARTICLE-WAVE INTERACTION

We have already established that the mean free path in astrophysical plasmas can be extremely large, yielding a collision time to be long compared to the characteristic timescales of the system, which are determined by the inverse plasma and cyclotron frequencies. This means the plasma can be treated as collisionless, and dissipation due to binary collisions is not efficient. Therefore, an important ingredient for the formation of shocks seems to be missing. However, the interaction of electromagnetic waves and particles can take the role of collisions and introduce dissipation in the system. The topic of wave-particle interaction in collisionless plasmas is vast and several books have been published discussing the microphysics of collisionless plasmas and, in particular, collisionless shocks (see, e.g.,
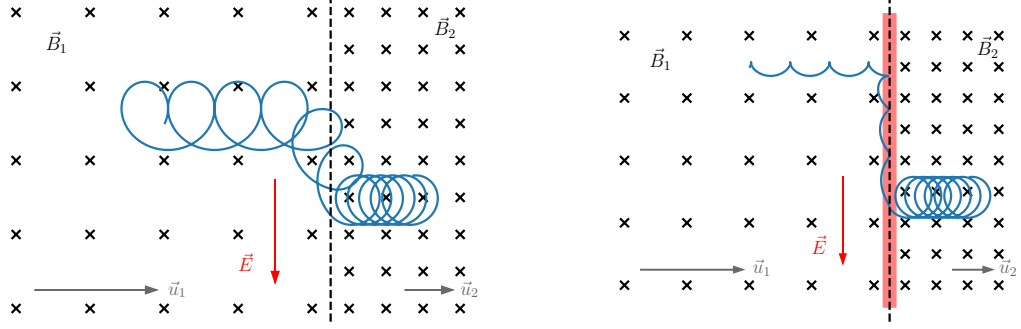
FIGURE 5: (left) Schematic diagram of shock drift acceleration SDA at a perpendicular shock with the magnetic field pointing into the plane of the figure. (right) Sketch of the shock surfing acceleration mechanism. The cross shock potential is indicated by the red area.

[104, 105]). Here we briefly discuss how a charged particle interacts with a electromagnetic wave and introduce some instabilities which are important in the context of collisionless shocks and may lead to the amplification of the magnetic field in these systems.

A PARTICLE IN A WAVE

The simplest textbook example is the motion of a charged particle in an electrostatic wave

$$\phi(x,t) = \phi_0 \, \cos(kx - \omega t), \tag{35}$$

where ϕ_0 is the wave amplitude, $k = 2\pi/\lambda$ denotes the wave vector and ω the frequency. In the wave rest frame,

$$x' = x - (\omega/k)\, t \tag{36}$$

$$v' = v - \omega/k, \tag{37}$$

the energy of the particle reads

$$E_{\text{tot}} = \frac{1}{2} \, mv'^2 + Ze\, \phi_0 \cos(kx'). \tag{38}$$

Depending on the sign of the total energy the particle can be either trapped ($E_{\text{tot}} < 0$) or passing ($E_{\text{tot}} > 0$). In the phase space (x', v') particles will move along lines of constant energies which form closed loops for the population of trapped particles.

A prominent example of the interaction between particles and electrostatic waves is the so-called Landau damping [106]. If particles move with a velocity close to the phase velocity of the wave they are accelerated or decelerated, depending on whether they move slightly slower or faster than the phase velocity of the wave. Hence, some particles will gain energy from the wave while others lose energy. In thermal equilibrium the velocity distribution function is Maxwellian and in general there will be a larger number of particles moving with a velocity slightly lower than any phase velocity. Hence, on the average the wave gives its energy to the particles and is damped. In non-equilibrium systems it can

be the case that for certain phase velocities the gradient of the distribution function is positive and the wave gains energy from the particles and is amplified. This simple example already indicates the importance of wave-particle interactions and shows that dissipation is possible also in the absence of binary collisions. Hence, even in unmagnetized collisionless systems all the ingredients for shock formation are present.

Ion Cyclotron Resonance

The motion of a charged particle in an electromagnetic field is governed by the Lorentz force,

$$\vec{F}_L = q \left(\vec{E} + \frac{1}{c}\, \vec{v} \times \vec{B} \right). \tag{39}$$

To describe the motion, it is useful to split the particle velocity into components parallel and perpendicular to the magnetic field,

$$\vec{v} = v_\parallel \frac{\vec{B}_0}{|\vec{B}_0|} + \vec{v}_\perp. \tag{40}$$

In absence of an electric field, the Lorentz force changes only the direction of the $v_\perp$ component while the velocity along the magnetic field remains unchanged. Hence, the particle will perform a spiraling motion around the field line with the handedness determined by the particle's charge (a positive charged particle will gyrate left-handed), see left panel of Fig. 6. The radius of the cyclotron motion is the Larmor radius, see Eq. (2), and the cyclotron frequency reads

$$\omega_c = \frac{q\, B_0}{m\, c}. \tag{41}$$

In a uniform magnetic field the angle that the instantaneous particle velocity makes with respect to the magnetic field vector is constant and is called the pitch angle, $\alpha = \sin^{-1}(v_\perp/v)$. When a particle is moving along the magnetic field in a wave with finite wave number, an interaction between particle and wave can result in a change in pitch angle. This happens when the Doppler-shifted frequency of the wave coincides with the particle's gyrofrequency or is equal to a multiple of ω_c. In this case the particle and the waves remain in phase, leading to energy and momentum exchange between them. The condition for the *cyclotron resonance* is

$$\omega - \vec{k} \cdot \vec{v} = \pm n\, \omega_c, \qquad n = 0, 1, 2, \ldots. \tag{42}$$

The parallel velocity component $v_\parallel$ of the particle changes due to the Lorentz force, $\frac{q}{c}\, \vec{v} \times \delta\vec{B}$, where $\delta\vec{B}$ denotes the wave magnetic field. Depending on the direction of the particle propagation and the phase between the gyro motion and the wave, $v_\parallel$ can increase or decrease. This results in a change of the pitch angle, see the right panel of Fig. 6. Note that the timescale of the interaction is typically much shorter than the cyclotron time, resulting in a violation of the conservation of the first adiabatic invariant. Additionally, the total energy of the particle is only conserved in the rest frame of the wave. Depending on
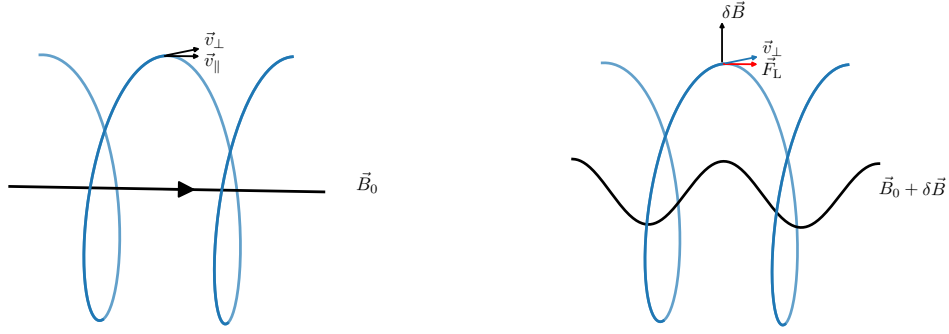
FIGURE 6: (left) Gyration of a positively charged ion around a magnetic field line. (right) Pitch angle scattering due to resonant wave-particle interaction.

whether $v_\parallel$ increases or decreases upon the interaction the particle gains or looses energy from/to the wave.

One can distinguish normal and anomalous resonance, see, e.g., [107]. The normal resonance describes a situation in which wave and particle propagate towards each other. In this case a left-hand gyrating particle interacts with a left-hand polarized wave. If an ion overtakes a wave ($v_\parallel > v_{\mathrm{ph}}$) it will interact with a right-handed wave (because it "sees" it as left-handed). This is termed anomalous resonance and here the negative sign in Eq. (42) has to be used [108, 109].

BELL'S NONRESONANT COSMIC RAY INSTABILITY

Observations indicate that the acceleration of particles and magnetic field amplification are intertwined phenomena. In fact, measurements of the synchrotron emission from accelerated electrons in young SNRs in the X-ray band indicate not only efficient electron acceleration but also a strong amplification of the magnetic field [110, 111]. While the cyclotron resonance provides a way of amplifying Alfvén waves, the whole process of magnetic field amplification at SNR shock is still not fully understood. Another mechanism of magnetic field amplification has been proposed recently [112], which has been termed cosmic ray current-driven instability or Bell's (nonresonant) instability.

Upstream of the shock the CR particles drift along the background magnetic field with respect to the upstream plasma. Especially more energetic particles, which are scattered less often by the magnetic turbulence, propagate further away from the shock. This drift creates a current of positively charged particles, J_{CR}, which is compensated by a return current, $J_{\mathrm{ret}} = -J_{\mathrm{CR}}$, in the thermal background plasma to maintain neutrality. In the presence of a small perturbation, $\delta\vec{B}$, there will be a force proportional to $\vec{J}_{\mathrm{ret}} \times \delta\vec{B}$ acting on the background plasma. If the perturbation is helical, the force on the background plasma results in a stretching of the magnetic field line and an amplification of the field.

It has been shown [113] that for a constant cosmic ray current the maximum growth rate of the instability is

$$\gamma_{\max} = J_{\mathrm{CR}}\sqrt{\frac{\pi}{\rho\,c^2}}, \tag{43}$$

where ρ denotes the mass density of the background plasma. The instability generates a broad spectrum of waves, and the fastest growing modes

$$\lambda_{\max} = \frac{B_0 \, c}{J_{\mathrm{CR}}} \tag{44}$$

were claimed to saturate via magnetic tension only for $\delta B \gg B_0$ [112]. Magnetic field amplification due tho this mechanism has been observed in MHD and PIC simulations [114, 115] and might play an important role for CR acceleration and propagation. Recently, an exact solution of the MHD equations in form of oscillatory magnetic pulses driven by a CR driver was found [116]. In high Alfvén Mach number shocks the peak amplitude may indeed approach $\delta B \sim M_A B_0 \gg B_0$. However, in partially ionized media additional damping has to be considered [117].

CHAPTER 3

The Hybrid Model

The modeling of shock waves in collisionless plasmas is an extremely challenging task for numerical simulations as these systems are inherently multi-scale. Spatial scales spanning from the kinetic scales of electrons and ions up to the precursor length influence the dynamical evolution of the system on the respective timescales. While a magneto-hydrodynamic (MHD) description might be appropriate to obtain the overall shock structure on large scales, see, e.g., [118], kinetic effects have to be considered to correctly describe the shock evolution and particle acceleration. On the other hand, a completely kinetic numerical treatment, e.g., based on the Vlasov-Maxwell system of equations, see Eq. (14), using, for example, the particle-in-cell (PIC) method is computationally not feasible, since one has to resolve the electron scales while following the evolution of the shock on timescales of the ions. For this reason, fully kinetic simulations can only be performed in reduced dimensionality or with strongly decreased ion-to-electron mass-ratios (e.g., $m_p/m_e = 30$ in [119]), which can influence the simulation results, see discussions in [120].

Here the hybrid approach comes to the rescue: by treating some plasma components as a fluid, but retaining a kinetic formulation for other components, the numerical effort can be reduced. Typically the ions are described kinetically while the electron population is treated as a massless charge neutralizing fluid. In this way high-frequency modes, associated with electron dynamics, are removed from the governing equations. This model is applicable when the scale of the system is comparable to the ion Larmor radii and the ions, therefore, must be treated fully kinetically, but the frequencies of interest are low compared to the ion cyclotron frequency. In the case of ion acceleration at collisionless shocks, time and spatial scales are clearly determined by the ions[10].

The possibility of a correct description of the ion kinetics has lead to a succesful application of hybrid modeling for the investigation of collisionless shocks for more than 30 years, see, e.g., [122, 123, 124, 125]. A detailed overview of the hybrid model together with the underlying equations and assumptions as well as possible extensions, such as the introduction of a finite electron mass, can be found in [25, 126, and references therein]. In the following we introduce the hybrid model used in this work and discuss the main aspects of our particular implementations of the related numerical algorithms. If not stated otherwise all equations below are given using *cgs* units.

---

[10]   This has been also deduced from data of the ISEE spacecrafts obtained at Earth's bow shock, see [121], where it was measured that the size of the shock structure is defined by the ion scales and the main dissipation mechanism is the reflection of ions.

3.1 Equations and Assumptions

In our hybrid model the evolution of the ion distribution function, $f_i(\vec{x}, \vec{v}, t)$, is governed by the kinetic Vlasov equation:

$$\frac{\partial}{\partial t} f_i + \vec{v}_i \nabla f_i + \frac{q_i}{m_i} \left(\vec{E} + \frac{1}{c} \vec{v}_i \times \vec{B} - \eta \vec{J} \right) \frac{\partial}{\partial v} f_i = 0, \tag{45}$$

where $\vec{E}, \vec{B}$, and $\vec{J}$ are the electric and magnetic fields, and the current density, $q_i = Z e$ and $m_i = A m_p$ denote the ion charge and mass (with e and m_p being the proton charge and mass, respectively). The electronic plasma component is treated as a charge neutralizing massless fluid. The assumption of neutrality,

$$n_e(\vec{x}, t) = n_i(\vec{x}, t) = n(\vec{x}, t), \tag{46}$$

where n_σ ($\sigma = e, i$) denotes the charge density, is justified on the ion scales, as they are much larger than the electron Debye length scale. Due to the high mobility of the electrons any charge separation will be compensated as the electrons quickly respond to the created electrostatic potential.

The momentum equation for the massless electron fluid reads

$$n_e m_e \frac{d\vec{u}_e}{dt} = 0 = -e n_e \left(\vec{E} + \frac{1}{c} \vec{u}_e \times \vec{B} \right) - \nabla \bar{\bar{p}}_e + e n_e \bar{\bar{\eta}} \vec{J}, \tag{47}$$

where $-e$, m_e, n_e, and $\vec{u}_e$ are the electron charge, mass, density and bulk velocity. The second term on the right hand side includes the electron pressure tensor, $\bar{\bar{p}}_e$, and the last term describes a friction force due to anomalous resistivity, $\bar{\bar{\eta}}$.

While in the general derivation of the fluid equations the electron pressure is introduced as a tensor (see, e.g., [127, Sec. 2.11]), where the diagonal terms describe the hydrostatic pressure, we assume an isotropic plasma. This can be expressed as $p_{xx} = p_{yy} = p_{zz} = p_e$, so the pressure is treated as a scalar. Finally, an equation for the electron temperature has to be prescribed to close the set of equations. We assume an adiabatic equation of state[11] yielding

$$p_e = n_e T_e \qquad \text{with} \qquad \frac{T_e}{T_{e,0}} = \left(\frac{n_e}{n_{e,0}} \right)^{\gamma - 1}, \tag{48}$$

with the adiabatic index $\gamma = 5/3$.

The phenomenological anomalous resistivity introduced in Eq. (47) is also assumed to be isotropic, so $\bar{\bar{\eta}} = \eta \bar{\bar{1}}$. This resistivity represents a way to account for anomalous wave-particle scattering at high-frequency, short-wavelength waves, which are not explicitly treated by the model [129]. It gives rise to electron Ohmic heating and smoothes the fields on the resistive scale. The corresponding collision frequency can be calculated as $\nu/\omega_{pi} = \eta \omega_{pe}^2 / 4\pi \omega_{pi}$. Detailed investigations of the influence of this quantity were performed in [122], where it was found that the structure of the shock does not change as long as η is not too large.

---

[11] Hybrid models assuming an isothermal or polytropic equation of state [97], but also more intricate descriptions for the fluid temperature, as solving a heat equation for the electrons [128], have been used.

In the Maxwell equations, a Darwin (magnetostatic or magnetoinductive) model is employed,

$$\nabla \times \vec{B} = \frac{4\pi}{c} \vec{J}, \tag{49}$$

in which the displacement current is neglected so that the propagation of high-frequency waves is inhibited. This is appropriate for modeling low-frequency phenomena as the short timescales are neglected. It has been recently shown that the low-frequency modes related to the ion dynamics (which is the focus of this thesis and cosmic ray (CR) acceleration at collisionless shocks in general) are in excellent agreement with the full electromagnetic model [130]. The time evolution of the magnetic field is governed by Faraday's law,

$$\frac{\partial \vec{B}}{\partial t} = -c\,\nabla \times \vec{E}. \tag{50}$$

The electric field on the right hand side can be calculated by rearranging the electron momentum equation, Eq. (47). With the quasi-neutrality assumption, Eq. (46), and the electron bulk velocity from $\vec{J} = \vec{J}_i - \vec{J}_e = en(\vec{u}_i - \vec{u}_e)$ the electric field reads

$$\vec{E} = \frac{1}{e\,n} \left(\frac{(\vec{J} - \vec{J}_i) \times \vec{B}}{c} - \nabla p_e \right) + \eta\,\vec{J}. \tag{51}$$

Finally, Gauss' law for magnetism has to be fulfilled,

$$\nabla \cdot \vec{B} = 0. \tag{52}$$

To solve the Vlasov equation for the ion plasma component we use the PIC method, in which the distribution function is sampled by a large number of macro-particles. The equations of motion for these particles read

$$m_i\,\frac{d\vec{v}_l}{dt} = q_i \left(\vec{E} + \frac{1}{c}\,\vec{v}_l \times \vec{B} - \eta\,\vec{J} \right), \tag{53}$$

$$\frac{d\vec{x}_l}{dt} = \vec{v}_l, \tag{54}$$

where l denotes the index of the particle. The last term on the right hand side in Eq. (53) balances the resistivity term in the equation for the electron fluid. Note that these equations are formulated nonrelativistically, which is justified as $|\vec{v}| \ll c$ holds during the injection into DSA. A detailed description of the numerical implementation is given in Sec. 3.3.

3.2 Non-Dimensionalization

The above equations have to be expressed in dimensionless variables before discretizing them for the numerical implementation. As the hybrid model is treating the spatial and temporal scales defined by the ion dynamics, it is natural to express the variables in terms of quantities which are defining these scales. In the simulation time is given in units of inverse proton cyclotron frequency, ω_c^{-1},

$$\tilde{t} = \frac{t}{\omega_c^{-1}} \qquad \text{with} \qquad \omega_c = \frac{e\,B_0}{m_p\,c}, \tag{55}$$

where B_0 is the amplitude of the background magnetic field, which also defines the unit of measure for the magnetic field,

$$\tilde{B} = \frac{B}{B_0}. \tag{56}$$

Lengths are normalized to the ion skin depth, c/ω_p, with ω_p being the upstream proton plasma frequency,

$$\tilde{x} = \frac{x}{c/\omega_p} \qquad \text{with} \qquad \omega_p = \sqrt{\frac{4\pi\,n_0\,e^2}{m_p}}. \tag{57}$$

Here n_0 is the far upstream ion density which in turn is used for normalizing the density,

$$\tilde{n} = \frac{n}{n_0}. \tag{58}$$

Finally, velocities are given in terms of the Alfvén velocity, v_A,

$$\tilde{v} = \frac{v}{v_A} \qquad \text{with} \qquad v_A = \sqrt{\frac{B_0^2}{4\pi\,n_0\,m_p}}. \tag{59}$$

Other dimensionless variables are summarized below:

$$
\begin{aligned}
\text{charge} \qquad & \tilde{q} = \frac{q}{e} = Z \\[4pt]
\text{mass} \qquad & \tilde{m} = \frac{m}{m_p} = A \\[4pt]
\text{electric field} \qquad & \tilde{E} = \frac{E}{B_0\,v_A/c} \\[4pt]
\text{pressure} \qquad & \tilde{p} = \frac{p}{p_{\mathrm{mag},0}} = \frac{p}{B_0^2/8\pi} \\[4pt]
\text{temperature} \qquad & \tilde{T} = \frac{T}{B_0^2/8\pi n_0} = \frac{T}{m\,v_A^2/2}.
\end{aligned}
$$

The equations of the hybrid model introduced in Sec. 3.1 and expressed in dimensionless variables are presented in the Appendix A. Note that in the Darwin model the ratio $\omega_p/\omega_c = c/v_A$ is arbitrary and can only be evaluated by defining the properties of the system (ion density and background magnetic field). For typical parameters of the interstellar medium, $n_0 \approx 0.1\,\mathrm{cm}^{-3}$ and $B_0 = 3\,\mu\mathrm{G}$, one finds an ion skin depth of $c/\omega_p \approx 720\,\mathrm{km}$, the inverse cyclotron frequency is $\omega_c^{-1} \approx 35\,\mathrm{s}$, and the Alfvén velocity is $v_A \approx 20\,\mathrm{km/s}$.

3.3   Implementation

The PIC method (see, e.g., [131]) is used to solve the Vlasov equation, Eq. (45), for the ion plasma component. In this method the phase space is sampled by a large number of macro-particles, which have the same mass-to-charge ratio as the ions in the plasma and move according to Eqs. (53, 54). The ion charge and current densities are obtained from the positions and velocities of the particles and serve as source terms in the Maxwell equations for the fields. In this way the simulation is fully self-consistent.

Updating particle positions and velocities

To integrate the equations of motion, Eqs. (53, 54), for the simulation particles numerically they are discretized and leapfrogged in time,

$$\frac{\vec{x}^{n+1} - \vec{x}^n}{\Delta t} = \vec{v}^{n+1/2}, \tag{60}$$

$$\frac{\vec{v}^{n+1/2} - \vec{v}^{n-1/2}}{\Delta t} = \frac{q_i}{m_i} \left(\vec{E}^n + \frac{1}{c} \frac{\vec{v}^{n-1/2} + \vec{v}^{n+1/2}}{2} \times \vec{B}^n - \eta \vec{J}^n \right), \tag{61}$$

where the notation $\vec{x}^n = \vec{x}(n\,\Delta t)$ is used, with Δt being the time step. This discretisation is time-reversible and symplectic and is second order in time. While updating the particle positions is straightforward, obtaining the new velocity is more involved as $\vec{v}^n = \dfrac{\vec{v}^{n-1/2} + \vec{v}^{n+1/2}}{2}$ appears on the right hand side of Eq. (61). An efficient solution is provided by the Boris-algorithm [132]. In this algorithm the update of the velocity is divided into three steps,

$$\vec{v}^- = \vec{v}^{n-1/2} + \frac{q_i}{m_i} \frac{\Delta t}{2} \vec{E}^n \qquad \text{(half acceleration)} \tag{62}$$

$$\frac{\vec{v}^+ - \vec{v}^-}{\Delta t} = \frac{q_i}{m_i} \frac{\vec{v}^+ + \vec{v}^-}{2} \times \vec{B}^n \qquad \text{(velocity rotation)} \tag{63}$$

$$\vec{v}^{n+1/2} = \vec{v}^+ + \frac{q_i}{m_i} \frac{\Delta t}{2} \vec{E}^n \qquad \text{(half acceleration)}. \tag{64}$$

A detailed description of the implementation of the velocity rotation can be found in [131], hence we will refrain from repeating it here. The algorithm is efficient, simple and has an excellent long term accuracy as it conserves phase space volume [133]. It has become a wide spread solution for the numerical integration of charged particle trajectories. For stability, the time step should be chosen such that the Courant–Friedrichs–Lewy condition is fulfilled,

$$v_{\max} \Delta t \leq \frac{\Delta x}{2}, \tag{65}$$

where Δx denotes the cell size of the numerical grid for the fields. Note that for the correct initialization of the velocities and positions a half acceleration and velocity rotation step with $-\Delta t/2$ has to be performed initially to calculate $\vec{v}^{-1/2}$.

To compute the updated velocity, the electromagnetic fields have to be evaluated at the particle positions. Since the values of the fields are only stored at discrete grid points,

an interpolation from the grid to the particle position is necessary. This is shown in Fig. 7, where position of a simulation particle is depicted in red, the numerical grid is shown in black and the grid points are labeled by the indices i, j. We use a linear weighting also referred to as area weighting in the two-dimensional case. The areas shown in different shades of blue in the figure are used to calculate the weights assigned to the four grid points adjacent to the particle position. Formally and using the one-dimensional case for simplicity, the interpolation of the field to the particle position, x_l, can be written as

$$\vec{E}_l = \int \vec{E}(x)\, S(x, x_l)\, dx, \tag{66}$$

where $S(x, x_l)$ is the so-called shape function, which is normalized to unity, $\int S(x, x_l) dx = 1$. In higher dimensions the shape function can be written as a product of shape functions in each direction,

$$S(\vec{x}, \vec{x}_l) = S_x(x, x_l)\, S_y(y, y_l)\, S_z(z, z_l). \tag{67}$$

For the linear weighting the shape function reads

$$S(x, x_l) = \begin{cases} \frac{1}{\Delta x} & 0 \leq |x - x_l| \leq \frac{\Delta x}{2} \\ 0 & \text{otherwise.} \end{cases} \tag{68}$$

The weighting function can be calculated by integrating the shape function over the cell volume, yielding

$$W(x, x_l) = \begin{cases} \frac{\Delta x - |x - x_l|}{\Delta x} & 0 \leq |x - x_l| \leq \Delta x \\ 0 & \text{otherwise.} \end{cases} \tag{69}$$

To reduce the noise level even more, higher order shape functions can be employed, but the linear weighting provides a reasonable compromise between computational speed and noise level.

The weighting is not only important for the interpolation of the fields from the grid to the particle positions but also for the calculation of the plasma density, $n_i(\vec{x}, t)$, and ion current density, $\vec{J}_i(\vec{x}, t)$, as they are required for the computation of the electromagnetic fields. The reconstruction of these quantities from the positions and velocities of the macro-particles reads

$$n = n_i(\vec{x}, t) = \sum_{l=1}^{N_{\max}} S(\vec{x}, \vec{x}_l) \quad \text{and} \quad \vec{J}_i(\vec{x}, t) = \sum_{l=1}^{N_{\max}} q_i\, \vec{v}_l(t)\, S(\vec{x}, \vec{x}_l). \tag{70}$$

Here the summation is over all $N_{\max}$ macro-particles. Considering the discretization in time as well as in space, the ion density can be expressed as

$$n_i(\vec{x}_k, n\,\Delta t) = n_i^n(\vec{x}_k) = \sum_{l=1}^{N_{\max}} W(\vec{x}_k, \vec{x}_l^n), \tag{71}$$

where $\vec{x}_k = (i\,\Delta x, j\,\Delta y)$ denotes the position of the grid point. The computation of the ion current density deserves more attention, since the time staggering of velocities and
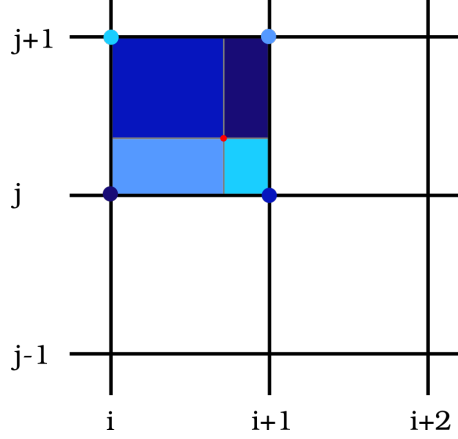
FIGURE 7: Schematic of the linear interpolation or area weighting. The position of a simulation particle is indicated in red while the numerical grid is shown in black. The areas shown in different shades of blue correspond to the weights assigned to the four grid points adjacent to the particle position, which are marked with the respective color.

positions, which are needed for the calculation, makes it non-trivial. We adopt a method proposed in [134]. The ion current density is calculated in the following way

$$\vec{J}_i^{\,n+1/2}(\vec{x}_k) = \frac{1}{2}(\vec{J}^- + \vec{J}^+) \tag{72}$$

$$= \frac{1}{2}\left(\sum_{l=1}^{N_{\max}} q_i\, \vec{v}_l^{\,n+1/2}\, W(\vec{x}_k, \vec{x}_l^{\,n}) + \sum_{l=1}^{N_{\max}} q_i\, \vec{v}_l^{\,n+1/2}\, W(\vec{x}_k, \vec{x}_l^{\,n+1})\right). \tag{73}$$

The inclusion of different ion species in the simulation is straightforward. They can be propagated independently and densities and currents can be evaluated separately. To account for the different abundances of the ions, each species is assigned a weight reflecting the abundance. This is then used to determine the total ion density and current density. Note that the ion current density is given at half-integer time steps while the density is calculated at integer time steps. However, for the calculation of the electric field both quantities are needed at the same time. Possible solutions to this problem will be discussed below as we describe the implementation of the numerical method to compute the fields.

UPDATING THE FIELDS

We solve the equations for the electromagnetic fields explicitly on an Eulerian grid using second-order finite difference stencils to discretize the derivatives. A detailed description of the discretized equations can be found in the Appendix A. Generally, the electromagnetic fields are updated from time step n to $(n + 1)$ using the moments of the distribution function, i.e., the ion density and current density.

To calculate the fields at the "new" time step $(n+1)$, the magnetic field is straightforwardly first updated to an intermediate time $(n + 1/2)$. This is done in accordance with the discretized Faraday's law, Eq. (50):

$$\vec{B}^{\,n+1/2} = \vec{B}^{\,n} - c\,\frac{\Delta t}{2}\,(\nabla \times \vec{E}^{\,n}). \tag{74}$$

With the magnetic field at $(n + 1/2)$ the electric field is evaluated at $(n + 1/2)$ using Eq. (51) in discretized form,

$$\vec{E}^{n+1/2} = \frac{1}{n_i^{n+1/2}} \left(\left(\vec{J}^{n+1/2} - \vec{J_i}^{n+1/2} \right) \times \vec{B}^{n+1/2} - \frac{1}{2} \nabla p_e^{n+1/2} \right) + \eta \, \vec{J}^{n+1/2}, \quad (75)$$

$$\text{with} \quad \vec{J}^{n+1/2} = \nabla \times \vec{B}^{n+1/2} \quad \text{and} \quad p_e^{n+1/2} = \left(n_i^{n+1/2} \right)^{\gamma}.$$

It is apparent that the electric field in Eq. (75) is a function of ion density, ion current density and magnetic field. Hence, we simply write

$$\vec{E}^{n+1/2} = \vec{F} \left(\vec{B}^{n+1/2}, n_i^{n+1/2}, \vec{J_i}^{n+1/2} \right) \quad (76)$$

to shorten the cumbersome expression above. Note, the density at the half-integer time step $(n + 1/2)$ can be obtained as an average, $n_i^{n+1/2} = \left(n_i^n + n_i^{n+1} \right)/2$. The updated electric field at $(n + 1/2)$ is used to obtain the magnetic field at the time step $(n + 1)$ analogue to Eq. (74). Finally, the new electric field at time step $(n + 1)$ is obtained as $\vec{E}^{n+1} = \vec{F}(\vec{B}^{n+1}, n_i^{n+1}, \vec{J_i}^{n+1})$. This step is, however, not straightforward because for the calculation of $\vec{E}^{n+1}$ the ion current at time step $(n + 1)$ is required which, in contrast to n_i^{n+1} and $\vec{B}^{n+1}$, is not known. Several different algorithms were put forward in the literature (see, e.g., [126] for an overview) to solve this problem. In our hybrid simulation code we have implemented two of them, the predictor-corrector method as well as a Bashford-Adams extrapolation of the ion current.

In the predictor-corrector method the calculation $\vec{E}^{n+1}$ does not follow Eq. (75), but its value is instead "predicted" using the value of the field at earlier times,

$$\vec{E}'^{n+1} = 2 \vec{E}^{n+1/2} - \vec{E}^n. \quad (77)$$

The predicted electric field, Eq. (77), is then used together with the magnetic field, $\vec{B}^{n+1}$, to propagate the ions, whereby the old positions and velocities are kept. From the new positions and velocities the moments of the distribution function are obtained on the grid. The available terms $n_i'^{n+3/2}$ and $\vec{J_i}'^{n+3/2}$ allow for the calculation of an updated electric field, $\vec{E}'^{n+3/2}$. This, in turn, is used to obtain the corrected field at time step $(n + 1)$,

$$\vec{E}^{n+1} = \frac{1}{2} \left(\vec{E}'^{n+3/2} + \vec{E}^{n+1/2} \right). \quad (78)$$

This field is then used to propagate the ions a second time in accordance with Eq. (61) using the old positions and velocities as starting point. Finally, the next iteration of the PIC cycle, which is shown schematically in Fig. 8 can be started. The PIC cycle can be summarized as follows: (i) the electromagnetic fields are interpolated to the positions of the simulation particles; (ii) the particle position and velocities are updated; (iii) using the new positions and velocities the ion density and current density are calculated on the grid; (iv) the current and density serve as inputs for the update of the electromagnetic fields. This cycle is then repeated until the simulation is finished.

While the predictor-corrector algorithm presented above is rather simple and has good
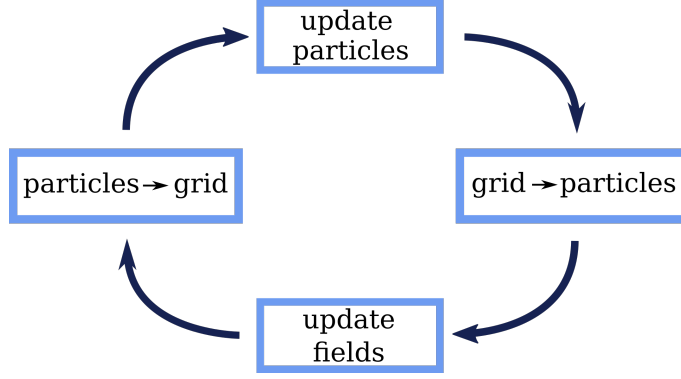
FIGURE 8: Scheme of the computational cycle of the particle-in-cell algorithm.

energy conserving properties, it comes at the price of high computational costs because the particles are propagated twice per time step. For large two-dimensional simulations, containing over 10^7 particles, this is very time-consuming because updating the particles contributes in large part to the computational time of the PIC cycle. Hence, an algorithm where the particles are pushed only once per time step is desirable. The solution is provided by a Bashford-Adams extrapolation of the ion current, which allows for the calculation of the ion current density, $\vec{J}_i^{n+1}$, using its values at earlier time steps,

$$\vec{J}_i^{n+1} = 2\,\vec{J}_i^{n+1/2} - \frac{3}{2}\,\vec{J}_i^{n-1/2} + \frac{1}{2}\,\vec{J}_i^{n-3/2}. \tag{79}$$

This method is used by default for two-dimensional simulations together with a fourth-order Runge-Kutta scheme for the propagation of the magnetic field. A detailed description is given in the Appendix A.

Boundary conditions

Attention has to be paid when particles are reaching the boundaries of the simulation box but also to the calculation of the electromagnetic fields at these boundaries. We have implemented different types of boundaries, to correctly account for the behavior of particles and fields under different conditions.

At periodic boundaries the particles leaving the simulation box are reintroduced at the other side of the box. Also the fields and moments of the distribution function are periodic at the boundary and fulfill

$$A_0 = A_{N-1} \qquad \text{and} \qquad A_N = A_1. \tag{80}$$

Here A is some quantity on the grid and N is the number of grid points.

Additionally, we have implemented a reflecting boundary for particles and fields. As a particle reaches this boundary its velocity component normal the boundary is reversed. Also the ion current density at the boundary has a change in the sign of the component normal to the boundary.

Finally, we have also included the option for an open boundary. At this boundary

particles can leave the simulation box[12]. However, in the modeling of acceleration at collisionless shocks the particles that are prone to leave the simulations box are the most energetic ones. At the same time, those are the particles we are most interested in. Therefore, we try to keep the number of particles leaving the box through the open boundary as small as possible by choosing an appropriate box size.

The open boundary also serves to inject new particles into the simulation domain. This is required because in our setup of the shock simulation the upstream plasma is flowing in one direction, see Fig. 11. Hence, new particles are injected at the open boundary to maintain a steady plasma flow with constant upstream ion density. In order to correctly inject a thermalized drifting plasma we initialize the velocities distributed according to a drifting Maxwellian flux, see [135] for a detailed discussion. The difference between a drifting Maxwellian and a drifting Maxwellian flux is negligible if the drift velocity is much larger than the thermal velocity, $v_0 \gg v_{\mathrm{th}}$. However, when simulating low Mach number shocks or including light, electron like, test-particles the exact reconstruction of the velocity distribution is important. To obtain particle velocities according to some distribution function, uniformly distributed random numbers in the interval $0 \leq R \leq 1$ are mapped to the respective distribution function. This map is provided by inverting the cumulative distribution function, which for the case of a drifting Maxwellian flux reads

$$F(v) = \frac{\int_{v_{\mathrm{cl}}}^{v} v' \exp\left((v' - v_0)^2\right) \, \mathrm{d}v'}{\int_{v_{\mathrm{cl}}}^{v_{\mathrm{cu}}} v' \exp\left((v' - v_0)^2\right) \, \mathrm{d}v'}, \tag{81}$$

where v_0 denotes the drift velocity and v_{cl} and v_{cu} are lower and upper limits for the velocity. In general these limits are $v_{\mathrm{cl}} = 0$ and $v_{\mathrm{cu}} \to \infty$, yielding

$$F(v) = \frac{\exp\left(-v_0^2\right) + \exp\left(-(v - v_0)^2\right) + \sqrt{\pi}\, v_0 \left(\mathrm{erf}(v - v_0) + \mathrm{erf}(v_0)\right)}{\exp\left(-v_0^2\right) + \sqrt{\pi}\, v_0 \left(1 + \mathrm{erf}(v_0)\right)}. \tag{82}$$

For a random number R in the interval $[0, 1)$ we invert $R = F(v)$ in order to obtain velocities with the right distribution. This cannot be done analytically. Hence, the cumulative distribution function is calculated numerically for discrete values of v and a linear interpolation is used to obtain the particle velocity from the random number, R.

The positions of all boundaries for the simulation of a collisionless shock are indicated in Fig. 9, where the parallelization strategy is shown. Note that in addition to the different types of boundaries presented above the parallelization requires an additional internal boundary, where particles are collected to be communicated to other processes and values of the fields at the boundary can be exchanged.

Parallelization and Load balancing

For large two- or three-dimensional simulation boxes with a reasonable number of particles per cell the total number of simulation particles can easily exceed a billion. As the numerical effort of PIC simulations scales with the number of particles, it is not feasible to

---

[12]   As only ions are treated using the PIC method, particles of opposite charge do not have to be removed to maintain neutrality.
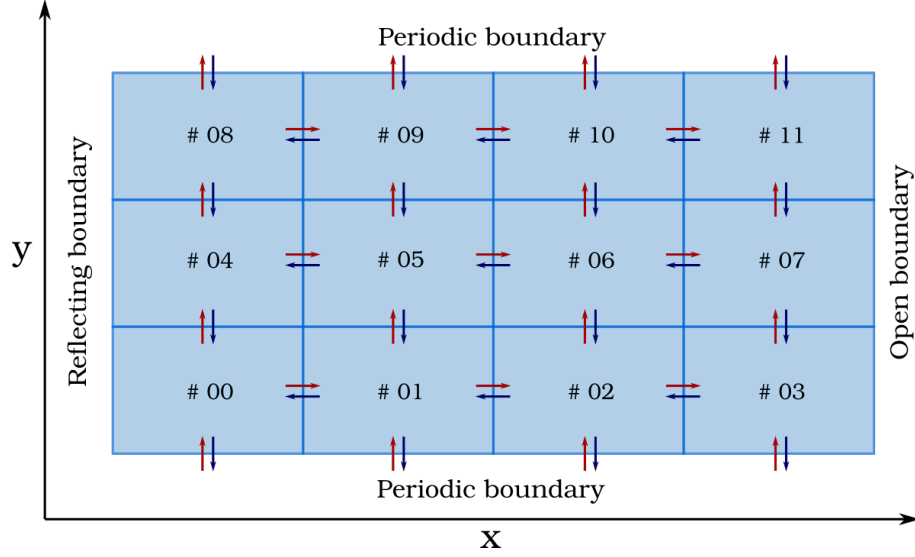
FIGURE 9: Sketch of the parallelization strategy: the simulation box is divided into a number of subdomains, which can be processed in parallel. Communication via MPI routines, denoted by red and blue arrows, is necessary to exchange data between neighboring domains.

run these large simulations on a desktop computer. Therefore, an efficient parallelization is needed in order to use the parallel compute capabilities of modern supercomputers. The hybrid algorithm presented above is local and, therefore, allows for parallelization via domain decomposition.

The general idea of this approach is illustrated in Fig. 9. The grid is divided into several subdomains, each of which is assigned to a process. Each process stores the necessary data, i.e., the particle data as well as all data stored on the numerical grid (fields, densities, etc.). We use the Message Passing Interface (MPI) to implement the parallelization. The simulation is initialized on $N^{\mathrm{cores}} = N_x^{\mathrm{cores}} \times N_y^{\mathrm{cores}}$ cores, where N_x^{cores} and N_y^{cores} denote the number of subdomains in x- and y-direction. While the particle positions and velocities can be updated on each subdomain independently, communication between neighboring domains (represented in Fig. 9 by the red and blue arrows) is necessary. For example, the data of particles crossing the domain boundaries has to be exchanged. These particles are identified during the update of the positions, collected and then sent to the respective neighboring domains using MPI routines. Additional communication routines are invoked after depositing the ion charge and current density on the grid to obtain the values at the boundaries (indicated by a darker shade of blue in Fig. 9). A communication of the values at the domain boundaries is also necessary during the calculation of the fields.

To quantify the scaling behavior we have performed a series of simulations for a plasma initialized with an upstream bulk velocity of $v_0 = 10\,v_A$ in a box with periodic boundaries in each direction. Simulations were performed using a two-dimensional (2D) setup with a grid spacing of $\Delta x = \Delta y = 0.5\,c/\omega_p$ and 25 particles per cell. We have investigated the strong scaling for a simulation box with the size $L_x \times L_y = 640 \times 400\,(c/\omega_p)^2$ and measured the wall time required for 1000 time steps on various numbers of subdomains
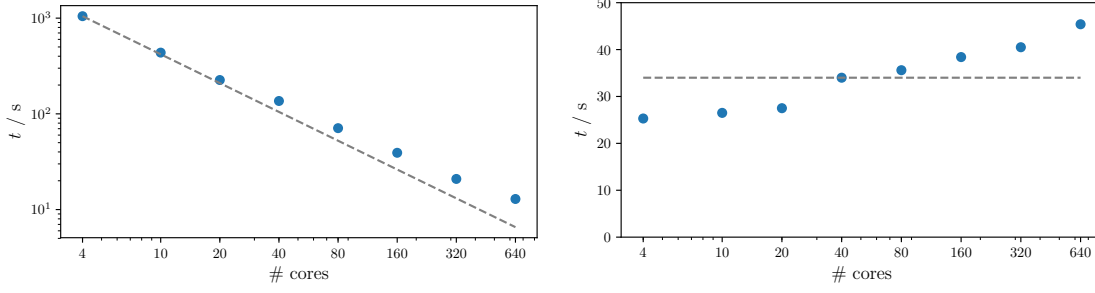
FIGURE 10: Parallel scalability of the hybrid simulation code. On the left the strong scaling behavior is plotted, while on the right the weak scaling is depicted.

and corresponding numbers of processor cores[13]. The result is plotted in the left panel of Fig. 10. The scaling with the number of cores is almost ideal up to 20 cores (1 CPU), while for higher core counts the parallel scaling efficiency drops. This is caused by the communication overhead as for up to 20 cores only one CPU is used, while for higher core counts communication between different CPUs and for more than 40 cores even communication between different nodes is necessary.

Additionally, the weak scaling behavior has been analyzed, which is important if large systems have to be investigated. Here we increase the size of the simulation box proportionally to the number of cores, keeping the load per core, i.e., the number of simulation particles per core constant (160000 particles per core were used). The result is shown in the right panel of Fig. 10. In the ideal case the wall time should remain constant, however, a deviation from the ideal behavior can be observed. A clear transition from the usage of only one CPU to more CPUs is visible as an increase in the wall time. When using more nodes the weak scaling efficiency decreases again due to the communication overhead. Despite the critical comments above, our numerical code has good strong and weak scaling behaviors and is suited to tackle large simulations on modern supercomputers.

From a computational point of view the numerical routines, handling the particle-grid connection, are the most time-consuming. For this reason the parallelization is efficient if the number of simulation particles on each subdomain is similar. A large load-imbalance, i.e., when some processes contain a much larger number of simulation particles, will result in a longer duration of the particle propagation step for those processes and the others will be waiting. This would waste valuable computational resources. Since in simulations of collisionless shocks the density in the downstream region is about four times higher than in the upstream, a serious load imbalance can be expected if equally sized subdomains are used. To enable load balancing in the simulation, the domain sizes are adjusted dynamically during the simulation. For one-dimensional simulations this is done by modifying the domain boundaries every few hundred time steps, changing the size by a few grid points and sending the grid and particle data to the neighboring domain. For the 2D simulation setup, we implemented a similar procedure and adjust the size of the subdomains only in the direction of the propagation of the shock. This prevents more than one domain being

---

13   Simulations were performed on the HLRN supercomputing center using the HLRN-III and HLRN-IV systems. The scaling results presented here were run on the latter system. Each node is equipped with two Intel Skylake Gold 6148 CPUs, totaling to 40 cores per node.

adjacent in each direction. While other methods of load balancing have been presented in the literature for arbitrary geometries [136, 137] this solution is sufficient since our simulations are focused on a planar shock geometry.

Data handling and Postprocessing

In order to extract useful information from the simulation, the coordinates and velocities of the simulation particles as well as the fields have to be saved and postprocessed. We use the Hierarchical Data Format (HDF5) [138] for saving the simulation data. The possibility to save the data in a hierarchical form, similar to a file system and writing data in parallel makes it suitable for our application. We use separate files for saving particle and grid data, with the simulation time encoded in the file name. For the particles one file for each species is written, with the file name corresponding to the species, e.g., `proton_100.000000.h5`. Additional to the data of the particles (indices, weights, positions, and velocity) the charge and mass of the particle species are saved as attributes in the file.

Files containing the data which is stored on the numerical grid are named, for example, `grid_100.000000.h5`. They also include attributes describing the simulation box, such as grid size, number of grid points in each direction and cell size. For each vector field the x, y, and z-components are stored separately as two-dimensional datasets. The hierarchical structure of the data allows to specify a group name for each quantity that is stored. Furthermore, we provide the option to save trajectories of simulation particles or the data of particles that cross a specific plane in the simulation.

The files can be read to continue a simulation but also for postprocessing of the data, which is performed with the help of various python scripts that also handle the visualization and rely mainly on the `h5py`, `numpy`, and `scipy` libraries. Postprocessing routines include the calculation of phase space distributions, velocity distributions and energy spectra.

For a better understanding of the underlying physical processes, it can be useful to follow the trajectories of some simulation particles. This can be done either by choosing a number of particles at random or by selecting a population of particles, (e.g., the ones that are accelerated to high energies) in postprocessing. In the latter case the simulation has to be run twice. After the first run the particles of interest can be identified by their unique index. And in the second run the trajectories of these particles are saved. Here it is important that the simulation is exactly reproducible, which is guaranteed by prescribed seeds of the random number generators. Additionally to the positions and velocity components we save the fields at the ion positions.

Initialization

We use the hybrid code to model collisionless shocks and investigate particle acceleration in these environments. Different simulation setups can be used to excite shocks in numerical simulations. A compilation can be found, for example, in [139, Fig. 4]. We use the injection or piston method, where a plasma is flowing with a super-sonic and super-Alfvénic velocity
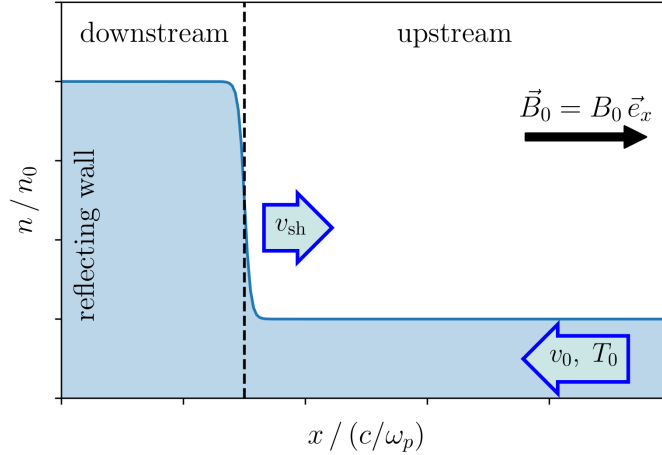
FIGURE 11: Sketch of the simulation setup: the simulation is initialized by sending a plasma with a super-Alfvénic (and super-sonic) mean upstream flow velocity against a reflecting wall. The background magnetic field is typically initialized uniformly with an angle θ_{Bn} to the shock normal.

towards a reflecting wall, which is placed at $x = 0$ in our simulation. The mean upstream flow velocity is denoted by v_0, which is oriented in $-x$ direction. As the plasma is reflected from the boundary, a shock forms due to the interaction of the counterpropagating flows. The shock propagates in x-direction, while the downstream plasma is at rest. A sketch of the setup is presented in Fig. 11. The simulation is initialized with a plasma of uniform density, n_0, and temperature, T_0, in a background magnetic field, $\vec{B}_0$. The ions as well as the electron fluid are assumed to be in thermal equilibrium. We have restricted ourselves to the case $\beta_e = \beta_i = 1$, where $\beta = p_{\mathrm{th}}/p_{\mathrm{mag}} = n\,k_B\,T/(B^2/8\pi)$ denotes the ratio of thermal to magnetic pressure.

Upon the start of the simulation a parameter file, `simulation.param`, is read. An example is given below. This file contains the required information about the simulation setup. In this file the dimensions of the simulation box, $L_x \times L_y$, (`GRID SIZE X, Y`) are given as well as the cell size (`DELTA X, Y`) and information important for the parallelization (`N PROCS X, Y`). The direction of the background magnetic field is specified via the angle θ_{Bn} between the magnetic field and the shock normal (see `THETA_BN` in the parameter file). Usually the field is taken to be in the simulation plane but also out of plane configurations are possible. A non-homogeneous background magnetic field can be initialized, too (see Chapter 5), as long as it fulfills Eq. (52). Furthermore, the file, `simulation.param`, specifies parameters which are necessary for the initialization of the simulation particles. Those are the number of particles per cell (`PARTICLES PER CELL`), the mean upstream flow velocity (`FLOW VELOCITY`) and ion temperature (`ION TEMP`). Also the initial temperature of the electron fluid (`ELECTRON TEMP`) as well as the value of the anomalous resistivity (`RESISTIVITY`) are given in `simulation.param`.

After reading the parameter file the size of the subdomains is calculated, each subdomain is initialized on the respective processing core and the necessary memory is allocated. Depending on the value of `START TIME` either an existing simulation is continued by reading the particle positions and velocities and field data from file or, in the case of `START`

TIME $= 0$, a new simulation is initialized. In this case the simulation particles are distributed on the grid and the initial fields are calculated. We initialize the particles with a spatially uniform distribution by scattering them equidistantly across the grid. The velocities are set according to normal distributed random numbers for each velocity component. The standard deviation of the normal distribution is determined by the ion temperature and mass. The mean velocity for the y- and z-components is zero while the mean velocity for the x-component is given by value for the upstream flow velocity. We use prescribed seeds for the random number generators that are unique for each subgrid. This allows for an exact reproducibility of the simulations and avoids artificial periodicities.

The current version of the code is suitable for simulations including multiple particle species. For each species the mass, charge and weight, reflecting the abundance, are specified in the main `.cpp` file. The weight is important for the calculation of the total ion density and current, if it is set to zero the corresponding particle species is treated as "test-particles". After the initialization of the simulation particles the initial moments of the distribution function are calculated, which allows for the computation of the initial electric field according to Eq. (51) as at later times during the simulation. Since the plasma is initialized with a homogeneous density the ∇p_e term vanishes initially.

The whole simulation procedure is summarized in the flow chart in Fig. 12.

```
 1  ##############################################################################
 2  #                                                                            #
 3  #                          SIMLATION PARAMETERS                              #
 4  #                                                                            #
 5  ##############################################################################
 6  #                              WRITING
 7
 8  OUTPUT PATH:   Test/output/
 9
10  ##############################################################################
11  #                              GRID
12
13  GRID SIZE X:   20000.
14  GRID SIZE Y:   200.
15  DELTA X:     0.5
16  DELTA Y:     0.5
17  NO PROCS X:    200
18  NO PROCS Y:    10
19  THETA_BN:      15.
20
21  ##############################################################################
22  #                              PARTICLES
23
24  PARTICLES PER CELL: 25
25  FLOW VELOCITY:     -10.
26  ION TEMP:          1.
27  ELECTRON TEMP:     1.
28  RESISTIVITY:       0.001
29
30  ##############################################################################
31  #                              TIME
32
33  START TIME: 0
34  END TIME:    400.
35  WRITE STEP: 10.
```

LISTING 1: Example for the file `simulation.param` which contains the parameters necessary for initializing the simulation
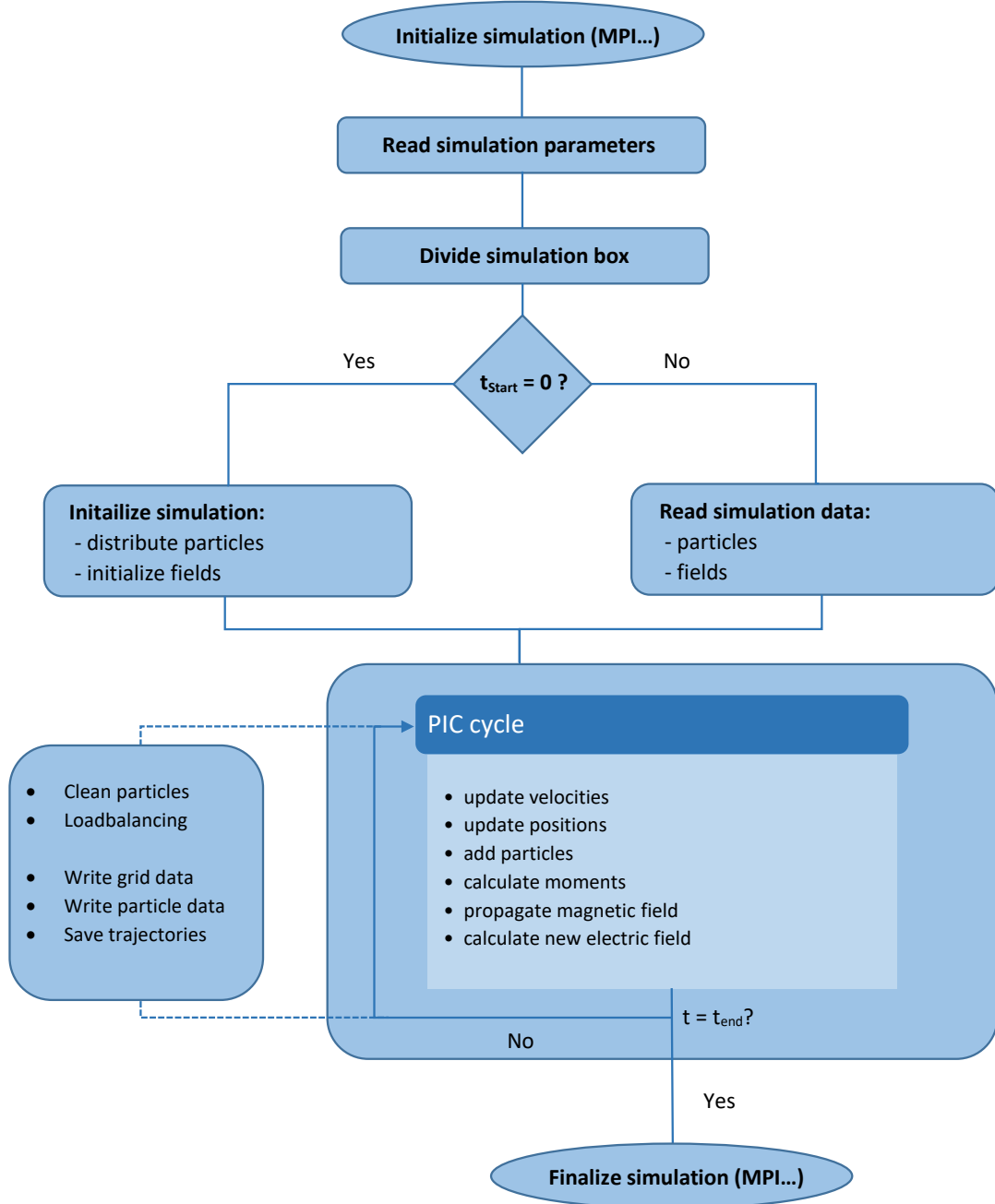
Figure 12: Flow chart of the simulation procedure. After reading the parameter file and the division of the simulation box into the subgrids for parallelization, the particles and fields are initialized or read from file. The PIC cycle is repeated as often as needed and the particle and grid data is saved from time to time.

CHAPTER 4

Mass-to-Charge Dependence as Key for Understanding the Injection

4.1 Motivation

According to current understanding, galactic cosmic rays (CRs) originate most likely from supernova remnants (SNRs), where they are presumably energized via diffusive shock acceleration (DSA). The DSA theory has recently faced a serious challenge when the accurate processing of the data for the energy spectra of primary CRs collected by the balloon-born detector ATIC-2 [28] indicated that the proton spectrum is significantly steeper than that of helium nuclei (He). This finding has been confirmed by the high-accuracy PAMELA and AMS-02 observations [7, 5], which measured a difference of $\Delta q \simeq 0.1$ in the spectral indices of these elements. The spectral difference can also be seen when plotting the flux ratio of different elements instead of the single-particle spectra. Figure 13 below shows the proton-to-helium ratio, measured by different experiments, as function of the particle rigidity,

$$\mathcal{R} = p\,c/Z\,e. \tag{83}$$

Here p denotes the momentum, c the velocity of light, and Ze is the charge of the ion. Although these measurements [7, 5] are limited to rigidities up to $\mathcal{R} \approx 1$ TV, there are other observations [2] indicating that this scaling is likely to continue to higher rigidities. The rigidity spectra of carbon (C) and oxygen (O) show a similar difference in the spectral index compared to protons [8], see Fig. 13. While a difference of $\Delta q \simeq 0.1$ in the spectral indices may appear as small, it still challenges the leading hypothesis of CR acceleration by DSA in supernova remnant shocks.

The problem becomes obvious when rewriting the equations of motion of charged particles in arbitrary electric and magnetic fields in terms of particle rigidity, instead of momentum $\vec{p}$:

$$\frac{1}{c}\frac{d\vec{\mathcal{R}}}{dt} = \vec{E}\left(\vec{r}, t\right) + \frac{\vec{\mathcal{R}} \times \vec{B}\left(\vec{r}, t\right)}{\sqrt{\mathcal{R}_0^2 + \mathcal{R}^2}}, \tag{84}$$

$$\frac{1}{c}\frac{d\vec{r}}{dt} = \frac{\vec{\mathcal{R}}}{\sqrt{\mathcal{R}_0^2 + \mathcal{R}^2}}. \tag{85}$$

Here $\mathcal{R}_0 = A\,m_p\,c^2/Z\,e$, with A being the atomic number and m_p the proton mass. $\vec{E}\left(\vec{r}, t\right)$ and $\vec{B}\left(\vec{r}, t\right)$ denote the spatially and time-dependent electric and magnetic fields, respectively, which can be completely arbitrary. Hence, the equations above do not only apply to the acceleration of CRs in the environment of a SNR shock[14] but also to their propagation

---

[14] The specific mechanism behind the acceleration (DSA) is electromagnetic in nature.
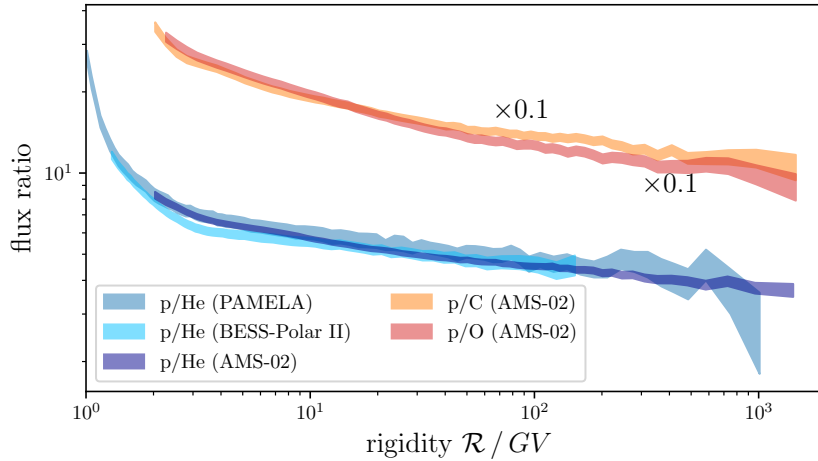
FIGURE 13: The p/He, p/C, and p/O ratios as a function of particle rigidity. The data is taken from [5, 7, 3, 8].

through the turbulent interstellar medium (ISM) to an observer, including an eventual escape of the accelerated CRs from our galaxy.

According to Eqs. (84) and (85), all ion species have similar trajectories in the phase space $(\vec{r}, \vec{\mathcal{R}})$ if they are energetic and $\mathcal{R} \gg \mathcal{R}_0 = A m_p c^2 / Z e$ is fulfilled. Hence, ions entering the acceleration process at some $\mathcal{R} \gg \mathcal{R}_0$ in a time-independent ratio should maintain this ratio even after acceleration to higher energies. However, the measurements with the ATIC-2, PAMELA, and AMS-02 instruments, see Fig. 13, show that the proton-to-helium ratio is a decreasing function of particle rigidity. Furthermore, the recent AMS-02 observations have revealed the same trend for the p/C and p/O ratios. This behavior is clearly in contradiction to the argument above. Note that in the range of low rigidities, $\mathcal{R} \leq 10$ GV, the rest mass rigidity ($\mathcal{R}_0 \approx 1$ GV for protons) cannot be neglected, and the arguments above do not apply. But the rigidity dependence of the flux ratio at higher rigidities is an anomaly posing a challenge to the theory of CR origin.

In the following we will introduce possible explanations of this anomaly and discuss potential shortcomings of these explanations. We anticipate, that our hybrid simulations focused on the injection phase of the DSA, where elemental similarity does not apply, and analytic modeling allow us to reconcile the high-precision measurements of elemental spectra with different mass-to-charge (A/Z) ratios with the DSA. The main results of this work have been published in [29].

4.2 Explanations of the Anomaly

Mainly three different ideas have been considered to explain the paradox outlined above: (i) contributions from several SNRs with different p-He mixes and spectral slopes [140]; (ii) CR spallation in the ISM that would modify Eq. (84) in different ways for different elements and introduce rigidity-dependent particle sources and sinks [141]; (iii) time dependence of the CR acceleration [142, 143].

The first scenario is not testable because the exact properties of the acceleration sites

are not known. Moreover, it fails to explain why the accelerated particle spectral slopes of carbon and oxygen are similar to that of helium. Meanwhile, according to [144], spallation effects cannot fully explain the p/He rigidity dependence, either. This is now also affirmed by the AMS-02 measurements of the carbon and oxygen spectra. Hence, the time-dependence of the initial acceleration phase, the so-called injection, remains as probable explanation of the anomaly. Two different theories were proposed in this context. In [142] it was assumed that the medium in which the shock propagates is inhomogeneous, with the p/He ratio changing with distance to the SNR progenitor star. As higher rigidities are dominated by earlier times of the acceleration history, one could expect a p/He ratio decreasing with rigidity if the helium contribution was higher in the regions closer to the SNR progenitor star. Another proposal is based on the simple argument that the shock velocity decreases with time, making the acceleration time-dependent. Since the spectral index depends on the shock compression ratio, which in turn depends on the shock Mach number, see Eq. (33), the measured proton-to-helium ratio might be explained if the injection itself is a mass-to-charge and Mach number dependent process. This idea was proposed in [102] in form of an analytic theory of the injection. The authors of [143] applied the results of [101, 102] to fit the PAMELA measurement for $A/Z = 2$ (specifically to He^{2+}, but also valid for fully ionized carbon and oxygen), yielding an excellent agreement in the rigidity range $2 < \mathcal{R} < 200$ GV. Following the arguments put forward in [102, 143], the elemental "anomaly" in the rigidity spectra is a result of the intrinsic properties of the injection mechanism, and no additional assumptions have to be made to explain it. In turn, the high-precision measurements of the flux ratios of different elements provide a valuable tool for understanding the physics of particle injection into the DSA.

The theoretical calculations of the p/He rigidity spectra [143] are based on an analytic theory [101, 102] that has some freedom in choosing the seed particles to be accelerated in the DSA. The source of the seed particles has triggered heated discussions. It was argued that those are either shock reflected ions [62], or hot ions evaporating from the shocked downstream plasma back to the upstream [91, 26]. Simulations can remove this uncertainty, allow to obtain self-consistent injection rates for different elements, and improve the general understanding of the injection mechanism.

In the following we will show that the measured flux ratios are not in contrast with the theory of CR origin in SNRs but support it. Note that, as stated in [29]: "it is crucial to use the rigidity dependence of the fractions of different species as a primary probe into the intrinsic properties of CR accelerators. Unlike the individual spectra, the fractions are unaffected by CR propagation, reacceleration, and losses in the galaxy, as long as spallation is negligible."

4.3 Simulation Setup

It has already been established analytically [101] as well as in numerical simulations [27, 145] that the injection into the DSA is only efficient at quasi-parallel shocks. Hence, we focus on this shock geometry with a special emphasis on parallel shocks. The results presented below are obtained in simulations where the spatial dimension is reduced to the

shock propagation direction (but all components of the velocity and fields are kept). This allows to dramatically increase the particle statistics, i.e., the number of simulation particles per cell, and to perform detailed parametric studies over shock parameters, necessary to test the injection bias, within finite time. While the reduced dimensionality prohibits some effects, such as shock rippling[15], it still captures the important aspects of the acceleration and has proven as a valuable tool for understanding ion acceleration at collisionless shocks (see, e.g., [122, 26, 147]). Additionally, the high computational requirements of injection studies in two-dimensional simulations allow only for small transverse box sizes rendering these simulations quasi-one-dimensional.

Our initial setup is depicted in Fig. 11. To investigate the mass-to-charge dependence of the injection we introduce in the simulation several different ion species with number ratios corresponding to the amount of particles in the ISM. The fraction of helium ions with respect to the main proton component is high, $\sim 10\%$. Therefore, helium ions are dynamically important and should be treated self-consistently. Carbon and oxygen ions, on the other hand, have fractions of $\sim 0.04\%$ with respect to protons, and can almost be considered as test-particles.

The upstream plasma is initialized with all ion species being in thermal equilibrium with $\beta = 1$. The background magnetic field is set parallel to the shock normal $\vec{B}_0 = B_0 \, \vec{e}_x$. The extension of the one-dimensional (1D) simulation box is $L_x = 12 - 48 \cdot 10^3 \, c/\omega_p$, depending on the upstream bulk velocity, v_0. We use a spatial resolution of $\Delta x = 0.25 \, c/\omega_p$, with at least 100 particles per cell for each species. The time step is chosen as $\Delta t = 0.01/M_0 \, \omega_c^{-1}$, where $M_0 = |v_0|/v_A$. All numerical parameters have been checked for convergence.

4.4 RESULTS

FIELDS

In the simulation the plasma is initialized to move with a bulk velocity, v_0, in $-x$-direction. A shock wave forms after the reflection of the plasma stream from the left boundary and the shock propagates in x-direction. The upper panels in Fig. 14 show the ion density and the transverse component of the magnetic field, B_y, as functions of spatial coordinate and time. The shock position is clearly visible as a jump in the plasma density and strength of the magnetic field. The sudden increase in density is predicted by the Rankine-Hugoniot jump conditions, Eq. (11), where a compression ratio of $r = 4$ is found in the limit of strong shocks. For shocks strongly modified by CRs rays even higher compression ratios can be achieved (see, e.g., [148, 149]). In this simulation, initialized with $v_0 = 10 \, v_A$, the mean downstream density value of $n = 4.1 \, n_0$ only marginally exceeds the value predicted by the Rankine-Hugoniot conditions.

After the shock has developed (this takes time on the order of a few tens of inverse proton gyrofrequencies), the position of the shock on larger timescales increases almost

---

[15]   Shock rippling has been investigated in two-dimensional hybrid simulations, see, e.g., [146], but a comprehensive analysis of the microphysics at the shock front requires a fully kinetic treatment.

linearly with time and the average shock velocity is nearly constant. The mean shock velocity, v_{sh}, in the downstream (simulation) rest frame is obtained by fitting a linear function

$$x_{\mathrm{sh}} = v_{\mathrm{sh}}\, t + x_0 \tag{86}$$

to the shock position, x_{sh}. This quantity is calculated from simulation data as the point where the density is first (as seen from the upstream) exceeds three times the upstream density,

$$x_{\mathrm{sh}} = \max_{n(x)>3\,n_0} x. \tag{87}$$

The insert in Fig. 14 shows the periodical reformation of the shock, occurring on a relatively short timescale. This behavior has been observed in earlier hybrid simulations of quasi-parallel collisionless shocks [150, 123, 151, 97].

The transverse component B_y of the magnetic field, plotted in the right and lower panels of Fig. 14, increases upon shock crossing. The same holds for B_z and for the magnitude of the magnetic field. As the field lines are frozen into the plasma, the magnetic field is compressed upon the transition to the denser downstream medium, see the lower panel of Fig. 14, where the transverse components of the magnetic field $(B_y(x), B_z(x))$ as well as the ion density at $t = 400\,\omega_c^{-1}$ are plotted. The parallel component of the magnetic field, which corresponds to the background magnetic field in the parallel shock geometry, is not compressed and remains constant in the one-dimensional simulation setup. The circularly polarized Alfvén waves present in the upstream are excited by streaming particles in the upstream either via resonant ion cyclotron streaming instability [107] (see also Sec. 2.3.4) or Bell's nonresonant CR current-driven instability [112] (see also Sec. 2.3.4). These waves are then advected with the plasma and compressed upon shock
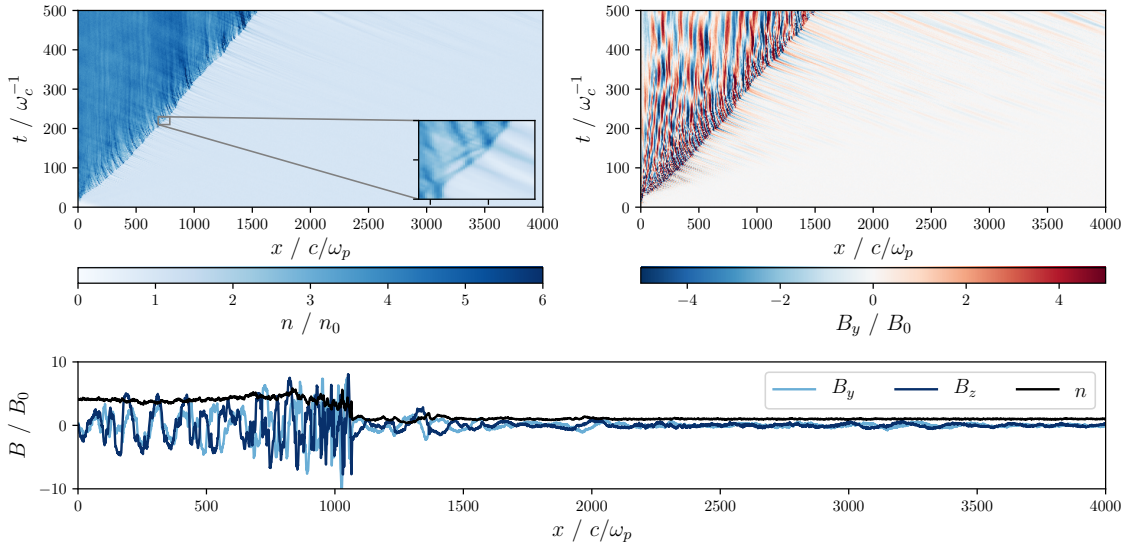

FIGURE 14: Ion density $n_i(x,t)$ (left) and y-component of the magnetic field $B_y(x,t)$ (right) for a simulation with $v_0 = 10\,v_A$. For both quantities a jump is visible at the shock position. The shock front is propagating in x-direction as the simulation is performed in the downstream rest frame. The lower panel shows the transverse components of the magnetic field $(B_y(x), B_z(x))$ as well as the ion density at $t = 400\,\omega_c^{-1}$.

transition and serve as scattering centers for energetic particles.

While the resonant and nonresonant excitation of circularly polarized waves upstream of the shock transition is well known and has been investigated analytically [108, 112] as well as by numerical simulations [26, 152, 27], less attention has been paid to the possible influence of additional ion species on the wave excitation. Especially helium ions, which contribute with approximately 10% to the composition of the ISM, might influence the wave generation. Typically, the waves driven by fully ionized helium via the resonant cyclotron interaction should be two times longer than the waves driven by protons. This can be relevant because in wave-particle interactions the resonance condition is usually more important than the wave amplitude (see also discussion in [29]). Additionally, nonlinear wave-wave interactions between proton and helium generated waves are possible due to their integer wavelength ratio. Since the injection of ions into the DSA is regulated by the self-consistent excitation of waves, it can be significantly influenced by the presence of an abundant helium population.

In order to investigate this influence we have compared the magnetic field and particle energy spectra obtained in a simulation with self-consistently included He^{2+} with the corresponding quantities collected for a pure hydrogen plasma, in which He^{2+} ions were included as test-particles. The results are plotted in Fig. 15. The spectra shown in the left panel are computed by a Fourier transform of the y-component of the magnetic field and are taken after the simulation has been running for $500\,\omega_c^{-1}$. A distinct difference in the wave spectra is the additional peak at small wavenumbers that appears if the helium population is included self-consistently. This indicates the presence of additional waves with longer wavelengths. The downstream energy spectra of the particles, shown in the right panel of Fig. 15, are also significantly influenced by the presence of helium ions. The enhanced number of downstream protons with high energies and an increase in the number of helium ions near the cutoff confirm the critical role of the self-consistent treatment of the He^{2+} population. The energy spectra of different ion species will be addressed in more detail below in this chapter.

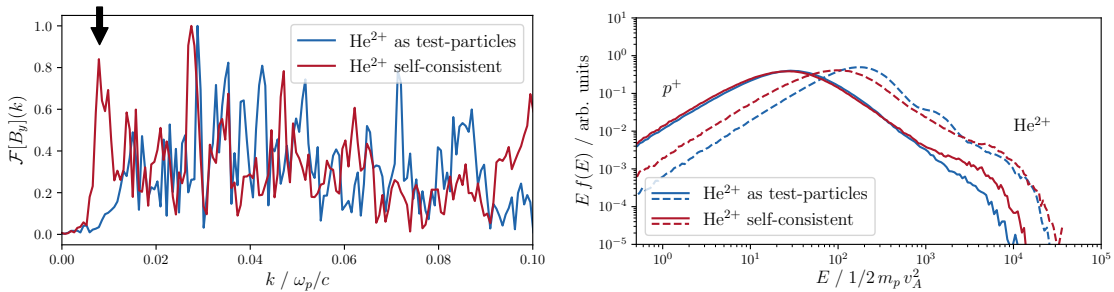The above results indicate that when investigating the injection of ions into the DSA

FIGURE 15: (left) Wave spectrum (Fourier transform of $B_y(x)$) for a simulation with helium ions as test-particles (blue) and treated self-consistently (red) measured at $t = 500\,\omega_c^{-1}$ for an initial upstream bulk velocity of $v_0 = 10v_A$. If a He^{2+} population is included, an additional Fourier component at small k (long wavelength) is present. (right) Downstream energy spectra of protons and helium ions calculated at the same time for the two setups.

the population of helium ions—even if it makes up only about ten percent of the ISM— should be taken into account not as test-particles in the proton-driven turbulence but rather self-consistently. In this way the additional population of particles with a different mass-to-charge ratio can drive unstable waves upstream of the shock, enriching the wave spectrum with additional components.

It should be noted that some of the past hybrid simulations of collisionless shocks addressing the acceleration of alpha particles have included them self-consistently [147, 153, 154, 155]. In some other cases they were made dynamically unimportant by dramatically reduced abundances [156]. In our particular study of the elemental selectivity of injection we use a realistic composition of the plasma consisting of ion species with number ratios corresponding to the amount of particles in the ISM and treat all ion species self-consistently.

Phase Space

In the following we will focus on simulations that include besides with protons and helium ions also carbon and oxygen ions with charge states $Z = 1$ and $Z = 2$. In Figure 16 we plot the distributions of ions in the phase plane, $f(x, v_x)$, for a simulation with an upstream velocity of $v_0 = 10\,v_A$. The snapshots are taken at $t = 1000\,\omega_c^{-1}$, long after the shock had developed. The transition from the upstream medium to the hot and turbulent downstream is visible at $x_\mathrm{sh} \approx 2970\,c/\omega_p$ in the center of each frame. Far upstream of the shock, the velocity distribution is centered around the upstream bulk velocity $v_x = -10\,v_A$ and the plasma is relatively cold. Since the ions are in thermal equilibrium, the width of the phase space distribution $f(x, v_x)$ in the upstream is narrower in the v_x direction for ions with higher masses. The shock transition itself is most prominent in the proton phase space while it is less visible in the O^{2+} and C^+ distributions. The width of the ion distribution close to the shock transition is determined by the Larmor radius of the respective ion species, which can be expressed as $r_L = \dfrac{A}{Z}\dfrac{v_\perp}{v_A}\,(c/\omega_p)$. Hence, the length of the transition increases with the mass-to-charge ratio. As $v_\perp$ is somewhere between $v_\mathrm{th} = v_A$ and v_0, the width of the particle distribution in the vicinity of the shock transition is on the order of a few proton skin depths for protons, while for C^+ ions it equals to several tens of proton skin depths. Populations of He^+ and O^{2+} ions with velocities close to the upstream bulk velocity but directed towards the upstream, are produced by a reflection from the shock front. An increase in the width of the velocity distribution upon shock crossing indicates an abrupt change in the temperature. In the downstream medium the velocity distribution is centered around $v_x = 0$ since the simulation is performed in the downstream rest frame. As the directions of the ion velocities are randomized upon shock crossing, the width of the velocity distribution is almost the same for all ion species, yielding a mass proportional downstream temperature predicted by the Rankine-Hugoniot conditions, Eq. (13). Energetic particles with negative or positive velocities that are considerably larger than the thermal velocity are present in the phase space distribution for all particle species. These particles have already gained some energy and by repeatedly crossing the shock a further energy increase via DSA is possible.
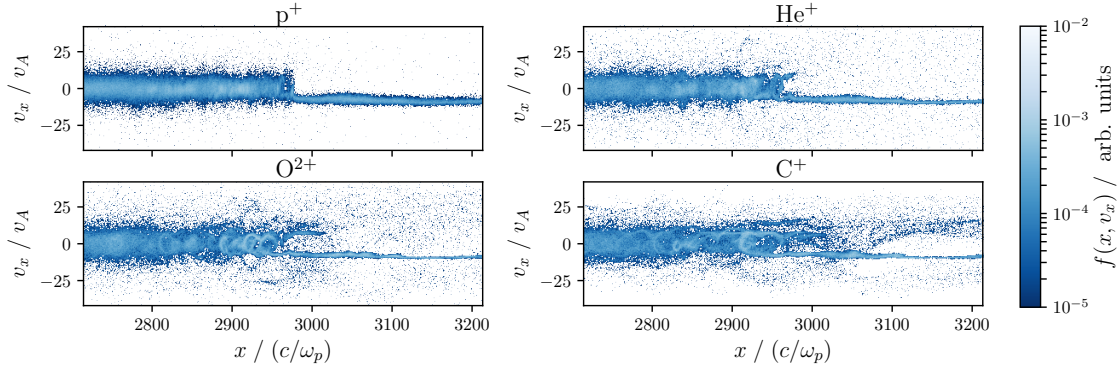
FIGURE 16: Phase space $f(x, v_x)$ at $t = 1000\,\omega_c^{-1}$ for different ion species in the region around the shock transition.

To analyze the downstream ion temperature in more detail, we show the velocity distribution, $f(v_x)$, for He^{2+} and C$^+$ ions in Fig. 17. The velocity distribution is computed for each species in a region of length $1000\,c/\omega_p$ behind the shock as well as in a region of the same size further downstream. The phase space plots, Fig. 16, indicate that while for protons a thermalization and relaxation to a Maxwellian distribution occurs almost directly behind the shock front, for ions with larger mass-to-charge ratios a thermalization takes place further downstream. This is confirmed by the velocity distributions in Fig. 17, where $f(v_x)$ measured far downstream and behind the shock are very similar for He^{2+}, but differ for C$^+$, especially at small v_x. The downstream temperatures are obtained for each ion species by fitting a Maxwellian distribution (dotted line in the left and mid frame of Fig. 17) to $f(v_x)$ far downstream. The results are plotted in the right panel of Fig. 17. The linear temperature dependence on the mass and its independence on the ion charge[16] perfectly match the predictions by the Rankine-Hugoniot jump conditions. However, the measured temperatures are lower than the values expected from Eq. (13), see the dashed line in the right panel of Fig. 17. This deviation, $T = 0.85\,T_2$, is caused by conversion of a fraction of the bulk kinetic energy in energy of the accelerated particle populations as well as energy of the magnetic field.
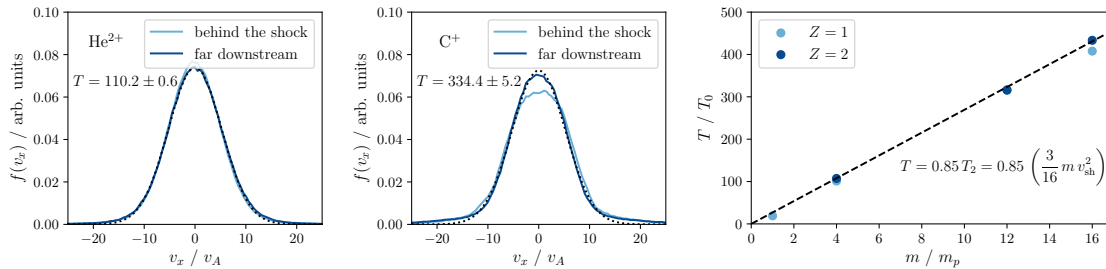

FIGURE 17: Velocity distribution, $f(v_x)$, for He^{2+} (left) and C$^+$ ions (middle) in a region behind the shock and far downstream. Maxwellian distributions are fitted to the far downstream data. (right) Downstream temperature as function of the ion mass. The temperature increases linearly with the mass of the respective ion species, however, it is lower than the prediction from the Rankine-Hugoniot conditions.

---

[16]   The ion charge determines the time needed for the thermalization.

The energetic particles are visible in the velocity distributions as nonthermal tails in addition to the thermal population: for the singly ionized carbon in Fig. 17 (middle frame) the measured $f(v_x)$ is larger than the prediction from the Maxwellian fit for $|v_x| > 15\, v_A$. For the investigation of these energetic particle populations we study the energy spectra of different ion species.

Energy Spectra

For the calculation of the energy spectra we employ a binning with logarithmically spaced bins and normalize the spectra to fulfill

$$\int_{E_{\min}}^{E_{\max}} f(E)\, dE = 1. \tag{88}$$

The energy spectra are obtained separately in the upstream and downstream regions, which are determined by the shock position, Eq. (87)[17]. Exemplary energy spectra of protons are depicted in Fig. 18. Note that the energy is measured in terms of the kinetic energy of the upstream bulk motion of the protons, $E_{\mathrm{sh}} = \frac{1}{2}\, m_p\, v_0^2$. The downstream energy spectrum, visible in the right panel, consists of two main components. At lower energies a Maxwellian distribution,

$$f_{\mathrm{th}}(E) \sim \sqrt{E}\, \exp(-E/T), \tag{89}$$

dominates, where T denotes the downstream temperature (see blue dotted line in Fig. 18). At higher energies the distinct feature is a power-law tail with an exponential cutoff,

$$f_{\mathrm{pow}}(E) \sim E^{-\gamma}\, \exp(-E/E_{\mathrm{cut}}). \tag{90}$$

Here γ is the power-law index and E_{cut} denotes the cutoff energy. A power-law fit is drawn in Fig. 18 by the black dashed line. Note that in this case the Maxwellian part of the distribution is not necessarily normalized to one as also the non-Maxwellian tail contributes non-negligibly to the overall energy spectrum.

The exponent of the power-law tail should correspond to the exponent predicted by the DSA. In the case of strong shocks this is given by Eqs. (32) and (33) for the momentum distribution. For the power-law tail in the energy spectra one gets $\gamma = 2$ for relativistic particles and $\gamma = 1.5$ in the nonrelativistic case, which is also used in the fit in Fig. 18.

Additionally to the Maxwellian and the power-law tail suprathermal particles with energies $3\, E_{\mathrm{sh}} < E < 10\, E_{\mathrm{sh}}$ are present in the downstream. These particles are energized above the thermal population but have not ended up in the power-law tail and obscure the transition from the thermal distribution to the power law [62].

Figure 19 shows the time evolution of the downstream energy spectra of different ion species. The spectrum is scaled with the energy in order to emphasize the power-law tail. The spectra of ions with larger A are shifted towards higher energies due to the higher mass. For all species the extension of the power law, i.e., the maximum energy increases

---

[17]   Additionally, a small region around the shock transition is excluded.
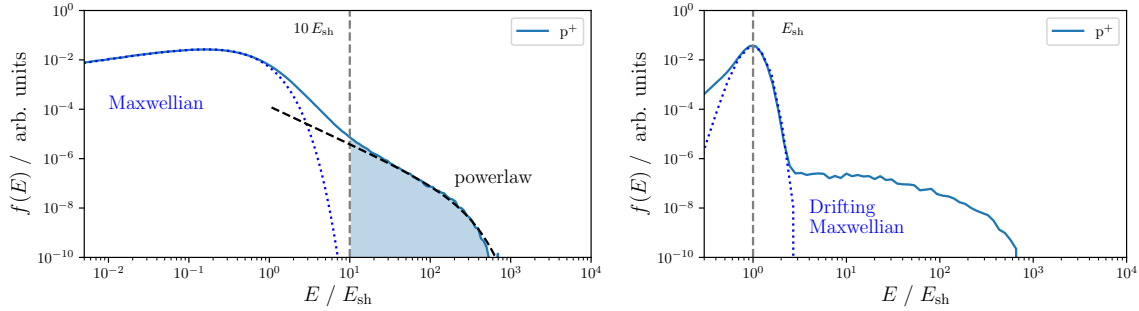
FIGURE 18: Proton energy spectrum downstream and upstream the shock transition for a simulation of a shock with $v_0 = 10\,v_A$. The spectra were obtained at $t = 1500\,\omega_c^{-1}$ and the energy is measured in terms of $E_{\mathrm{sh}} = 1/2\,m_p\,v_0^2$.

with time. For $t > 1500\,\omega_c^{-1}$ the tail is well developed for all ion species present in the simulation. However, for the ions with the largest A/Z, i.e., C^+ and O^+ the tail deviates from a smooth power law as it demonstrates some bumps. It is also worth noting that for these species the power-law tail starts to develop at later times. Hence, longer runtimes are necessary in order to achieve a smooth power-law tail for the heavier ions. The comparison of the energy spectra of ions with different charge states confirms the findings reported earlier [156] that the doubly charged ions reach higher energies.

To see exactly how the maximum energy, $E_{\max}$, behaves as function of time for different ion species, we have computed this quantity from the energy spectra using the condition $f(E) > 10^{-9}$. The resulting values are plotted in Fig. 20 for protons, He^+, C^+, and C^{2+}. The errorbars denote the width of the energy bin. We observe the maximum energy increasing roughly linearly with time for all ion species (see dashed lines which represent linear fits to the data). When comparing the energy plots (Fig. 20) for different ions it becomes apparent that for higher A/Z an efficient energy gain starts later in the simulation, which is particularly pronounced in the case of C^+ and C^{2+}. This can be attributed to the wave generation by the main plasma component, as waves with suitable wavelengths have to be present for efficient scattering and acceleration. Furthermore, one can see that ions with higher charge states are accelerated to higher energies, i.e., the doubly charged carbon is reaching approximately twice the maximum energy of C^+.

The phase space distributions in Fig. 16 already indicate an isotropic distribution of the velocities of the thermal ions in the downstream. However, for a sound statement different phase space planes have to be analyzed. A more appealing way of investigating the direction of particle motion is the analysis of the angular distribution of the velocities. We have calculated $f(\vartheta)$, where ϑ denotes the angle between the velocity components parallel and perpendicular to the background magnetic field,

$$\vartheta = \arctan\left(\frac{v_\perp}{v_\parallel}\right). \tag{91}$$

For the case of a parallel shock considered here one has $v_\parallel = v_x$ and $v_\perp = \sqrt{v_y^2 + v_z^2}$. To observe a difference in the angular distributions of different particle populations, we plot
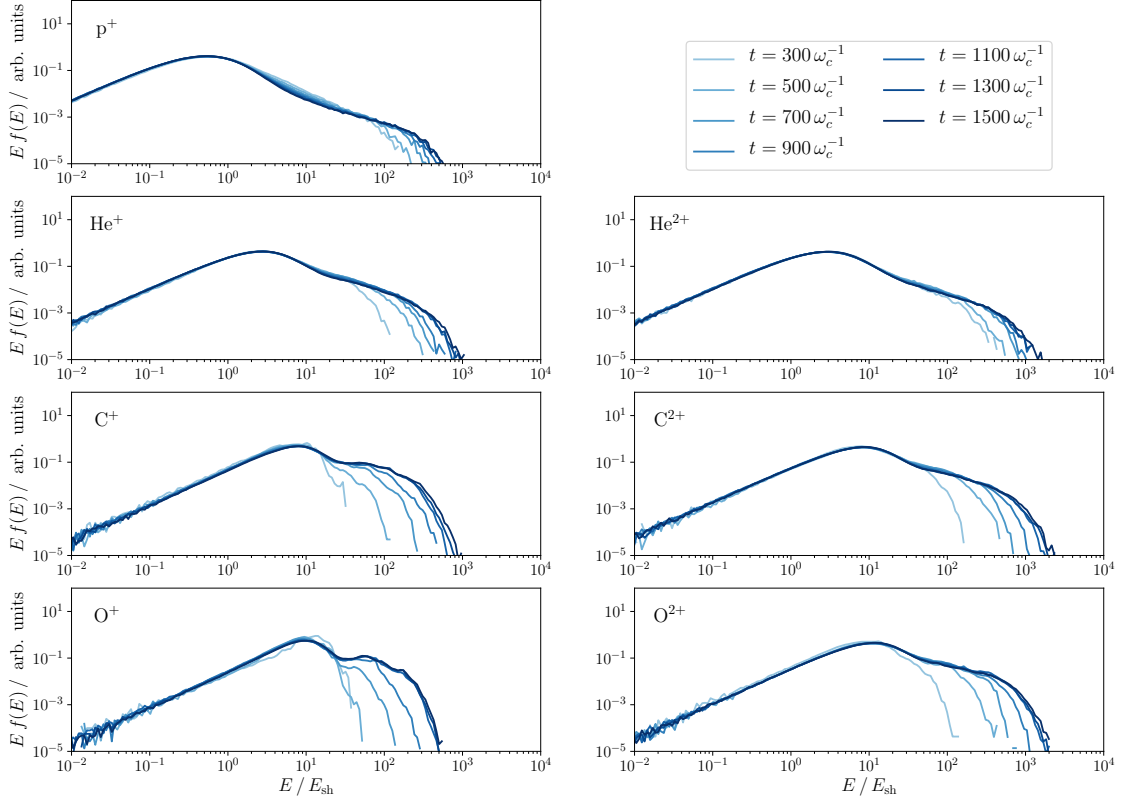
Figure 19: Time evolution of the downstream energy spectra of different ion species for a simulation with $v_0 = 10\,v_A$. The maximum energy increases with time and by the end of the simulation well developed power-law tails are visible.

the distribution of the velocity direction, $f(\vartheta)$, of protons in various energy ranges and at different positions in the simulation box in Fig. 21. We investigate three energy regimes: thermal particles with $E < 3\,E_{\text{sh}}$, suprathermal particles with $3\,E_{\text{sh}} < E < 10\,E_{\text{sh}}$, and accelerated particles with $E > 20\,E_{\text{sh}}$. In the downstream we find an isotropic distribution of velocity directions in all energy ranges. This can be seen from the $f(\vartheta) \propto \sin(\vartheta)$ behavior, which is expected for an isotropic angular distribution. In a region of $100\,c/\omega_p$ behind the shock the thermal particles are not yet fully isotropized, and the distribution of the more energetic particles is quite noisy due to the lower particle statistics. In a region with a size of 100 proton skin depth in front of the shock the angular velocity distribution in the low and higher energy ranges differ considerably. The low energy component consists of the protons moving with the upstream bulk velocity towards the shock. Hence, the angular distribution is shifted towards large ϑ, close to $\vartheta = \pi/2$. The suprathermal and energetic particles produce a different picture. Here the angular distribution points towards large perpendicular velocity components, with most of the energetic particles moving towards the upstream. In the whole upstream the situation is similar. The low energy upstream plasma has an angular distribution centered around large ϑ, while the more energetic particles have angular velocity distributions with maxima close to $\vartheta = \pi/2$. In contrast to the region in front of the shock, however, a larger fraction of particles has velocities directed towards the shock front, i.e., $\vartheta > \pi/2$, especially for the suprathermal protons.
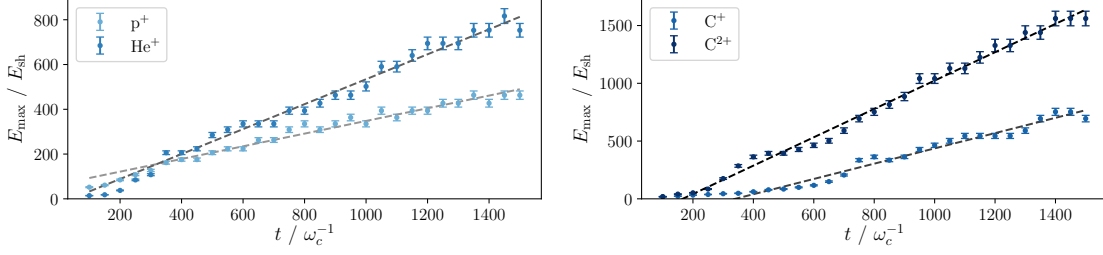
FIGURE 20: Maximum kinetic energy as function of time for different ion species. The maximum energy increases linearly with time.

These returning particles might be injected into the DSA process to further gain energy.

In the following we take a closer look at the mechanism, which might be responsible for the initial ion acceleration, which leads to an energization that allows for an injection into the DSA process. This mechanism should be able to explain the observed phase space plots, the energy spectra, as well as the angular distribution of the velocities observed in the simulation.
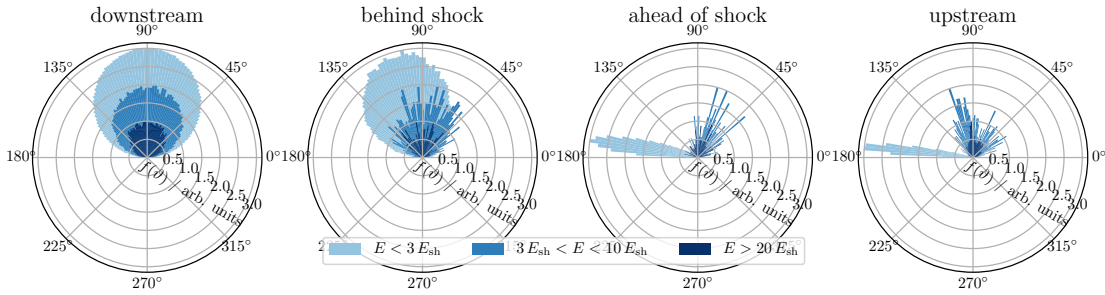

FIGURE 21: Angular distribution, $f(\vartheta)$, of proton velocities in different regions and energy ranges. In the downstream an isotropic distribution is visible for all energy ranges. The velocity distribution in the upstream is anisotropic but with a different behavior for thermal and energetic particles.

ACCELERATION MECHANISM

In order to understand the acceleration mechanism and the initial phase of the injection it is helpful to follow the trajectories of some particles that end up in the tail of the energy distribution. This is achieved by first performing a simulation, then selecting the energetic particles for tracing, and finally re-running the simulation and saving the positions, velocities and fields for the particles that have been selected.

Figure 22 shows exemplary trajectories of three particles, a proton, a He$^+$, and a C^{2+} ion, which are energized during the simulation. In the first panel the ion trajectory (blue line) in the magnetic field is plotted in the (x, t)-plane. The shock position is indicated by the black line and red crosses indicate shock crossings. All trajectories display the ions originating from the upstream and interacting with the shock front several times. After an interaction with the shock a particle might remain in the downstream or upstream medium for some time before returning back to the shock. For all three trajectories shown here

the particle finally ends up in the upstream medium. The time evolution of the particles' longitudinal velocity, v_x, and energy are shown in the mid panels. The velocity plots display that the ions change their direction several times. While the particle is propagating in the upstream and approaching the shock its kinetic energy does not change. An increase in the kinetic energy is visible mostly at times when the ion encounters the shock several times (indicated by the horizontal dotted lines). Finally, in the right panels of Fig. 22 we show the components of the velocity parallel, $v_\parallel$, and perpendicular, $v_\perp$, to the shock normal over time. Both velocity components increase during the propagation. In the $(v_\parallel, v_\perp)$-plane the ions move along arches of circles (with two distinct centers) of constant velocity $v = \sqrt{v_\parallel^2 + v_\perp^2}$. This process is reminiscent of the "scatter free acceleration" proposed by Sugiyama *et al.* in [157, 158, 159], where the authors model the injection and acceleration of particles at a shock in the presence of a large amplitude monochromatic Alfvén wave by means of test-particle calculations as well as by one-dimensional hybrid simulations. Figure 23 displays schematically the proposed scenario. In the upstream rest frame the monochromatic wave travels towards the upstream with the Alfvén velocity, while in the shock frame it moves towards the shock with a velocity v_w^{up} corresponding to $M - 1$ since the field is frozen into the plasma. As the wave passes the shock transition, it is compressed in the downstream, leading to an increase of the wave amplitude and a decrease of the wavelength. In the downstream rest frame the wave propagation is directed upstream with the local Alfvén velocity, v_w^{down}. For a particle propagating in such a wave, the energy is conserved in the frame of the wave. Hence, a particle in the upstream will move in the $(v_\parallel, v_\perp)$-plane on a circle centered around $(v_w^{\mathrm{up}}, 0)$. When the ion crosses the shock its motion will be constrained to another circle centered around $(v_w^{\mathrm{down}}, 0)$ as the energy is conserved in the local wave frame. As the ion propagates in the downstream and interacts with the waves, its parallel velocity, $v_\parallel$, changes allowing the particle to return to the upstream. During such cycle the energy of the ion increases, as seen from the shock frame, with the velocity gain being mostly in the $v_\perp$-component. The authors of [157, 158, 159] claim that the quick motions along the circles are due to nonlinear phase trapping. The important parameter in this model, which determines whether an ion is injected, is the phase angle, θ, between the velocity perpendicular to the shock normal and the direction of the wave magnetic field. Other processes, such as shock drift acceleration (SDA) were found to contribute only little as the distance traveled by the ion along the motional electric field is very short. Repeated acceleration by multiple interactions with the shock are deemed to be possible, if the wave polarization is not circular, but rather elliptical or linear, for example, due to presence of additional left-handed polarized waves of the same wavelength. In this setup stochastic pitch angle scattering can occur allowing some of the escaping ions to return to the shock to get further accelerated by the mechanism outlined above.

In the following, we have made sure that this mechanism is not only an artifact of the reduced one-dimensional modeling and followed the trajectories of accelerated protons also in a two-dimensional (2D) simulation. We have initialized the simulation domain with a size of $4000 \times 100 \, (c/\omega_p)^2$ and injected a plasma with a bulk velocity of $v_0 = 5 \, v_A$. To
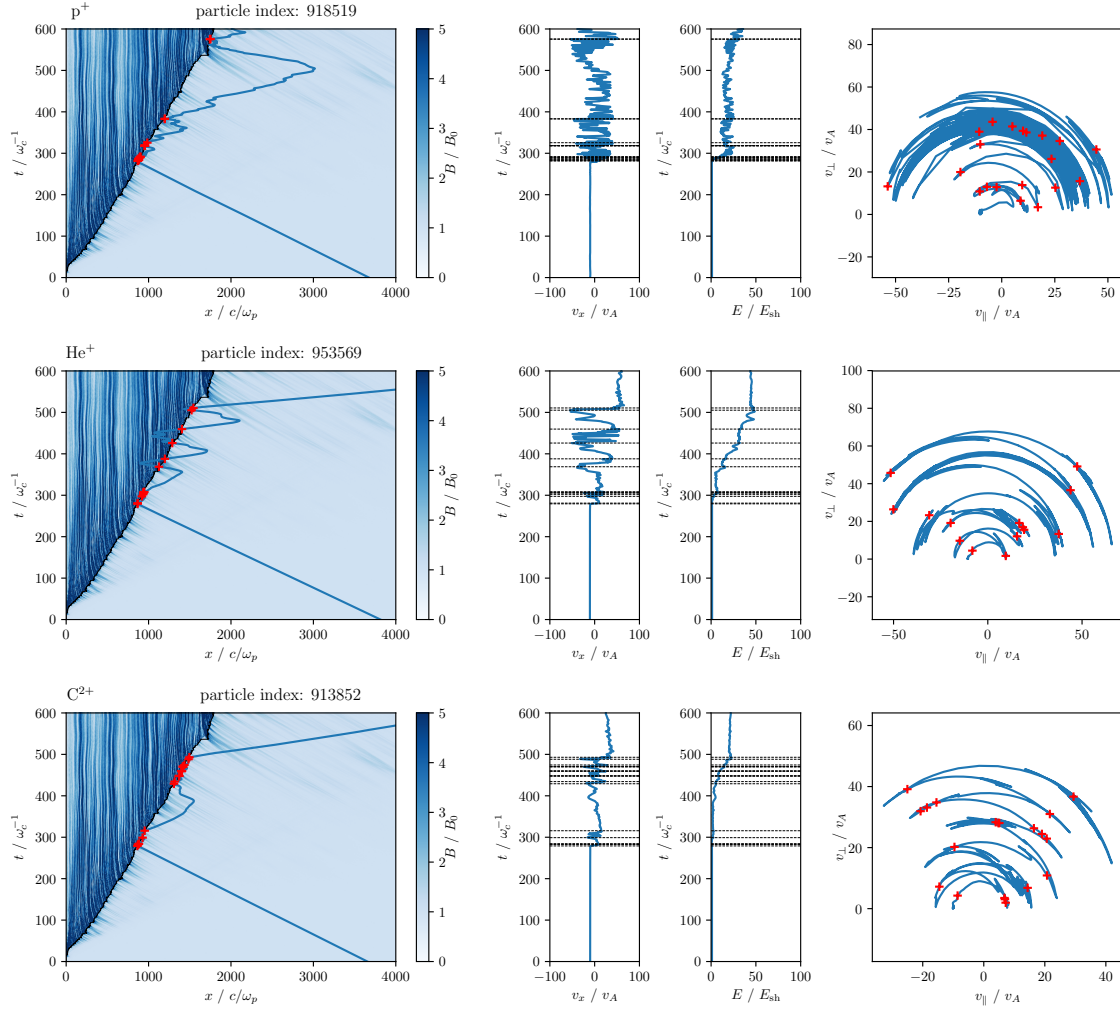
FIGURE 22: Trajectories of different ion species in the magnetic field. The ions are initially reflected from the shock and cross the shock many times while being scattered by the waves in the up- and downstream. Additionally v_x and the ion's kinetic energy are plotted as function of time as well as the particle motion in the $(v_\parallel, v_\perp)$-plane.

reduce the computational costs, we considered a pure hydrogen plasma. The background magnetic field is set at an angle of $\theta_{\mathrm{Bn}} = 20°$ with respect to the x-axis. We identified the particles that have been accelerated by $t = 300\omega_c^{-1}$ and followed their trajectories. The results are shown in Fig. 24. In the left panel the trajectory of an accelerated proton is plotted in the shock rest frame, where the shock is positioned at $x = 0\,c/\omega_p$ (black dashed line). Note that in the two-dimensional case the shock position on the x-axis is obtained by averaging over the transverse y-direction and a constant shock velocity is assumed. The resulting uncertainty is shown in Fig. 24 by the grey shaded area of $10\,c/\omega_p$ width. Furthermore, the motion of the proton is unfolded in the y-direction for the sake of clarity. When the particle crosses one of the periodic boundaries, $y = 0$ or $y = L_y$, it reenters the simulation domain on the other side, $y = L_y$ or $y = 0$. The positions, where this occurs are marked in Fig. 24 by black points. The time is color coded as indicated by the colorbar. In the middle panel the proton's kinetic energy is plotted as function of time. The times, at which the particle is close to the shock and gains energy are indicated by the
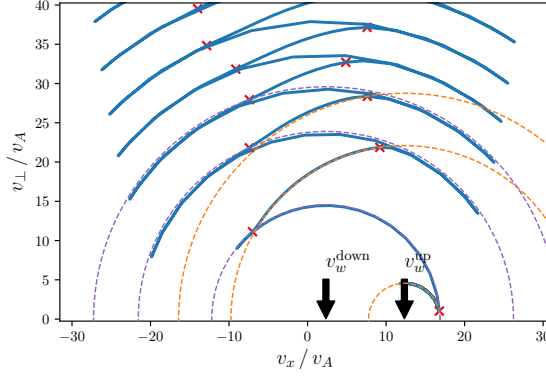
FIGURE 23: Particle motion in the $(v_\parallel, v_\perp)$-plane for an ion in a monochromatic wave at a collisionless shock. As the energy is conserved in the wave frame the motion will take place along circles centered around the wave velocity.

grey shaded areas. Finally, in the right panel the particle's motion in the $(v_\parallel, v_\perp)$-plane is shown. The time the particle is close to the shock is shown grey. The similarity of the particle behavior in one- and two-dimensional simulations allows us to conclude that the same initial energization mechanism is at work in both setups.
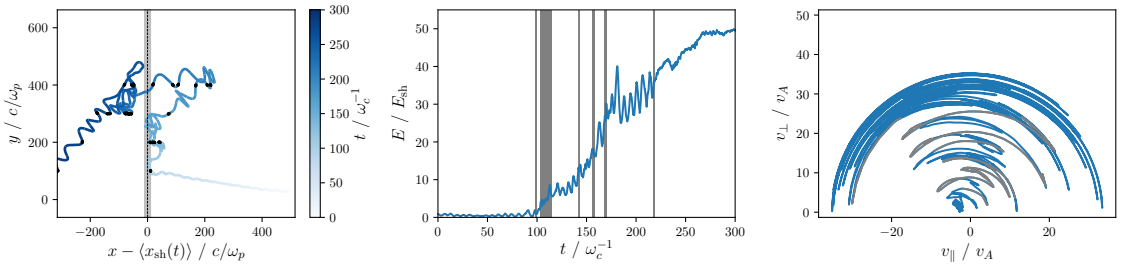

FIGURE 24: Trajectory of an accelerated proton from a two-dimensional simulation. The left panel shows the trajectory in the rest-frame of the shock with the shock positioned at $x = 0\,c/\omega_p$. In the middle the proton kinetic energy is plotted as function of time. On the right the particle motion is shown in the $(v_\parallel, v_\perp)$-plane.

A different injection model which includes shock reformation and ion reflection in the downstream frame was proposed in [97]. In this model ions can either simply pass the shock when the shock potential is low or be reflected when the potential is high. The reflected ions are then energized via SDA with a fraction of them passing the shock after only one SDA cycle. These ions make up the suprathermal part of the spectrum. A small fraction of ions will undergo multiple reflections and gain more energy. These ions finally escape towards the upstream and are considered as injected. While the authors have found good agreement of this model with proton energy spectra from hybrid simulations it fails to describe the injection of ions with larger A/Z, for which the penetration of the shock potential is easier. Furthermore, the usage of a polytropic equation of state, which is based on the assumption of electron-proton temperature equilibration[18], might lead to an overestimation of the influence of the shock potential.

---

[18] Due to the collisionless nature of the plasma it is not clear whether a full temperature equilibration is possible during the shock lifetime, see Ch. 6.

In this thesis we do not aim to develop a complete model for particle injection into the DSA as our results support the mechanism presented by Sugiyama *et al.* [157, 158, 159]. Instead we want now to quantify how the injection of different ion species depends on the mass-to-charge ratio.

Injection Efficiency and Number Efficiency

The direct measurement of the injection rate in the simulation is difficult because the transition from the thermal part to the power-law tail is hidden by the presence of suprathermal particles, see left frame in Fig. 18. A simple measure of the injection efficiency is the number of energetic particles in the tail of the energy spectrum[19]. For protons it has been established by many simulations that a power-law tail is well developed at energies above ten times the upstream bulk kinetic energy ($E > 10\,E_{\rm sh}$). Since for ions with higher masses the energy spectra are shifted towards higher energies we calculate the selection rate as the fraction of ions in the tail with energies of $E > 10\,A\,E_{\rm sh}$ for each ion species. We obtain the selection rate for different ion species at several times throughout the simulation up to $t = 2000\,\omega_c^{-1}$. The results are plotted as function of the mass-to-charge ratio in Fig. 25 for simulations of shocks with different Mach numbers. We find that for the lowest shock velocity the fraction of ions that end up in the energetic tail is lower, especially for ions with $A/Z \geq 4$. For $M_A \geq 8$ we observe an almost linear increase of the selection rate with the mass-to-charge ratio at lower A/Z. This is in agreement with results reported earlier [156], where a linear increase of the selection rate for $A/Z \leq 8$ has been found (see Fig. 2 in [156]). Our results indicate that depending on the Mach number of the shock a saturation of the selection rate occurs around $A/Z \sim 8 - 12$. For even higher values of A/Z we find a decrease of the selection rate. This is in agreement with the physically correct asymptotic behavior for $A/Z \to \infty$, as neutral particles should simply pass the shock without being injected. The follow up 2D simulations [160] also point toward a saturation of the selection rate for higher A/Z.

The exact value of the mass-to-charge ratio at which the saturation occurs is to some extend time-dependent, as heavier ions are accelerated at later times, see Fig. 20. This is because for the injection and acceleration of ions with higher A/Z longer waves need to be generated to provide efficient scattering. These waves are predominantly excited if the ions of the main plasma component (protons) are already accelerated to higher energies. The saturation and subsequent decrease of the selection rate for high A/Z ratios is in tension with the findings reported in a recent study on the chemical composition of CRs [156] where in two-dimensional hybrid simulations the injection rate was found to increase linearly with A/Z without saturation up to at least $A/Z = 56$ (singly ionized iron). This discrepancy has triggered some discussions, but it might be ascribed to particularities of the two approaches. This includes the use of a realistic plasma composition with a $\sim 10\%$ contribution of helium ions (as opposed to 10^{-5} used in [156]), determination of the selection rate from the well developed DSA spectra downstream for all ion species (as opposed to the evaluation of the chemical enhancement of heavier elements with $A/Z > 8$

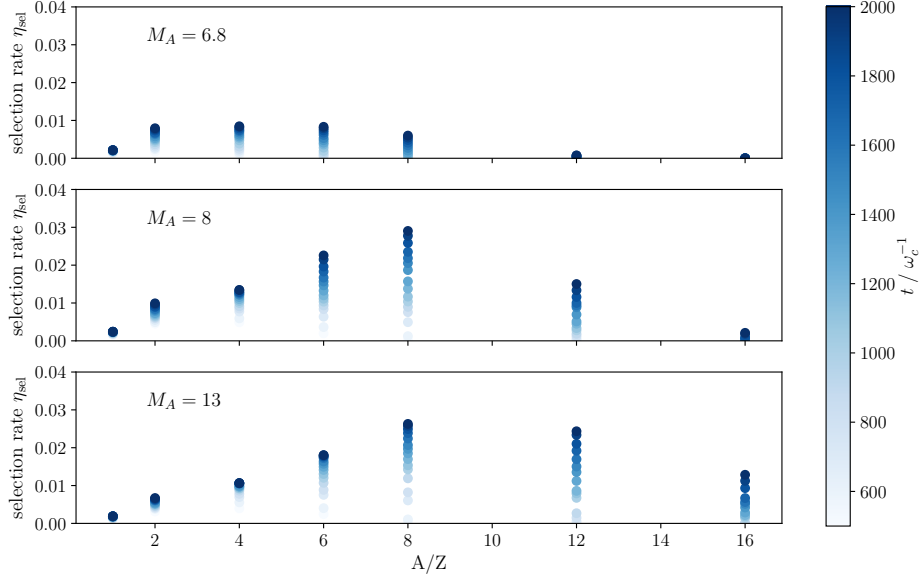[19]   This quantity has also been used previously, see, e.g., [27].

Figure 25: The fraction of accelerated particles in the tail of the energy spectrum as function of A/Z for different shock Mach numbers. The color of the symbols denotes the time, indicating that heavier elements are injected later in the simulation.

in the upstream before these species have developed the universal downstream DSA spectra in [156]) etc. Without going into details, we stand by the statement that the unlimited increase of the selection rate with A/Z is unphysical or at minimum, imposes quite unusual constraints on the scattering turbulence.

Independently of the discussion above, our results clearly indicate that the injection rate into the DSA, obtained from self-consistent hybrid simulations without any further assumptions, depends on the mass-to-charge ratio of the respective ion species and on the shock velocity. This dependence is an intrinsic property of the acceleration mechanism. In the following we will show that the elemental dependence of the injection efficiency is sufficient to ensure the rigidity dependence of the $p/$He flux ratio in agreement with the recent AMS-02 and PAMELA observations.

Combining the Injection with Shock Evolution

While the results presented in Fig. 25 already show that the injection depends on A/Z and on the Mach number, as was predicted by the analytic theory in [102, see, e.g., Fig. 5], this is not yet sufficient for explaining the measured $p/$He ratio, Fig. 13. As was stated above in Section 4.2, we assume that the elemental anomaly in the rigidity spectra of different elements obtained by the new generation of precise direct measurements can be attributed to the time dependence of the shock strength combined with the intrinsic properties of the injection phase of the acceleration mechanism. Hence, the idea is to combine the injection efficiency from the numerical simulations with the evolution of the SNR during the Sedov-Taylor stage. This phase covers the evolution of a SNR after the free expansion phase, when the mass of interstellar gas swept up by the shock becomes larger than the ejected mass [41], and it can be described by a self similar solution. During this stage the

shock radius, R_{sh}, increases with time while the shock velocity, V_{sh}, and also the shock Mach number decreases as

$$R_{\text{sh}}(t) \simeq C_{\text{ST}}\, t^{2/5}, \tag{92}$$

$$V_{\text{sh}}(t) \simeq \frac{2}{5}\, C_{\text{ST}}\, t^{-3/5} = \frac{2}{5}\, C_{\text{ST}}^{5/2}\, [R_{\text{sh}}(t)]^{-3/2}. \tag{93}$$

Here the constant, $C_{\text{ST}} \simeq (2\, E_e/\rho_0)^{1/5}$, is determined by the energy of the ejecta, E_e, and the ambient density, ρ_0.

The transition from the Maxwellian to the power-law tail in the energy spectrum is not sharp, see left frame in Fig. 18, therefore we fit a thermal distribution, Eq. (89), and a power law, Eq. (90), to the downstream energy spectra and calculate the injection efficiency as

$$\eta_{\text{inj}} \propto \left(\frac{dN}{dE}\right)\Bigg|_{E=E_{\text{inj}}} = \frac{f_{\text{th}}(E_{\text{inj}})}{\int_0^\infty f_{\text{th}}(E)\, dE}, \tag{94}$$

where the injection energy, E_{inj}, is defined via $f_{\text{th}}(E_{\text{inj}}) = f_{\text{pow}}(E_{\text{inj}})$ and computed separately for each species.

To obtain the injection efficiency as function of the shock strength, we have performed a series of simulations for various initial upstream bulk velocities with a plasma consisting of 90% protons and 10% fully ionized helium. After the spectra for both species have been converged, we have calculated the injection efficiency according to Eq. (94). This allows us to obtain the injection efficiency as function of the shock Mach number, $M = (v_0 + v_{\text{sh}})/v_A$, where v_{sh} is the shock velocity measured in the downstream rest frame.

The resulting Mach number dependence of the injection efficiency is plotted for protons and He^{2+} in Fig. 26. The errorbars denote the spread in dN_{inj}/dE calculated at several times. The general behavior of the injection efficiency as function of M is similar for protons and He^{2+}. It reaches a maximum ($M \simeq 5$) for protons and ($M \simeq 7$) for helium ions, and then decreases towards higher Mach numbers. This was predicted theoretically in [102], where an asymptotic behavior of $\eta_{\text{inj}} \sim \ln M/M$ was found. It can be seen that at low Mach numbers the injection of protons is dominant and, furthermore, for He^{2+} the maximum is shifted towards larger M, compared to the protons.

	p	He^{2+}
a	5.68	0.25
b	3.27	3.79
c	3.50	2.73

TABLE 1: Parameters for the fit to the injection efficiency, see Fig. 26, where a function $\eta(M) = a\,(M-b)\,M^{-c}$ was assumed. Separate fits are performed for protons and helium ions.

In order to model the time-dependence of the acceleration we combine the observed M-dependence of the injection with the shock evolution during the Sedov-Taylor phase, Eqs. (92) and (93). During the evolution of the SNR the shock slows down, which has an influence on the injection efficiency as well as the spectral slope for which the theoretical DSA prediction, Eq. (33), is assumed. This convolution of the injection efficiency obtained
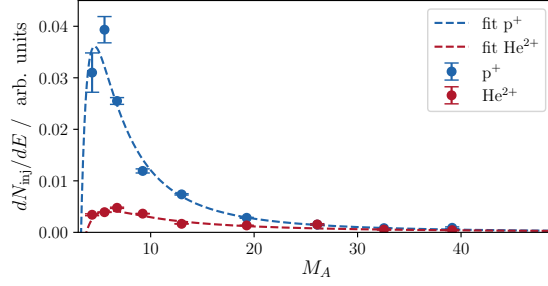
FIGURE 26: Injection efficiency for protons and fully ionized helium as function of the shock Mach number. A function $\eta(M) = a\,(M - b)\,M^{-c}$ is fitted to the simulation results.

from the simulation with the SNR evolution allows us to extend the spectra to rigidities far beyond what any simulation can achieve[20].

Following [143], we calculate the number of CRs of each species $\sigma = p^+, \mathrm{He}^{2+}$ deposited in the interior of the remnant as the shock radius increases from R_{min} to R_{max} as

$$N_\sigma(\mathcal{R}) \propto \int_{R_{\mathrm{min}}}^{R_{\mathrm{max}}} f_\sigma\left(\mathcal{R}, M(R)\right) R^2 \, \mathrm{d}R \propto \int_{M_{\mathrm{max}}^{-2}}^{M_{\mathrm{min}}^{-2}} f_\sigma(\mathcal{R}, M) \, \mathrm{d}M^{-2}. \tag{95}$$

Here $f_\sigma(\mathcal{R}, M)$ denotes the distribution function for species σ in terms of the rigidity. While the shock radius increases, the shock Mach number drops from M_{max} to M_{min}. Eqs. (92),(93) allow to eliminate the radius from the equation. For the momentum or rigidity distribution function we assume the power law predicted by the DSA and scale it with the injection rate from the simulation, which is a function of Mach number and mass-to-charge ratio,

$$f_\sigma(\mathcal{R}, M) \propto \eta_{\mathrm{inj}}^\sigma(M)\left(\mathcal{R}/\mathcal{R}_{\mathrm{inj}}\right)^{-q(M)}. \tag{96}$$

The equations above are accurate for the sub-TV particles that are accelerated quickly in the SNR shocks. We focus on this rigidity range since these particles can be detected dicrectly by magnetic spectrometers such as AMS-02 and PAMELA. While Eq. (95) implicitly assumes an unimpeded release of the accelerated particles into the galaxy, the key of our approach is to consider only the ratios of different elements, which are independent of the release mechanism. In this way we mitigate the complicated problem of modeling the escape of the CRs into the ISM, which is now actively researched, see, e.g., [161, 162, 163]. Since we have performed simulations only for a limited number of shock velocities (sufficiently detailed Mach scans, though), we fit a simple function of the form $\eta(M) = a\,(M - b)\,M^{-c}$ to the simulation results to get a continuous function for the injection efficiency. The fits are depicted in Fig. 26 as dashed lines and the fit parameters are given in Tab. 1.

We calculate the proton-to-helium ratio, N_p/N_{He}, as function of particle rigidity according to Eq. (95) via an integration in the range $M_{\mathrm{min}} = 3.5 < M < M_{\mathrm{max}} = 100$. The

---

[20] This extension is justified as long the energy spectra from the simulation exhibit the power-law tail predicted by the DSA.
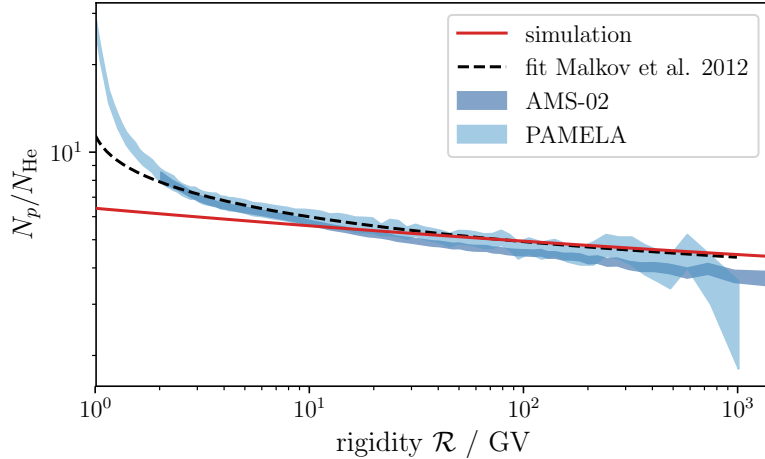
FIGURE 27: Rigidity dependence of the proton-to-helium ratio extracted from the simulation compared to the measurements from AMS-02 [7] and PAMELA [5].

result is plotted in Fig. 27 as red line together with the measurements from the PAMELA and AMS-02 instruments (blue areas). The proton-to-helium ratio extracted from our simulations correctly reproduces the decrease of the ratio with rigidity. For $\mathcal{R} > 10$ GV we find a good agreement with the observational data, where the proton-to-helium ratio can be described by a power law with $\Delta q \approx 0.1$. Differences between the predictions from the simulations and the measurements are visible in the lower rigidity range. This has to be expected because the equations of motion, Eqs. (84), (85) for the two particle species differ in this regime due to the different values for $\mathcal{R}_0$. The exact reason for the small deviation (it is, however, smaller than the spectral difference Δq) from the observational data in the high-rigidity range is unclear. It can be caused, for example, by spallation during the propagation in the ISM, or be a mixing effect from different SNRs. However, except for this uncertainty, we can conclude that the mass-to-charge dependence of the injection can fully explain the measured p/He ratio.

DIMENSIONALITY OF THE SIMULATIONS

One important point to discuss is the reduced dimensionality in the simulations. Certainly, most fundamental aspects of shocks can be considered in the direction along the shock normal, as it is done in our simulations. However, there are phenomena that are only accounted for if a two- or even three-dimensional (3D) description of the system is used. These include effects such as shock corrugation or rippling [146, 164], which call for at least two-dimensional modeling and might influence the injection. While a full 3D hybrid simulation would best resemble reality, it is computationally not feasible to follow the shock in such simulation over long time with an acceptable box size (also in the transverse directions) and good particle statistics. Hence, a 2D model seems to be a reasonable compromise as additional effects, not present in 1D modeling are included while the simulations are computationally possible. With this it is implicitly assumed that 2D simulations of the particle acceleration at collisionless shocks produce more credible

results than 1D simulations do. As this might not always be the case, caution is advised (see also the discussion in [29]).

Mainly two aspects have to be considered in this context. First, when considering turbulence in a 2D fluid an inverse cascade appears, which is not present in three dimensions [165]. Although the difference between 2D and 3D dynamics is not so explicit in magnetohydrodynamic (MHD), the inverse cascade in 2D might lead to the formation of coherent structures and therefore to an excessive scattering. Second, to reduce the computational effort 2D simulations are usually performed using a simulation box with a relatively small size in the transverse direction where the periodic boundaries are placed. This strongly elongated box setup can cause artificial periodicities on the scale of the box size which can be "seen" by energetic ions with large Larmor radii.

We have performed a series of 2D simulations with various transverse box lengths, L_y, ranging from $L_y = 50 \, c/\omega_p$ to $L_y = 800 \, c/\omega_p$. The length of the simulation box in the shock propagation direction was fixed to $L_x = 19200 \, c/\omega_p$ in all cases and the simulations were performed for an upstream bulk velocity of $v_0 = 10 \, v_A$. As for the 1D simulations the magnetic field was set parallel to the shock propagation direction, but also simulations for $\theta_{\mathrm{Bn}} = 40°$ were performed.

In Fig. 28 the spatial distribution of the z-component of the magnetic field is depicted for the smallest and biggest transverse box sizes that were investigated. The differences in the field configuration are clearly visible. The Fourier spectrum of B_z is shown in the right panel. Due to the small transverse size in the first case the number of possible wave vectors in y-direction is very limited and a variation of B_z appears mostly in x-direction. Hence, for 2D simulations a reasonable transverse size of the simulation box is important, as this size limits the maximum wavelength in this direction. Furthermore, some instabilities can be suppressed, if the size of the simulation in the transverse direction is small, as was also noted in [166]. Figure 29 shows the downstream particle energy spectra for these
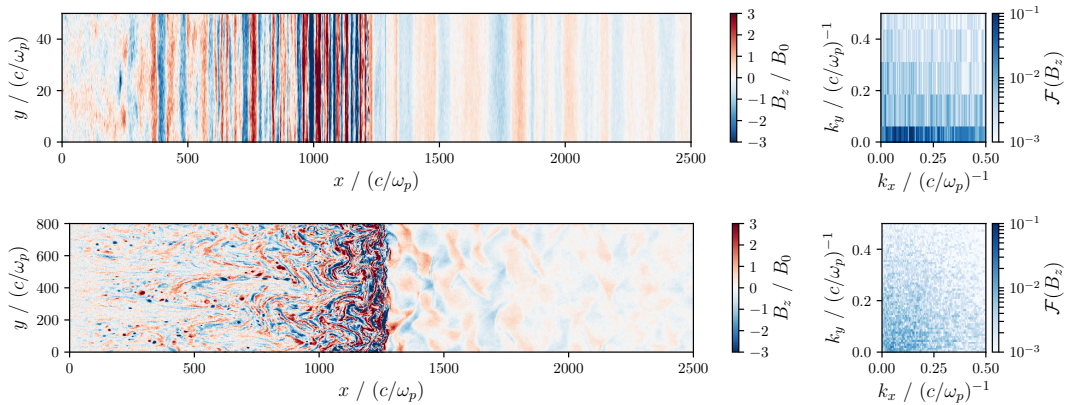

FIGURE 28: $B_z(x, y)$ around the shock transition for two simulations with different transverse lengths of the simulation box. The fields are taken at $t = 400 \, \omega_c^{-1}$ for simulations initialized with $v_0 = 10 \, v_A$. Additionally, the Fourier transform of the field component is shown on the right. Due to the limited transverse size in the first case, the number of possible wave vectors in y-direction is very limited and a variation of B_z appears mostly in x-direction.
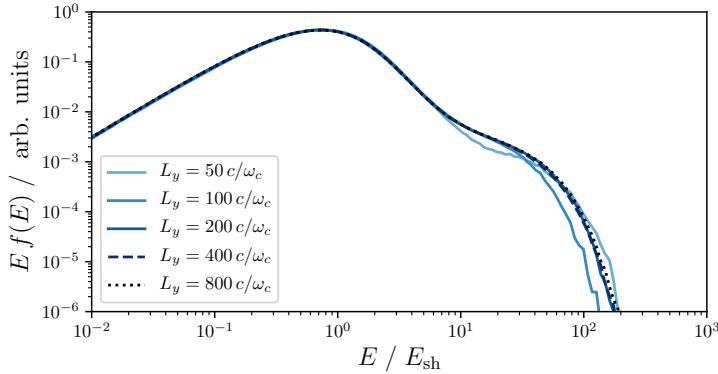
Figure 29: Downstream energy spectra obtained from two-dimensional simulations with different transverse box sizes. When using very elongated boxes the spectra differ clearly, indicating an influence of L_y on the energization of the protons.

simulations. It can be seen that for the smallest transverse box sizes the spectra exhibit considerable differences in shape and maximum achievable energy. For $L_y \geq 200\,c/\omega_p$ the energy spectra are very similar, indicating a convergence. However, for longer simulation times, larger box sizes might be necessary as as the maximum energy is increasing[21].

4.5 Summary

We have performed self-consistent hybrid simulations focused on the injection phase of of the DSA, where elemental similarity does not apply. In these simulations ions with mass-to-charge ratios $A/Z < 16$ are included self-consistently with weights reflecting the composition of the ISM. The self-consistent treatment is proven to be very important for helium ions, which contribute with approximately ten percent to the ISM composition and drive waves that enrich the spectrum with additional components. We observe the development of power-law tails in the energy spectra in agreement with the theory of DSA and show that the maximum achievable energy increases with time. We find an injection process similar to the one proposed by Sugiyama *et al.* [158], which relies on the nonlinear interaction of the particles with circularly polarized Alfvén waves.

Our results prove the earlier theoretical predictions [102] and numerical findings [156] that the mass-to-charge ratio, A/Z, is an important parameter for the injection. We show that the fraction of energetic particles in the power-law tail depends on A/Z in a particular way. After a linear increase with A/Z this measure of the injection saturates in a Mach-dependent fashion at higher A/Z.

We have performed a sufficiently detailed scan over various shock Mach numbers and calculated the injection rate for protons and He^{2+} ions to test the theoretically predicted p/He injection bias [143]. By combining the simulation data with the time-dependence of the shock evolution during the Sedov-Taylor phase, we calculated the rigidity dependence of the p/He ratio. The resulting prediction of the proton-to-helium ratio (see Fig. 27) is in good agreement with the high-precision measurements by the PAMELA and AMS-02

---

21   At the time shown Fig. 28 the Lamor radii of the most energetic particles are already on the order of $100\,c/\omega_p$.

detectors [5, 7], showing a spectral index difference of $\Delta q \approx 0.1$ above $\mathcal{R} = 10$ GV.

This agreement of the predicted p/He ratio with the measurements shows that the mass-to-charge dependence of the injection phase, as discussed in the beginning of this chapter, fully explains the apparent anomaly in the rigidity spectra of different elements. Therefore, the rigidity dependence of the proton-to-helium ratio can be ascribed to the intrinsic properties of particle acceleration at collisionless shocks. In contrast to other explanations that were put forward, such as contributions from several different SNRs or the inhomogeneity of their environments, this explanation does not require any additional assumptions.

CHAPTER 5

The Steepening of Cosmic Ray Spectra

5.1 Motivation

In the previous chapter we have presented one example of the details in the cosmic ray (CR) spectra that are revealed by the precise CR measurements and discussed how these features allow to test hypotheses of CR origin. While in Chapter 4 the focus has been on an anomaly which was observed in the spectra of the flux ratios of certain ion species, in particular the p/He ratio (and also p/C and p/O), now we want to turn our attention to a characteristic that is common to all spectra of primary CR ions: the discrepancy between the steepness of the observed spectra measured on Earth or using space based instruments, and the prediction by the diffusive shock acceleration (DSA).

As stated before, the DSA predicts a power law for the momentum distribution of the accelerated particles, $f(p) \sim p^{-q}$, with a power-law index which only depends on the shock compression, see Eq. (33). Thus, an agreement of the measured spectra with the theory strongly supports the predicted scenario of CR origin while any disagreement will cast doubt that the DSA correctly describes the acceleration of cosmic rays.

A certain difference, mainly attributed to propagation losses, between the CR spectra measured on Earth and the theoretically predicted source spectra is expected. During the propagation from the source to an observer, the accelerated particles perform a diffusive motion in the turbulent interstellar magnetic field. As the diffusion coefficient is energy dependent and an escape of particles from the Milky Way is possible, the spectral index has to be increased by $\Delta q_{\mathrm{prop}} = 0.3 - 0.6$. The exact value depends on the turbulence in the interstellar medium (ISM) that influences the diffusion model (see, e.g., [167]). Although constraints on the diffusion properties can be obtained from measurements of secondary-to-primary ratios such as the boron-to-carbon ratio [168], not all uncertainties in the diffusion parameters can be removed [169]. While the offset $\Delta q_{\mathrm{prop}} = 0.3 - 0.6$ would allow to link the CR spectra observed on Earth, $f_{\mathrm{obs}}(E) \sim E^{-2.7} - E^{-2.8}$, to the DSA-predicted source spectra, $f_{\mathrm{source}}(E) \sim E^{-2.0} - E^{-2.2}$, this link is weakened as the AMS-02 measurements of the boron-to-carbon ratio favour a lower value for Δq_{prop} [168].

The correction for propagation losses can be omitted only for two types of observations. Firstly, the ratios of different elements in the CR composition (under the assumption that both elements can be attributed to the same accelerator and spallation is negligible), which was considered in the previous chapter. Secondly, the momentary source spectra, which can be determined only indirectly via secondary emission from the accelerated CRs in the supernova remnant (SNR) environment. Here the difficulty lies in the disentanglement of the leptonic and hardronic sources of the radiation.While emissions at X-ray energies can be attributed to synchrotron radiation of energetic electrons, γ-rays can be either produced via inverse Compton scattering of energetic electrons on the cosmic microwave

background or by the decay of neutral pions, which are produced by collisions of CRs with the ambient gas [170]. These indirect measurements of the source spectra [171] confirm the spectral steepening already indicated in the data published by the AMS-02 collaboration for the proton spectrum [7]. Additional validation comes from the recent high-precision observations by the CALET team, which reports a spectral index of $q = 2.87 \pm 0.06$ below 500 GV [30]. These results are in tension with the DSA, resulting in an ongoing debate whether the DSA can fully account for the production of CRs in SNRs (e.g., [172]).

A simple explanation of the steep spectra would be the addition of an exponential cutoff to the power law predicted by the DSA. However, this old paradigm is not supported by the newer measurements and has been ruled out even if one invokes a nearby source with a cutoff in the sub-TeV range to explain the steep part of the spectrum. Various other theories have been proposed to elucidate the steepening of the source spectra in order to reconcile the observations and the DSA-prediction. The authors of [173] attribute the steepening to the energy loss of CRs due to turbulent magnetic field amplification during the acceleration process. Another scenario was put forward in [174]. It is based on the fact that the injection into the DSA largely depends on the shock inclination, i.e., the angle between shock normal and background magnetic field, θ_{Bn}. Typically one distinguishes two domains: quasi-parallel shocks with $\theta_{Bn} \leq 45°$, where particle injection is effective, and quasi-perpendicular shocks with $\theta_{Bn} > 45°$, where particle injection is suppressed. This property of collisionless shocks can be derived analytically from simple kinematic considerations [101] and has also been reported in Monte-Carlo [145] and hybrid simulations [27]. For completeness, we show in Fig. 30 (left panel) the fraction of particles in the power-law tail as function of the shock inclination obtained from two-dimensional hybrid simulations using our code. In these simulations the plasma is initialized to flow with a velocity of $v_0 = 10\, v_A$ in the $-x$ direction and the background magnetic field makes an angle θ_{Bn} with the x-axis and lays in the simulation plane. The fraction of energetic particles[22], a measure for the injection efficiency, does not strongly depend on the angle between the shock normal and the background magnetic field, as long as the shock is quasi-parallel As the shock inclination increases above $\theta_{Bn} = 45°$ the injection efficiency drops fast, and above $\theta_{Bn} = 60°$ a formation of a power-law tail cannot be observed anymore. In the right panel of Fig. 30 the amplitude of the magnetic field and field lines are plotted for three different shock inclinations, showing that turbulent magnetic fields are only created if particles are accelerated to high energies.

In bilateral SNRs, such as SN 1006, two regions of active particle acceleration (polar caps) exist where $\theta_{Bn} \leq 45°$. They are separated by a zone where the shock is quasi-perpendicular (equatorial region) and the particle acceleration is suppressed. As the SNR shock expands, the acceleration zone is growing and new particles enter the region of active particle acceleration. These particles, newly added to the population of accelerated ions, just have started the DSA cycle and therefore have lower energies. In total this yields an enhanced production of ions with lower energies and thus a steepening of the spectrum [174].

---

[22] We use the same condition as in the previous chapter to determine whether a particle is in the tail, $E > 10 E_{sh}$, where $E_{sh} = \frac{1}{2} m_p v_0^2$.
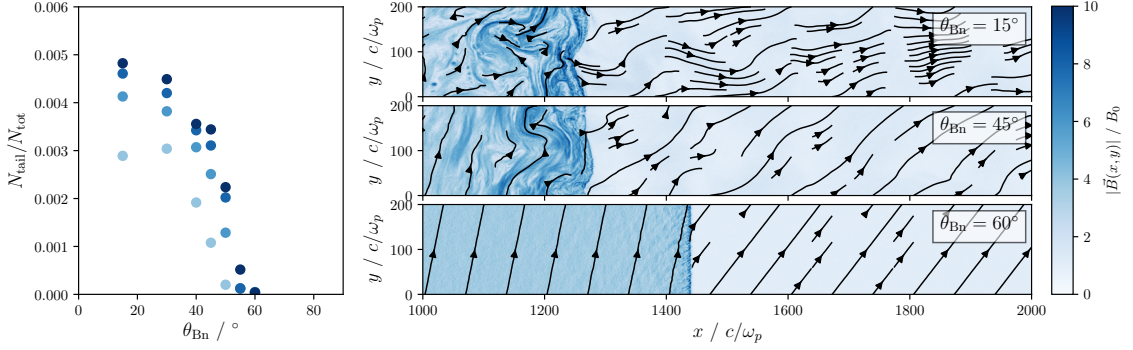
FIGURE 30: (left) Fraction of energetic particles in the power-law tail as measure of the injection efficiency as function of the shock inclination. The different shades encode different times in the range $100\,\omega_c^{-1} \le t \le 400\,\omega_c^{-1}$. (right) Magnetic field and field lines in the simulation plane for three shock inclinations at $t = 400\,\omega_c^{-1}$. All simulations have been initialized with an upstream bulk velocity of $v_0 = 10\,v_A$.

But also another mechanism is connected to the variability of the angle between shock normal and background magnetic field. In particular, if zones of different shock inclination coexist, particles can diffuse from the active zone, where they are injected and accelerated, to a zone where the shock is oblique. In this region particle acceleration is suppressed and hence also turbulence confining the particles is absent, and they are lost from the acceleration. Typically the diffusion coefficient is a function of energy, therefore a steeper spectrum can be expected. In this case a time-dependence of the size of the acceleration region is not required to explain the steepening in contrast to the mechanism presented in [174]. Hence, a reduction of the model to a planar shock is reasonable[23]. This potential possibility for the steepening of CR spectra is investigated in the following. In particular, we are considering "patchy" shocks where the direction of the magnetic field varies along the shock front. This kind of setup of changing magnetic field direction ahead of the shock changes might either be caused by preexisting turbulence in the ISM or it arises due to magnetic perturbations caused by the cyclotron instability of energetic particles diffusing ahead of the shock or escaping from the accelerator. In both cases we expect a variation of the shock geometry on scales larger than the Larmor radii of low-energy ions but considerably smaller than the remnant size.

The particle acceleration in spherically expanding SNR blast waves was investigated recently for different magnetic field morphologies using a hydrodynamic model [118]. This allowed the authors of [118] to consider the obliquity dependence of particle acceleration on large scales. However, these simulations are not fully self-consistent as they rely on inputs from simulations where the ion population is treated kinetically. The effect of shock inclination on the injection of nonrelativistic particles into the DSA has been investigated by means of hybrid simulations for homogeneous background magnetic field [27].

In the following we study the influence of a variable orientation of the magnetic field on ion acceleration and investigate whether an inhomogeneity in form of a variation of

---

[23]   Generally, in the case of low energy particles, a spherical shock should yield the same results, as long as the shock curvature is unimportant.

the shock obliquity along its face can produce the necessary extra steepening of the CR spectra. As the particle energy remains relatively low and the size of the system can be kept reasonable, hybrid simulations provide a suitable tool for studying this steepening mechanism. The majority of the results presented below have been published in [24], but here we provide some additional details.

5.2 Simulation Setup

Different setups for shocks propagating into inhomogeneous magnetic fields have been investigated using hybrid as well as fully kinetic particle-in-cell (PIC) simulations, however, focusing on other aspects. In [175, 124] the interaction between the solar wind and a planetary magnetic field has been explored. In this case a shock with variable inclination naturally arises due to the formation of a bow shock in the solar wind. In [176] shocks occurring due to the expansion of a blast shell in an uniform magnetic field were analyzed using fully kinetic PIC simulations. While this setup resembles the expansion of a SNR shock to some extent, spatial and temporal scales are completely different. Hybrid simulations of collisionless shocks including large scale magnetic turbulence that has been prescribed in the upstream plasma have been performed in [35], however, with a focus on the acceleration of electron test-particles. As in the studies mentioned above we use a model with reduced dimensionality, i.e., the spatial dimension is reduced to 2D, while all components of the velocity and fields are kept. The shock propagates in the x-direction, hence, we vary the magnetic field direction and thereby θ_{Bn} as function of the transverse coordinate, y. To ensure $\nabla \cdot \vec{B} = 0$, the prescribed background fields have to be chosen properly. We set B_x and B_z as functions of y, which fulfill Gauss' law for magnetism. Additionally, we require the strength of the magnetic field to be constant, $|\vec{B}(y)| = B_0 = const$. We have used two different setups for the background magnetic field, both are depicted in Fig. 31. In the first setup the magnetic field is prescribed as

$$B_x(y) = B_0 \sin\left(\frac{\pi y}{L_y}\right), \qquad B_y(y) = 0, \quad \text{and} \quad B_z(y) = B_0 \left|\cos\left(\frac{\pi y}{L_y}\right)\right|. \qquad (97)$$

Therefore, the scale length of the magnetic field is twice the transverse size of the simulation box, L_y. In the second setup we include a full period of the variation of the field direction in the simulation box and use

$$B_x(y) = B_0 \cos\left(\frac{2\pi y}{L_y}\right), \qquad B_y(y) = 0, \quad \text{and} \quad B_z(y) = B_0 \sin\left(\frac{2\pi y}{L_y}\right). \qquad (98)$$

In general, the scale of the inhomogeneity of the magnetic field can be as small as the resonant wavelength of suprathermal particles and reach sizes as large as the radius of the SNR shock. The choice of scale length in our case is somewhat arbitrary. However, the important point is that the regions of active and suppressed particle injection coexist along the shock front and the physics of the transition between these regions is covered. The computational resources limit the size of the scale length, due to its relation to the size of the simulation box. Since simulations with extremely large boxes are computationally very

demanding if the particle statistics is kept high, we refrain from using also a larger scale length or other, spatially more complicated geometries of the magnetic field, which could be of interest. Because of the computational constraints we only considered the case of a pure hydrogen plasma. Note that the setup of the magnetic field, Eqs. (97) and (98), contains a component out of the simulation plane. To make sure that this does not influence the acceleration dynamics significantly, additional simulations of a quasi-parallel collisionless shock with a homogeneous upstream magnetic field with an out-of-plane component have been performed.

The simulation is initialized as depicted in Fig. 11, with the plasma moving in $-x$-direction and a reflecting wall positioned at $x = 0$. Ions and electron fluid are initialized in thermal equilibrium with $\beta_e = \beta_i = 1$.
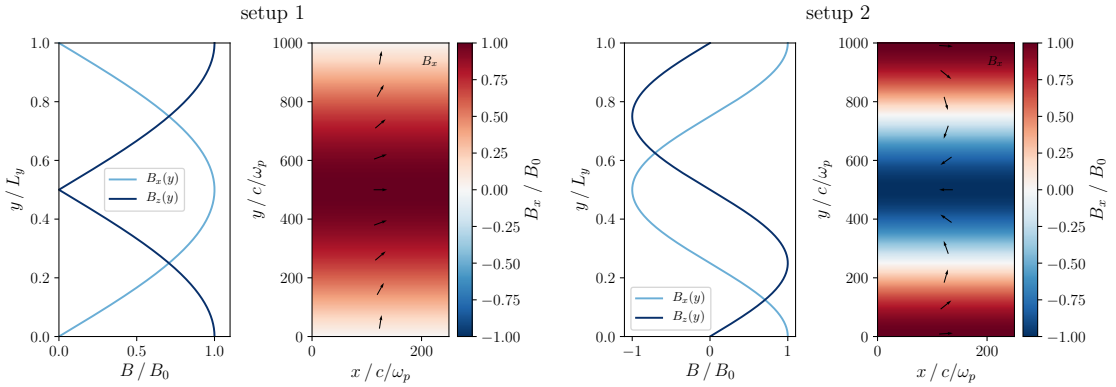

FIGURE 31: Configuration of the background magnetic field for simulating a shock with variable obliquity. In "setup 1" only a half cycle of the variation is included, while in "setup 2" a whole cycle is embedded in the simulation box.

The initial electric field is calculated using Eq. (51), where the pressure term at $t = 0$ is zero as the ions are initially distributed evenly across the simulation domain. The Lorentz force, $\vec{F}_{\mathrm{L}} = q_i (\vec{E} + \vec{v} \times \vec{B})$, is zero in the far upstream[24]. Therefore, the whole setup is expected to be stable. This has been checked by performing a simulation with periodic boundary conditions also in the x-direction. The size of the simulation box was chosen as $L_x \times L_y = 1000 \times 1000 \ (c/\omega_p)^2$. In Fig. 32 we plot the x-component of the magnetic field as well as the velocity distribution as they are initialized at $t = 0 \, \omega_c^{-1}$ and after $t = 200 \, \omega_c^{-1}$. Additionally to $B_x(x, y)$ we show the y-dependence of B_x at $x = 200 \, c/\omega_p$ as black line. The setup remains stable and only the fluctuations arising due to the finite number of simulation particles are visible in the magnetic field at $t = 200 \, \omega_c^{-1}$. The velocity distributions, $f(v_x)$ and $f(v_y)$, shown in the right panel of the figure, stay unchanged and no sign of instability or heating can be observed.

We have also investigated the dependence of the results on the scales of the field variation. Therefore simulation runs initialized according to "setup 1" for different values of L_y have been analyzed. The resulting spatially dependent ion densities and magnetic fields are plotted in Fig. 33 for $L_y = 250 - 1000 \, c/\omega_p$. While the structure of the magnetic field changes when increasing the transverse box size from $L_y = 250 \, c/\omega_p$ to $L_y = 500 \, c/\omega_p$,

---

[24] While fluctuations arise due to the limited number of simulation particles, the average should be zero.
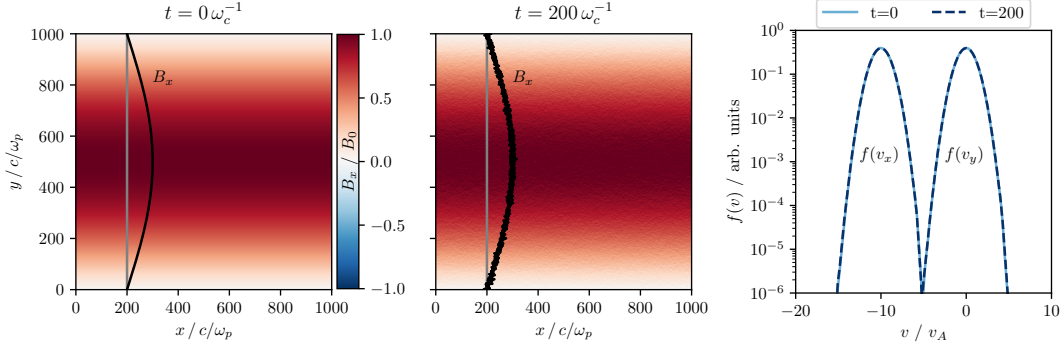
FIGURE 32: Initial $B_x(x,y)$ for a simulation according to "setup 1" (left) and after $t = 200\,\omega_c^{-1}$ (middle). The black line shows a slice of the the x-component of the magnetic field along $x = 200\,c/\omega_p$. (right) Velocity distributions, $f(v_x)$ and $f(v_y)$, of protons at $t = 0\,\omega_c^{-1}$ (solid line) and $t = 200\,\omega_c^{-1}$ (dashed line). No signs of heating or instability are visible.

for the two largest values for L_y the pattern of the density and magnetic field does not change significantly. The downstream energy spectra at $t = 300\,\omega_c^{-1}$ for these simulations (see Fig. 34) show the influence of the transverse box size and the connected scale length of the magnetic field variation on the spectrum. For the smallest box with $L_y = 250\,c/\omega_p$ the power-law tail generation is suppressed because regions of active and marginal injection are not well separated. In this case a significant part of the injected ions can move to regions where the shock is quasi-perpendicular and gets lost for the acceleration process. Increasing L_y from $750\,c/\omega_p$ to $1000\,c/\omega_p$ leaves the downstream energy spectrum practically unchanged.

Hence, in the following we perform simulations using a box with the size $L_x \times L_y = 8000 \times 1000\,(c/\omega_p)^2$ with a cell size of $\Delta x = \Delta y = 0.5\,c/\omega_p$, 16 simulation particles per cell and a time resolution of $\Delta t = 10^{-3}\,\omega_c^{-1}$.
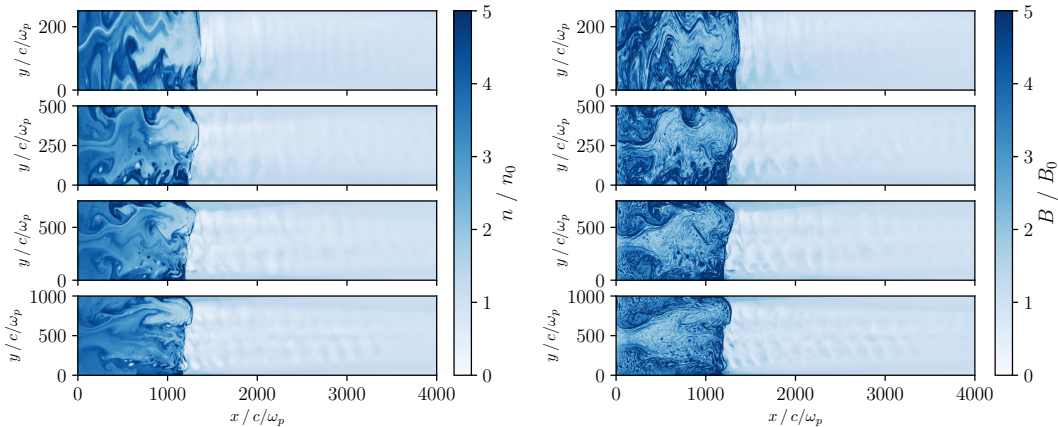

FIGURE 33: Ion density $n_i(x,y)$ (left) and magnitude of the magnetic field $|\vec{B}(x,y)|$ (right) at $t = 300\,\omega_c^{-1}$ for simulations with different extensions in y-direction. In all cases the simulation has been initialized with an upstream bulk velocity of $v_0 = 10\,v_A$.
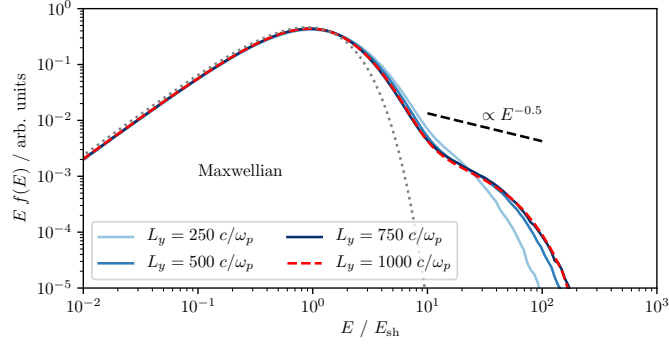
FIGURE 34: Downstream energy spectra for simulations initialized with a magnetic field configuration according to "setup 1" with different transverse box sizes $L_y = 250 - 1000\,c/\omega_p$. The energy is measured in terms of $E_{\mathrm{sh}} = \frac{1}{2}\,m_p\,v_0^2$.

5.3 Results

A distinct behavior along the shock surface can be expected for a shock propagating into a medium with variable orientation of the magnetic field, as the physics depends largely on the angle between the shock normal and the magnetic field. To illustrate this we plot in Fig. 35 the magnitude of the magnetic field $|\vec{B}(x,y)|$ for both setups at $t = 300\,\omega_c^{-1}$ well after the shock has developed and consider three regions: (1) $\theta_{\mathrm{Bn}} \approx 0°$, (2) $\theta_{\mathrm{Bn}} \approx 45°$, and (3) $\theta_{\mathrm{Bn}} \approx 90°$. These regions are marked in Fig. 35a by red rectangles. The individual components of the magnetic field in these regions (averaged over y) are depicted in Fig. 35b)-d). In the spatial distribution of the magnetic field, Fig. 35a), it can be seen that the shock front differs considerably from a planar shape for both setups, as the shock position in propagation direction varies up to $100\,c/\omega_p$ across the shock front. We have calculated the shock velocities in the regions where the shock is parallel/perpendicular and found no difference in the shock velocities maintained over the whole runtime of the simulation. The non-planar shape of the shock front results in additional local variations of the shock obliquity, however, this effect can also occur in shocks with constant obliquity due to shock rippling [146]. The theory predicts injection to be efficient at quasi-parallel shocks. In this case ions can return from the shock and excite waves in the upstream plasma[25]. Correspondingly, waves are present in the upstream in the regions of $\theta_{\mathrm{Bn}} \approx 0°$ and $\theta_{\mathrm{Bn}} \approx 45°$, see Fig. 35b)-c) for both simulation setups. As time progresses, these waves are advected with the plasma and the field is compressed upon shock crossing. In the region where the angle between the shock normal and the magnetic field is large ($\theta_{\mathrm{Bn}} \approx 90°$, panels d) in Fig. 35, no wave activity is visible upstream of the shock.

To visualize the particles that are responsible for wave excitation in the upstream, we have calculated the density of protons with a velocity component, v_x, directed towards the upstream. The result is depicted in Fig. 36 in a region around the shock transition for "setup 1" (panel a) and "setup 2" (panel b) as well as for strictly quasi-parallel shock with $\theta_{\mathrm{Bn}} = 20°$ (panel c). In all cases the upstream and downstream regions are easily

---

[25] This has been observed in hybrid simulations of collisionless shocks in homogenous magnetic fields with different shock inclinations [27].
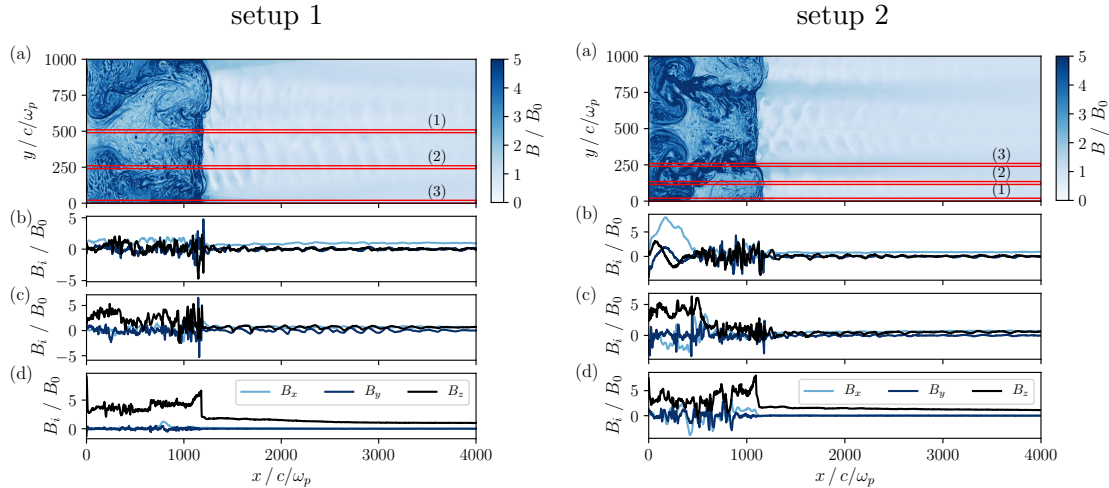
setup 1 setup 2

Figure 35: (a) Amplitude of the magnetic field $|\vec{B}(x,y)|$ at $t = 300\,\omega_c^{-1}$ for "setup 1" (left) and "setup 2" (right). The red rectangles denote regions in which the shock is parallel (1), oblique (2), and perpendicular (3). Panels (b-d) show the components of the magnetic field in these regions.

distinguishable. As the direction of the velocity is randomized upon shock crossing and the downstream region is turbulent (see, e.g., Fig. 35) a large number of protons in the downstream has a positive v_x which leads, together with the higher total density of ions in the downstream, to large values of $f(x, y, v_x > 0)$. In the upstream most ions have a velocity directed towards the shock and the density of particles with $v_x > 0$ is low. Only particles that are reflected from the shock or have entered the acceleration mechanism and gained some energy can have upstream directed velocities. For the simulation with constant obliquity ($\theta_{Bn} = 20°$) the density of ions with $v_x > 0$, Fig. 36c), is almost homogeneous and variations are only visible close to the shock transition. In the case of variable shock inclination, a dependence of the density on the transverse coordinate, i.e., the shock inclination, is obvious, Fig. 36a)-b). In particular, the density of particles with positive v_x in the upstream decreases for $\theta_{Bn} > 45°$, and for $\theta_{Bn} > 75°$ almost no ions have $v_x > 0$. This behavior is the same for both simulation setups and can be attributed to the fact that the injection is suppressed for $\theta_{Bn} > 45°$ and only a few ions diffuse into the region $\theta_{Bn} > 75°$.

To investigate the effect of a variable shock obliquity on the spectral index, a comparison of the energy spectra from simulations with variable and constant shock obliquity is necessary. Therefore, we calculate the particles spectra in regions of different shock obliquity as well as integrated over the whole downstream region and compare them to results obtained for a quasi-parallel shock. As an effective injection of particles into the energization mechanism only occurs in some parts of the simulation box for a varying shock inclination, a different behavior of the energy spectra obtained at miscellaneous locations in the simulation box is expected[26]. In Figure 37 we compare the downstream energy spectra obtained from a simulation with constant shock inclination and a simulation run

---

[26] A spatially dependent momentum spectra was also found in [177], where the Parker transport equation was solved for a system containing a large scale sinusoidal magnetic field variation.
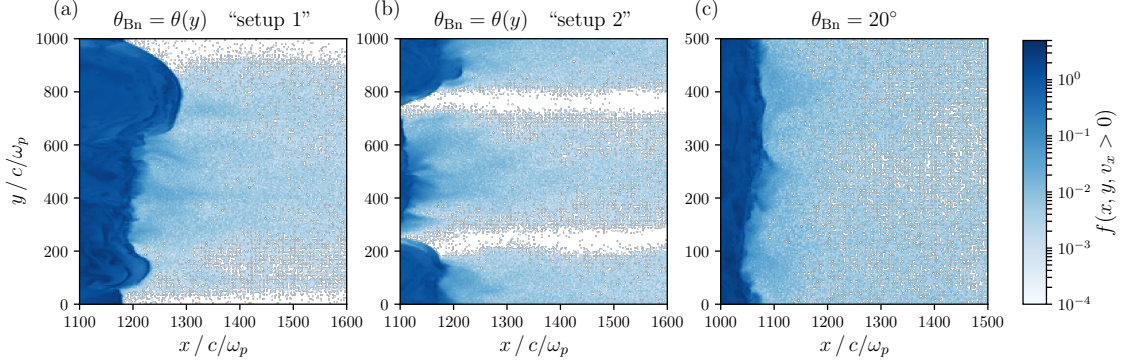
FIGURE 36: Density of protons with positive v_x in the shock vicinity at $t = 300\,\omega_c^{-1}$ for (a) a simulation initialized according to "setup 1", (b) "setup 2", and (c) for a simulation of a quasi-parallel shock with $\theta_{\mathrm{Bn}} = 20°$.

with variable magnetic field direction according to "setup 1". The spectra are measured at two different times, $t = 200\,\omega_c^{-1}$ and $t = 400\,\omega_c^{-1}$. The spectrum for a quasi-parallel shock (blue line in Fig. 37) shows the characteristic thermal and power-law parts with the power law extending in energy as time progresses. The red lines in Fig. 37 denote the spectra obtained from a simulation with variable magnetic field direction. In the region where the shock is quasi-parallel ($\theta_{\mathrm{Bn}} < 45°$, dotted line) the energy spectrum at $t = 200\,\omega_c^{-1}$ almost coincides with the spectrum from the simulation with constant obliquity. This is partially due to the fact that the dependence of the injection on the shock inclination is weak as long as the shock is quasi-parallel [27]. By the end of the simulation, $t = 400\,\omega_c^{-1}$, a slight difference in the spectral slope becomes visible, which is caused by the diffusion of ions into regions where the shock is quasi-perpendicular. For purely quasi-perpendicular shocks usually no power-law tails are observed[27]. Ions are only mildly energized by a few cycles of shock drift acceleration (SDA) before being transmitted downstream. Nevertheless, we observe a population of energetic particles in the downstream for $\theta_{\mathrm{Bn}} > 60°$, indicated by the red shaded area. At $t = 400\,\omega_c^{-1}$ this is even more pronounced and the spectrum resembles a power law with a cutoff for high energies. The downstream spectrum integrated over the whole width of the simulation box (solid line) also exhibits a power-law tail, however, with a lower normalization as particle injection is not efficient throughout the entire simulation box.

The origin of the energetic particles in the quasi-perpendicular region (see shaded region in the downstream energy spectrum, Fig. 37) from parts of the simulation box where the shock is quasi-parallel can be confirmed by following these particles in time. In the first panel of Fig. 38 the considered energy spectrum is reprinted with the energy region of the particles that are followed marked. The other panels show the positions of the particles of interest, and in the background the amplitude of the magnetic field is plotted. It is obvious that these ions originate from regions with $\theta_{\mathrm{Bn}} < 60°$, and at $t = 100\,\omega_c^{-1}$ most of them have not yet reached the shock. As time progresses these ions encounter the

---

[27]   However, a formation of a power-law tail has been reported even for quasi-perpendicular shocks in the case of prescribed fluctuations in the upstream [178] as well as for perpendicular shock in partially ionized medium [179].
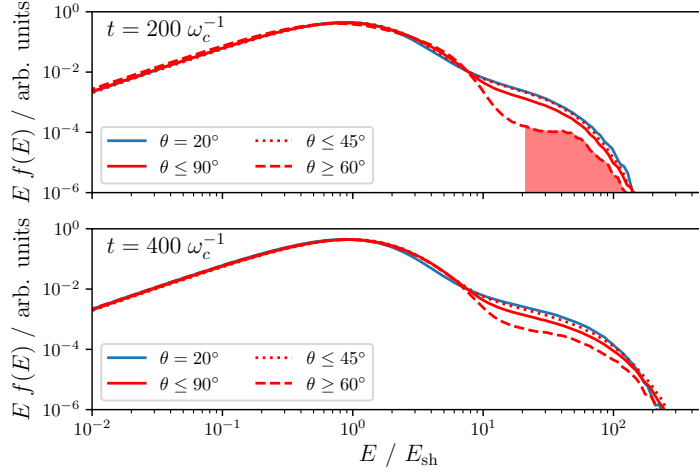
FIGURE 37: Downstream energy spectra for a simulation of a quasi-parallel shock (blue) and a shock with variable obliquity ("setup 1", red) earlier in the simulation, $t = 200 \, \omega_c^{-1}$, and at $t = 400 \, \omega_c^{-1}$. For the setup with variable obliquity the spectra are calculated in different regions: in the whole box (solid line), in the region where the shock is quasi-perpendicular (dashed line) and quasi-parallel (dotted line).

shock and get accelerated. In the turbulent downstream plasma the ions then move to the region where the shock normal makes an angle $\theta_{\mathrm{Bn}} > 60°$ with the background magnetic field. This means that the acceleration starts in regions where the injection efficiency is high, i.e., where the shock is quasi-parallel. However, as the magnetic field direction varies along the shock front some of the injected and accelerated particles might leave the active acceleration zone moving towards regions where the shock is quasi-perpendicular. This diffusion alters the spectral slope since a population can escape the acceleration mechanism in an energy dependent fashion.
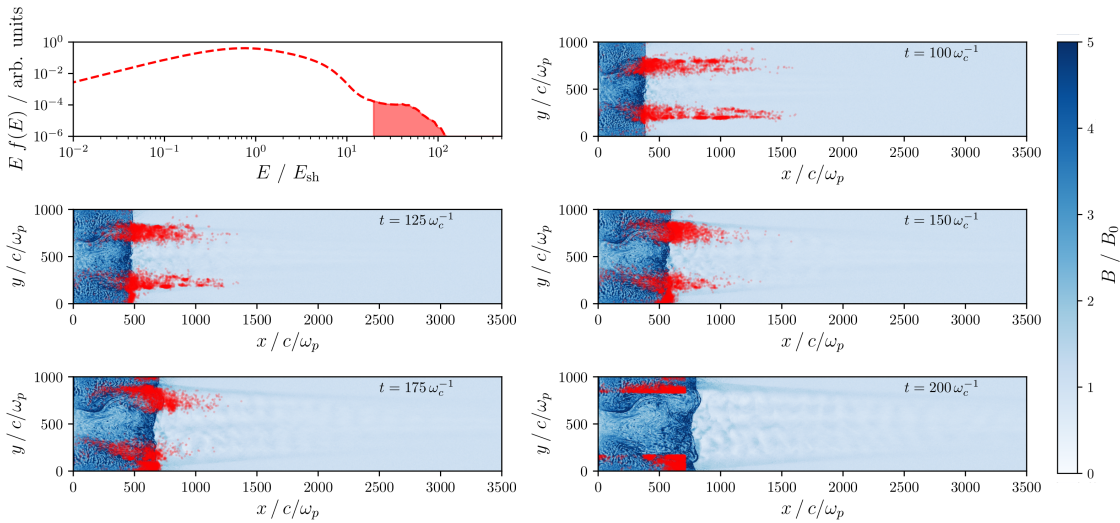

FIGURE 38: To determine the origin of the energetic particles in the quasi-perpendicular region (shaded region in the energy spectrum) the particles are identified and their positions (red dots) are plotted at earlier times. For reference the amplitude of the magnetic field $|\vec{B}(x,y)|$ is shown in the background.

The change in the spectral slope is already indicated in the energy spectra depicted in Fig. 37. To quantify this effect the spectral index,

$$q = -\frac{d \ln(f(E))}{d \ln E}, \tag{99}$$

has to be computed. In principle this energy dependent spectral index could be calculated directly from the energy spectra of the ions in the downstream. However, since only a small fraction of the particles ends up in the power-law tail this is prone to noise, especially in the high energy region of the power law where the particle statistics is low. Hence, we first calculate

$$\tilde{q} = -\frac{\ln(f(E))}{\ln E} \tag{100}$$

from the energy spectra, which were obtained using a logarithmic binning. The data points are denoted by "+" markers in Fig. 39. Using these data points, a smooth spline is calculated using the `scipy` python library (dotted line in Fig. 39). Finally, we calculate the spectral index according to Eq. (99) from the spline function. We compare the spectral index from a simulation of a quasi-parallel shock with constant shock inclination (blue) to our two setups with variable obliquity (red and dark red). For all three simulations the formation of a power law starting around $E \approx 10\,E_{\mathrm{sh}}$ can be observed. The transition from the thermal part of the spectrum is smoothed out due to the presence of suprathermal particles. Towards higher energies an exponential cutoff is visible (see also Fig. 37), which is caused by the finite simulation runtime and can also be influenced by the limited extension of the system. Both transitions at low and high energies limit the energy range where a clear power-law behavior can be observed. We find that $\tilde{q}$ is almost flat for $10\,E_{\mathrm{sh}} < E < 50\,E_{\mathrm{sh}}$. The upper boundary of the energy region in which a clear power law can be observed should increase with time. However, we are here limited by the available computational resources preventing simulation runs with considerably larger simulation boxes and run times. Nevertheless, we find that the variable shock inclination influences the value for the power-law exponent already at $t = 400\,\omega_c^{-1}$. It can be seen that the power-law index, q, is larger for the setups with varying shock obliquity and the difference is as large as $\Delta q = q_{\mathrm{var}} - q_{\mathrm{const}} = 0.1 - 0.15$. The apparent discrepancy with the correct asymptotic index $q = 1.5$ for $\theta_{\mathrm{Bn}} = 20°$ is due to the limited simulation time. While the obtained Δq might seem negligible at first glance, it is nevertheless significant. Firstly, as presented earlier in Chapter 4 (and also in [29]), the precise measurements in combination with the distinct predictions provided by the DSA have already shown that small variations in the spectral index can be meaningful and help solving the puzzle of CR acceleration. Additionally, we are confident that the observed spectral steepening will increase for larger box sizes and longer simulation times. Hence, we expect Δq to increase for a more realistic representation of the SNR environment.

5.4 Conclusion

Using hybrid simulations, we have investigated the influence of an inhomogeneous magnetic field geometry on particle acceleration at collisionless shocks. We have performed a series
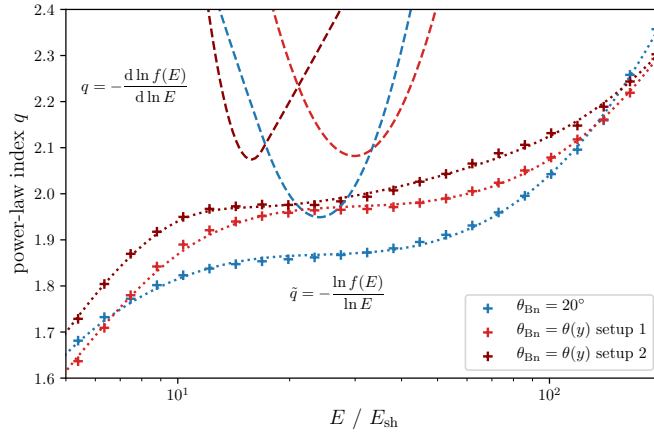
FIGURE 39: The power-law spectral index, q, obtained from the downstream energy spectra for a simulation of a quasi-parallel shock with $\theta_{\mathrm{Bn}} = 20°$ (blue) as well as for the setups with variable field inclination (red and dark red). The spectra obtained in the latter case are steeper and a larger value for the spectral index is obtained.

of simulations with a variable magnetic field direction in the upstream, which leads to different shock inclinations along the shock front. This geometry affects the power-law index of the spectrum of the accelerated ions in the downstream. This phenomenon can help to understand the puzzling steepness of the propagation-corrected CR spectra which is unaccounted for by the DSA-predictions. Our setup facilitates the coexistence of regions of quasi-parallel and quasi-perpendicular shock geometries in one simulation box, resembling a shock propagating into a medium with a turbulent magnetic field aligned in different directions. As expected, we find ions to be injected efficiently into the acceleration mechanism only in regions where the shock is quasi-parallel. The acceleration also proceeds in this region, however, particles can diffuse into other regions, where the shock inclination is larger and the injection and acceleration are suppressed. Since these particles remain in the downstream and are inhibited to repeatedly recross the shock they are lost to the acceleration mechanism. This results in a downstream energy spectrum that is measurably steeper than the spectrum obtained for a quasi-parallel shock. The observed change of the spectral index $\Delta q = q_{\mathrm{var}} - q_{\mathrm{const}} = 0.1 - 0.15$ is likely to increase for larger scales of the inhomogeneity of the magnetic field, i.e., larger system sizes, modeling the SNR environment more realistically. Since the mechanism presented here works at relatively low energies, other mechanisms[28] might take over at higher CR energies.

As we have shown in the previous chapter, see Fig. 15, the presence of helium ions, even if their number density compared to the protons is small, has an influence on the wave spectrum and particle injection. Hence, the interesting question arises, whether a self-consistent inclusion of an additional population of He^{2+} ions would alter the dependence of proton injection on the shock inclination as well as the injection and acceleration in shocks with variable field direction. To take a first step in this direction we have performed two-dimensional simulations of shocks with different field inclinations and compared results

---

[28] Such as an energy loss to the amplified magnetic field [173] or a combination of the obliquity dependent injection efficiency with the shock geometry and shock evolution [174]

from simulations that contain an additional population of helium ions contributing with 10 % to the plasma composition to results for the pure hydrogen plasma. In particular, we have analyzed the fraction of particles and energy in the tails of the distribution functions. Simulation boxes with sizes of $L_x \times L_y = 20000 \times 200 \, (c/\omega_p)^2$, at least 25 particles per cell per species, and spatial resolution $\Delta x = 0.5 \, c/\omega_p$ were used to assure converged results. The shock evolution and particle acceleration was followed for $400 \, \omega_c^{-1}$. After this time we have calculated the fraction of particles in the power-law tail as well as the fraction of energy in the tail for the downstream plasma, where the condition $E > 10 \, A \, E_{\mathrm{sh}}$, with A being the mass number, was employed to determine whether a particle is in the tail. The results are depicted in Fig. 40, where on the left the pure proton case is shown, while on the right protons and helium ions were present in the simulation. As expected, the fraction of energetic particles and the fraction of energy in the power-law tail drops fast for shock inclinations above the critical value of $\theta_{\mathrm{Bn}}^{\mathrm{crit}} = 45°$. This can already be observed at earlier times, see Fig. 30. The results shown in Fig. 40 indicate that the shock obliquity dependence of the proton injection efficiency changes if helium ions are present. In this case the injection efficiency of protons first increases as the critical shock inclination is approached, before it drops quickly for even larger θ_{Bn}. In turn, the injection of He^{2+} is monotonically decreasing with increasing shock inclination similar to the pure proton case in the right panel. This can also be seen from the dotted and dashed lines which represent phenomenological fit functions[29] to the data extracted from the simulation.
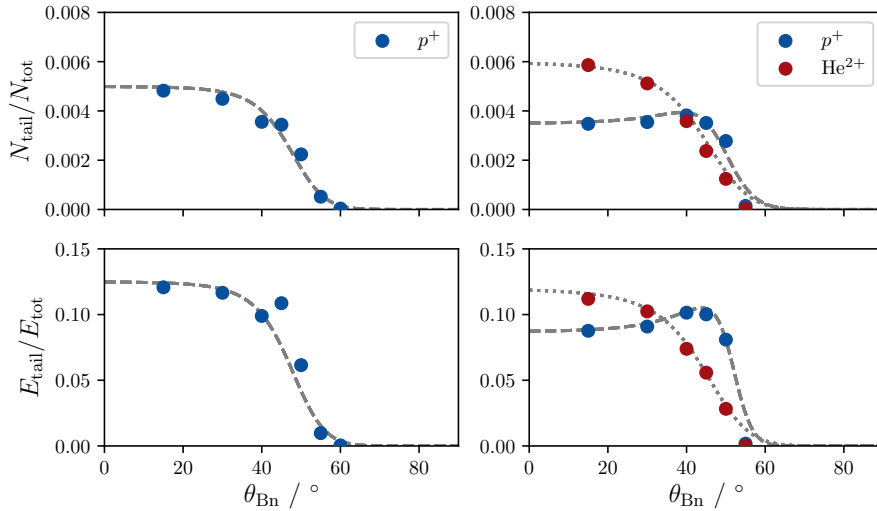

FIGURE 40: Dependence of the injection on the shock inclination for a pure hydrogen plasma (left) and a proton-helium mixture containing 10% He^{2+} ions (right) An influence on the injection of protons is visible when an additional component of helium ions is included in the simulation. The results presented here are for an upstream bulk velocity of $v_0 = 10 \, v_A$ and are measured at $t = 400 \, \omega_c^{-1}$.

These preliminary results lead to the conclusion that a further investigation of the injection and acceleration of ions at shocks with variable magnetic field direction in proton-helium plasmas is worthwhile. The self-consistent inclusion of helium ions would provide a

---

[29] The functions have the form $f(\theta) = \frac{a}{2} \left(1 - \tanh \left(\frac{\theta - \theta_{\mathrm{crit}}}{b - c \, \theta} \right) \right)$ and $g(\theta) = f(\theta) \left(1 + d \exp \left(\frac{\theta - e}{f} \right) \right)$.

more realistic model of the composition of the ISM and, furthermore, would allow to capture additional effects, such as the waves generated by the helium ions. This investigation remains as a future project.

CHAPTER 6

Electron-Heating in Quasi-Parallel Shocks

6.1 Motivation

Until now we have considered the injection of ions into the diffusive shock acceleration (DSA). This focus is natural in the context of hybrid simulations as the model disregards the electron kinetics, which is appropriate as shock structure and timescales are determined by the ions. We were investigating particular features in the ion spectra, which have now been measured with great accuracy, while the CR electron flux on Earth is several orders of magnitude lower. Nevertheless, observations of supernova remnants (SNRs) in the X-ray regime indicate a quite efficient acceleration of electrons up to energies on the order of several tens of TeV, which can be deduced from their synchrotron emission [31, 32]. Satellite missions allow for *in situ* measurements of particle acceleration signatures at shocks in the Solar system, such as Earth's bow shock [180, 181]. In this environment efficient electron acceleration is found to occur in a quasi-perpendicular shock geometry while quasi-parallel shocks are favorable for ion acceleration [182, 183]. However, SNR shocks, which are the most probable acceleration sites for cosmic rays (CRs) (including electrons), are much stronger and considerably larger than Earth's bow shocks. Their remote observations and also *in situ* measurements at Saturn's bow shock, the strongest shock in the Solar system, indicate that electrons are also accelerated efficiently in the quasi-parallel shock geometry [184].

While the injection of ions into the DSA is still not fully understood, the injection of electrons is even more puzzling. In the previous chapters we tried to shed some light on particular aspects of the injection of ions and investigated how different parameters influence the spectra of the accelerated particles. However, until now no adequate model of the whole injection process has been presented. In the context of electron injection, the question arises whether electrons are able to generate turbulence on the respective scales to facilitate injection or some "assistance" by the ion component is necessary. Especially at quasi-parallel shocks the latter appears critical, which in turn raises the question whether accelerated protons can generate the turbulence necessary for electron injection.

The acceleration of electrons has been mostly investigated by means of fully kinetic particle-in-cell (PIC) simulations and almost exclusively for the quasi-perpendicular shock geometry. In such an environment, whistler waves were found to be crucial for electron injection [185]. Other investigations report that electrostatic waves excited by the Buneman instability and accompanied by particle trapping are vital for efficient electron acceleration [186, 187, 188, 189, 190]. It is important to note here that in fully kinetic simulations artificially increased electron-to-ion mass ratios are often used to reduce the numerical ef-

fort and obtain converged results within finite time. This, however, might have an impact on the results, see, e.g., the investigation of the mass ratio dependence of the Buneman instability in [189] or discussions in [191, 84, 120]. Electron acceleration at quasi-parallel shocks was investigated recently in [95], where the authors found that waves excited by Bell's instability [112] are responsible for scattering and injection of both, electrons and ions.

In the context of collisionless shocks not only the injection and acceleration of electrons to high energies is of interest. The low energy part of the spectrum also deserves attention. In this energy range the thermalization of electrons is a major aspect, which is important for the analysis of the observed X-ray spectra. Furthermore, it is essential (along with electron acceleration, though) to understand the energy partitioning between the thermal population and the accelerated CR particles. In collisionless shock environments the particle mean free path is much larger than the shock thickness, therefore, an equilibration of electron and ion temperatures might only occur on very long timescales. This uncertainty in the behavior of the electron temperature can influence hybrid simulations, where aside from the usual adiabatic equation of state for the electron fluid also polytropic equations of state have been used to model a possible temperature equilibration [97].

Observations of Balmer-dominated shocks can give insights into the downstream temperature ratios of electrons and ions. In shocks propagating into partially ionized medium a hot neutral population is created in addition to the cold neutral hydrogen. This is due to charge exchange between hot downstream ions and cold neutrals, which do not interact with the shock. These shocks are observable via the optical emission of collisionally excited hydrogen (Balmer lines). From the widths of the broad and narrow components of the Hα line profile, information about the shock velocity and the temperature ratio can be extracted [33]. The observation of the electron-ion temperature ratio in different SNR shocks indicates that this quantity is a decreasing function of shock velocity. A similar behavior of the temperature ratio as function of the shock Mach number, M, was found recently in fully kinetic simulations of low M quasi-perpendicular shocks [192].

6.2   Introducing Electrons as Test-Particles

While fully kinetic PIC simulations are the most fundamental approach of modeling electron acceleration at collisionless shocks numerically, they are computationally very expensive due to the disparity of electron and ion scales. Hence, increased electron-ion mass ratios are regularly used. A different approach to the investigation of electron acceleration by means of numerical simulations has been taken in [193, 35, 36]. Instead of performing expensive fully kinetic PIC simulations, the authors introduce a population of test-particle electrons and propagate them in the fields obtained from hybrid simulations. In this way they investigate the influence of shock surface and magnetic field variations on electron acceleration at quasi-perpendicular shocks. This approach was first adopted by Kraus-Verban *et al.* [34], and to quote [62, p. 286]: "This unusual mixed self-consistent and test particle model allows the use of realistic electron-ion mass ratio and the macroscopic shock fields." Consequently, studying electron trajectories in turbulent fields generated

by the ion component is worthwhile as long the stochastic fields from hybrid simulations resemble the reality, and there are reasons to believe this. The drawback of this approach is that any electron scale turbulence and the associated scattering is neglected.

A contribution of suprathermal electrons is usually neglected in hybrid simulations (this is also true for our hybrid model, see Sec. 3.1). This is a reasonable assumption if their number density is small and the simulation results are not affected significantly. However, while this component might be low in density and unimportant for the simulation dynamics, it can be of significance for observations. In the spirit of the approach presented in [193, 35, 36], we aim to study the behavior of electrons in quasi-parallel shocks beyond the hydrodynamical treatment. Therefore, we introduce electrons as test-particles in hybrid simulations and investigate their thermalization in the proton-driven turbulence.

To reduce the computational effort, we use a one-dimensional (1D) model, which allows us to increase the number of simulation particles, yielding low noise levels in the electromagnetic fields. While a realistic alternative to 1D, a 2D model, would allow to include effects like shock corrugation, it has some drawbacks beyond higher computational costs. Additionally to the inverse cascade present in 2D, a recent comparison between 2D and 3D modeling has shown that in the 2D modeling an artificial enhanced acceleration of electrons can be observed due to the trapping of particles in fluctuations at the shock surface [36].

The simulation is initialized by sending a super-sonic and super-Alfvénic hydrogen plasma flow with velocity v_0 against a reflecting wall, placed at $x = 0$, Fig. 11. The addition of test-particles[30] in our hybrid model is easily achievable, however, the separation of electron and ion scales requires the implementation of some additional steps. In particular, to correctly resolve the electron motion, a subcycling is introduced. The electron positions and velocities are updated N_{cyc} times during one time step of the main proton component. This allows to reduce the effective time step for the test-electrons to $\Delta t_e = \Delta t / N_{\text{cyc}}$. At each sub-step the electromagnetic fields are obtained by a linear interpolation. The time step for the ion component depends on the upstream bulk velocity, $\Delta t = 0.01 (c/\omega_p)/v_0$, and the test-electron positions and velocities are updated 20 times during one time step for the ions. The test-eletron particles have a slightly increased mass, $m_e = 1/400 \, m_p$. We use a cell size of $\Delta x = 0.25 \, c/\omega_p$ with at least 1000 simulation particles per cell for the ion component to keep the numerical noise level low. This is necessary to avoid an artificial heating of the test-particle electrons. We have performed convergence studies with varying numbers of protons per cell, N_{ppc}, and calculated the downstream velocity distributions, $f(v_z)$, of electrons and ions. The results are depicted in Fig. 41. The velocity distribution of the protons shows little variation with N_{ppc}, while the velocity distribution of the test-particle electrons clearly changes with N_{ppc}, and we observe converged results only for $N_{\text{ppc}} > 400$. For fewer particles per cell strong nonthermal tails are visible in the velocity distribution of the electron test-population, indicating an artificial heating.

The ions and the electron fluid are initialized in thermal equilibrium with $\beta_e = \beta_i = 1$.

---

[30] The test-electrons, by definition, do not generate electric or magnetic fields, neither exert pressure on the background plasma.
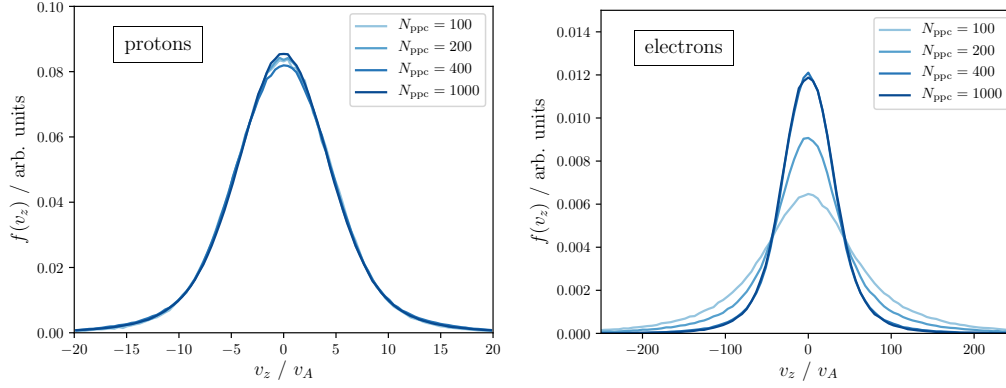
FIGURE 41: Downstream velocity distributions, $f(v_z)$, for protons and electrons for various numbers of proton simulation particles per cell. If this number is not big enough ($N_{\mathrm{ppc}} < 400$) the noise in the electromagnetic fields from the hybrid simulations will lead to an artificial heating of the test-particle electrons, resulting in pronounced nonthermal tails.

The test-particle electrons are injected from the right boundary[31], i.e., from far upstream. We have investigated three different initial electron distributions: (i) a test-electron population that is injected with a mean velocity equal to the upstream plasma flow velocity $\vec{v}_{0,e} = \vec{v}_0$; (ii) a "beam distribution" with a mean velocity of the test-electron population of $v_{0,e} = 100\, v_A \gg v_0$ directed parallel to the bulk velocity of the ions; (iii) a "shell distribution" with an suprathermal velocity $v_{0,e} = 100\, v_A \gg v_0$. If not stated otherwise, in the following we will mainly discuss results obtained for the first distribution, (i). The particles are injected starting at $t = 0\,\omega_c^{-1}$ if $\vec{v}_{0,e} = \vec{v}_0$ and at $t = 50\,\omega_c^{-1}$ otherwise, which assures that the first particles reach the shock well after it has formed. For the first two cases, (i) and (ii), the test-particle electron population is initialized with the same upstream temperature as the electron fluid. It is important to note here that, since the thermal velocity of the electrons is larger or comparable to $|v_{0,e}|$, the electrons have to be initialized with a distribution according to the flux of a drifting Maxwellian (see Sec. 3.3 for details).

6.3 Results

In our simulations, we followed the shock evolution over several hundred proton cyclotron times. Since the setup of the simulation does not differ from the one presented in Chapter 4, except for the additional inclusion of electron test-particles, we do not show the resulting magnetic fields again but rather refer to the field configuration depicted in Fig. 14. As stated before, streaming ions excite circularly polarized Alfvén waves in the upstream via resonant or non-resonant instabilities, see Sec. 2.3.4. This turbulence from the hybrid simulations serves as input for the propagation of the electron test-particles.

Valuable information about particle energization and thermalization can be gained from the phase space distribution, depicted in Fig. 42 for protons and electrons. Note that while for the protons the phase space plane (x, v_x) is shown, we plot $f_e(x, v_\parallel)$ for

---
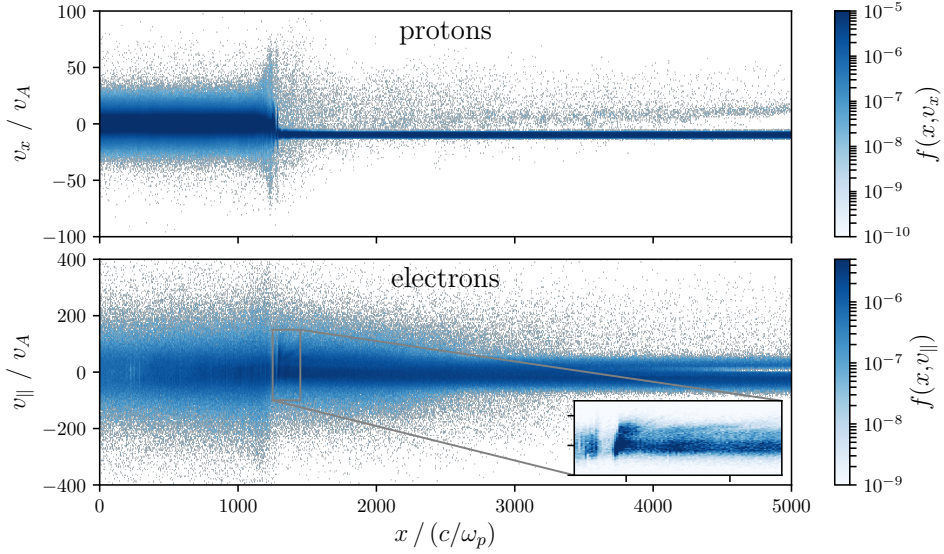
[31] See Fig. 11 for a sketch of the simulation setup.

FIGURE 42: (top) Proton phase space distribution, f_p, in the (x, v_x)-plane at $t = 400\,\omega_c^{-1}$ for a simulation with a upstream bulk velocity of $v_0 = 10\,v_A$. (bottom) Phase space distribution of test-particle electrons $f_e(x, v_\parallel)$. The inset shows the phase space around the shock transition using a linear color scale. There a reflection of electrons is visible.

the test-particle electrons. Here $v_\parallel$ denotes the velocity along the local (background plus turbulent) magnetic field, therefore,

$$v_\parallel(t) = \vec{v}(t) \cdot \frac{\vec{B}(x, t)}{\left|\vec{B}(x, t)\right|}. \tag{101}$$

In the proton phase space, the transition from the cold upstream to the hot downstream plasma is clearly visible. Additionally to the thermal population nonthermal particles are present in the upstream and downstream media. The distribution of electrons spans over a larger range of velocities because the mass of the test-particle electrons is much smaller than the proton mass, yielding a larger thermal velocity. In the upstream, a population of electrons with positive $v_\parallel$ can be observed in addition to the bulk electrons, moving towards the shock with negative $v_\parallel$. This indicates a reflection of particles near the shock transition. In the inset in Fig. 42 a reflection of test-particle electrons at the shock front, presumably due to magnetic mirroring, becomes apparent. Furthermore, an increase in the width of the velocity distribution can be observed as the shock front is approached from the upstream, which indicates a heating of the test-particles. In contrast to protons for which a considerable increase in the temperature is expected upon the shock transition, the width of the electron velocity distribution shows only a minor increase, which suggests only small changes in the temperature.

To confirm the reflection of test-particle electrons at the shock front, inferred from the phase space plot in Fig. 42, the analysis of trajectories of some test-particles provides a useful tool. We have saved trajectories of some test-electrons, which reside in the upstream in front of the shock at $t = 275\,\omega_c^{-1}$ and end up in the upstream at $t = 300\,\omega_c^{-1}$, to confirm the reflection and to see the processes at the shock front in more detail. A small number
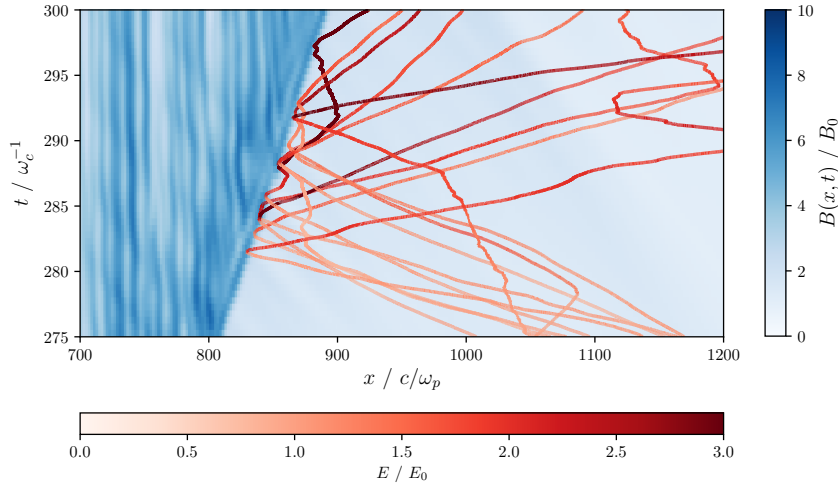
Figure 43: The red lines denote trajectories of reflected test-particle electrons in the (x, t)-plane. The color encodes their energy in terms of the initial energy at $t = 275\,\omega_c^{-1}$. In the background the magnitude of the magnetic field is shown. Electrons are reflected from the increasing magnetic field at the shock. During the reflection an energy gain can be observed.

of trajectories are shown in Fig. 43 in red (the shade encodes the energy in terms of the electron's initial energy at $t = 275\,\omega_c^{-1}$). In the background the magnitude of the magnetic field is plotted as function of spatial coordinate and time. The trajectories evidence that test-electrons are reflected at the shock front, presumably by magnetic mirroring. Additionally, one can observe an increase of the particle energy during the reflection. Hence, this process might be important for the injection of electrons into the DSA. Note that the idea of the electron acceleration by mirror reflection and trapping in the ion-scale turbulence in quasi-parallel shocks has been put forward two decades ago by G. Mann & H.-T. Claßen, see, e.g., [194, 195].

To see whether accelerated electrons have been generated at all and to investigate the electron heating upon shock crossing, we take a closer look at the downstream velocity distribution of the test-particles. We plot $f(v_\parallel)$ at $t = 400\,\omega_c^{-1}$ in Fig. 44. Note that these test-particle electrons correspond to a low density addition to the core electron distribution which is accounted for by the fluid description in the hybrid model. The center of the velocity distribution is well described by a Maxwellian with $T = 5.6\,T_0$, see the dashed blue line. As we will show later, this temperature is significantly higher than the temperature of the electron fluid. At larger $|v_\parallel|$ an additional nonthermal component is apparent. While this could indicate electron acceleration and injection, we do not observe the formation of a clear power-law tail in the energy spectrum (see also Fig. 46). Rather, the velocity distribution including the suprathermal particles is well described by the so-called Kappa (κ-) distribution. This class of distribution functions is frequently used to describe collisionless plasmas out of equilibrium. Common applications are space and astrophysical plasmas from solar wind and planetary magnetospheres to the heliosheath, and beyond to interstellar and intergalactic plasmas [180, 196, 197, 198, 199, 200]. The
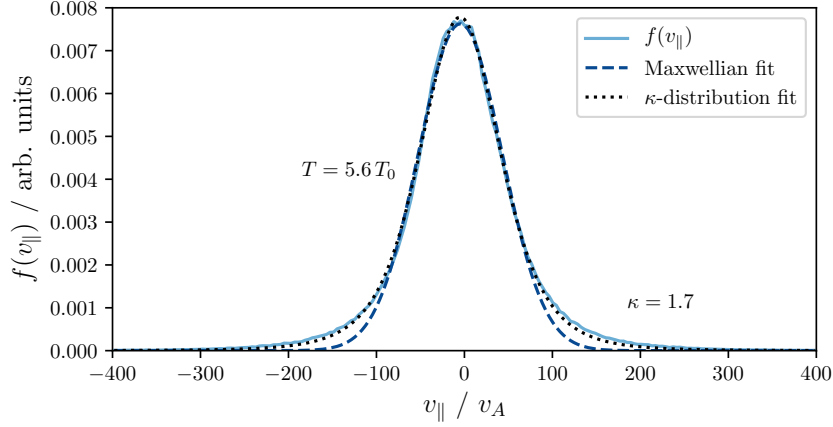
FIGURE 44: Downstream velocity distribution, $f(v_\parallel)$, of test-electrons at $t = 400\omega_c^{-1}$ for a simulation initialized with an upstream bulk velocity of $v_0 = 10\,v_A$. While the center of the distribution resembles a Maxwellian, the tails at higher $v_\parallel$ are better described by a κ-distribution.

distribution function reads

$$f_\kappa(v) \propto (\kappa w_\kappa^2)^{-\frac{3}{2}} \frac{\Gamma(\kappa+1)}{\Gamma(\kappa-1/2)} \left(1 + \frac{v^2}{\kappa w_\kappa^2}\right)^{-(\kappa+1)}, \tag{102}$$

where $w_\kappa = \sqrt{(2\kappa - 3)k_B T / \kappa m}$, is a characteristic velocity, corresponding to the thermal velocity in a Maxwellian distribution, m and T are the particle's mass and temperature, and $\Gamma(x)$ denotes the Gamma function. The fitted κ-distribution, see black dotted line in Fig. 44, agrees well with the measured downstream velocity distribution over the whole range of $v_\parallel$. Note that in the limit of $\kappa \to \infty$ the Kappa-distribution becomes a Maxwellian. In our case the value $\kappa = 1.7$ is obtained from the fit, which is close to the critical value of $\kappa_{\mathrm{crit}} = 1.5$, indicating a considerable non-Maxwellian tail.

Comparing the velocity distribution of the test-particles with the electron fluid, one finds a considerable difference in the tail/core content. The test-particle distribution has not only a higher temperature than the adiabatic heating prescribed for the electron fluid but also exhibits nonthermal tails. Using the expected thermal velocity for the electron fluid in the downstream, $v_{\mathrm{th,d}}^e$, as a reference, we calculate the ratio $f(5\,v_{\mathrm{th,d}}^e)/f(0)$, i.e., the ratio of the velocity distribution measured in the tail at $5\,v_{\mathrm{th,d}}^e \approx 150\,v_A$ and in the center. This ratio is more than 5000 times larger for the test-electrons than for the electron fluid ($f^{\mathrm{TP}}(5\,v_{\mathrm{th,d}}^e)/f^{\mathrm{TP}}(0) \simeq 0.05$ vs. $f^{\mathrm{fluid}}(5\,v_{\mathrm{th,d}}^e)/f^{\mathrm{fluid}}(0) \simeq 9 \cdot 10^{-6}$).

Spatially resolved temperature profiles of protons, test-particle electrons and electron fluid are plotted in Fig. 45. The proton temperature remains constant throughout the upstream and only directly in front of the shock a heating of ions in the precursor is visible. Upon shock crossing the protons are heated strongly as the velocities are randomized by the turbulent fields and a large part of the bulk kinetic energy is converted into thermal energy. The comparison of the temperatures of the fluid and the test-particle electrons reveals differences in the upstream as well as in the downstream medium. As the ion density remains constant in the upstream, also the temperature of the electron fluid is

constant since an adiabatic equation of state, see Eq. (48), is assumed. The test-electrons on the other hand show a gradual increase of the temperature towards the shock front in the region $1300\,c/\omega_p \leq x \leq 2600\,c/\omega_p$, indicating a considerable heating in the shock precursor. The downstream temperature of the test-particle electrons is approximately two times larger than the fluid temperature[32].
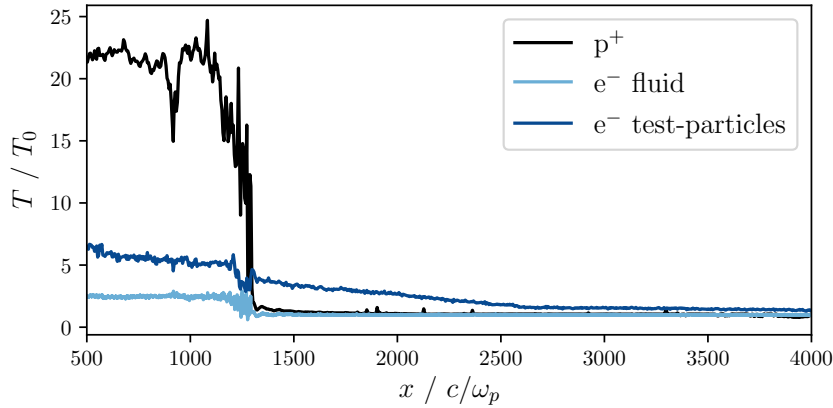

FIGURE 45: Spatially resolved temperatures of protons, electron test-particles and electron fluid. The temperatures of simulation and test-particles are determined by fitting Maxwellian distributions, while the fluid temperature is given by the adiabatic equation of state, Eq. (48), which is used to model the electron pressure. For test-particle electrons a heating in the shock precursor can be observed.

For completeness, some results for the different initial test-electron distributions (ii) and (iii) are compiled in Fig. 46. The injection of suprathermal electrons in form of a beam or shell distribution results in a larger width of $f(v_\parallel)$ and a shift of the maximum of $f(v_\perp)$. As expected, the downstream temperature will be higher for these particles. The downstream velocity distributions for the suprathermal test-electrons are similar despite of the difference of the initial distributions. A peculiarity is the flatness of $f(v_\parallel)$ at small $v_\parallel$, which is more pronounced for smaller proton upstream bulk velocities. The energy spectra, shown in the right panels of Fig. 46 for different proton upstream bulk velocities, do not exhibit signs of a power law.

Besides numerical simulations, remote observations can help to understand the electron thermalization at collisionless shocks. Observations of Balmer-dominated shocks do not point towards an equilibration of electron and ion temperatures directly behind the shock but rather obtain an electron-ion temperature ratio which decreases with shock velocity. To analyze the dependence of the electron-to-proton temperature ratio, we have performed parametric simulations for various upstream bulk velocities and calculated the temperature of protons and test-particle electrons in the downstream by fitting a Maxwellian to the velocity distribution. We compute the velocity distributions at $t > 150\,\omega_c^{-1}$, well after the shock has developed. At this time a prominent power-law DSA tail in the proton distribution has not yet developed, but protons are already energized and drive circularly

---

[32]   The answer of the puzzling question, which of the two temperature profiles resembles reality best, could be probably determined by fully kinetic PIC simulations, which, however, are computationally very demanding.
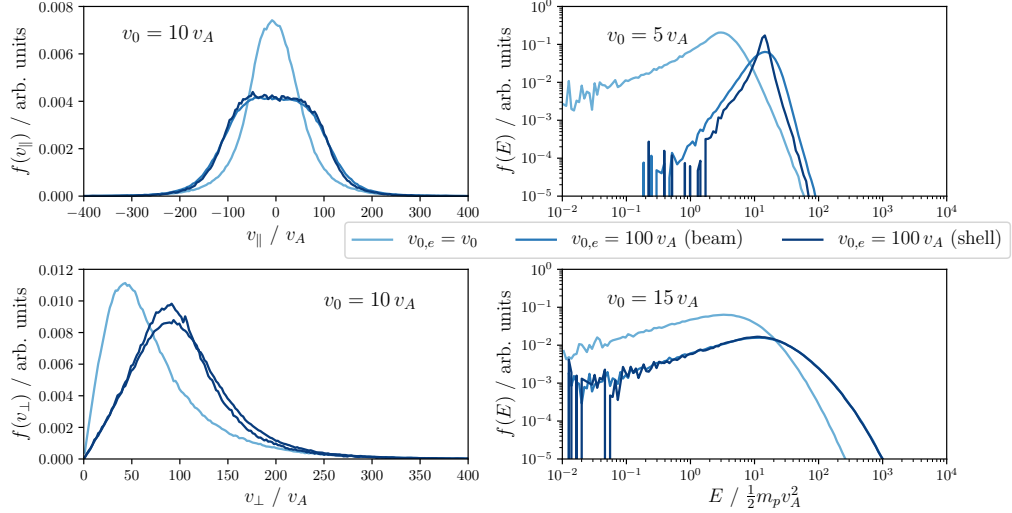
FIGURE 46: (left) Downstream velocity distributions, $f(v_\parallel)$ and $f(v_\perp)$, at $t = 300\,\omega_c^{-1}$ for different initial test-electron populations. (right) Downstream energy spectra for different proton upstream bulk velocities and initial test-electron distributions. While the injection of suprathermal electrons results in a shift of the spectrum towards higher energies, a formation of power-law tails could not be observed.

polarized Alfvén waves in the upstream. Figure 47 depicts the resulting temperature ratio as function of the Alfvénic shock Mach number (blue diamonds). Additionally, we show the temperature ratio inferred from the observation of the Hα lines at Balmer-dominated shocks, using data from [33, 201, 202][33]. Both, the observations as well as the results from the simulation indicate that the electron-ion temperature ratio decreases with increasing shock velocity or Mach number, respectively. Especially the in the observations T_e/T_i seems to saturate (or even increase again) at high shock velocities. The authors of [33] found a functional dependence $T_e/T_i \sim v_{\rm sh}^{-2}$ to fit best to the observational data (red dashed line in Fig. 47). Our simulation results are better described by $T_e/T_i \sim M^{-1}$ (blue dashed line). This behavior has been reported for the electron-ion temperature ratio at the terrestrial bow shock and interplanetary shocks [203]. The scaling observed in our simulations may be partially attributed to the fact that our numerical model treats only the nonrelativistic injection phase and all particles are subrelativistic. It is worth noting that we have to assume a relatively high Alfvén velocity of $v_A = 90$ km/s for a direct comparison of the temperature ratio extracted from the simulation with the observational data. This is about four times higher than the value of $v_A = 20$ km/s for typical parameters of the interstellar medium (ISM) of $n = 0.1\,{\rm cm}^{-3}$ and $B = 3\,\mu{\rm G}$. However, since the exact parameters in the SNR environment are not known, and it is arguable whether one has to consider the Alfvén velocity in the amplified field, which can reach values of $\delta B/B = 4-10$ [33], this comparison is still meaningful.

---

[33] Note that in this case the temperature ratio is given as function of the shock velocity, $v_{\rm sh}$, since a direct measurement of the conditions in the SNR environment is difficult, which prevents a determination of shock Mach numbers.
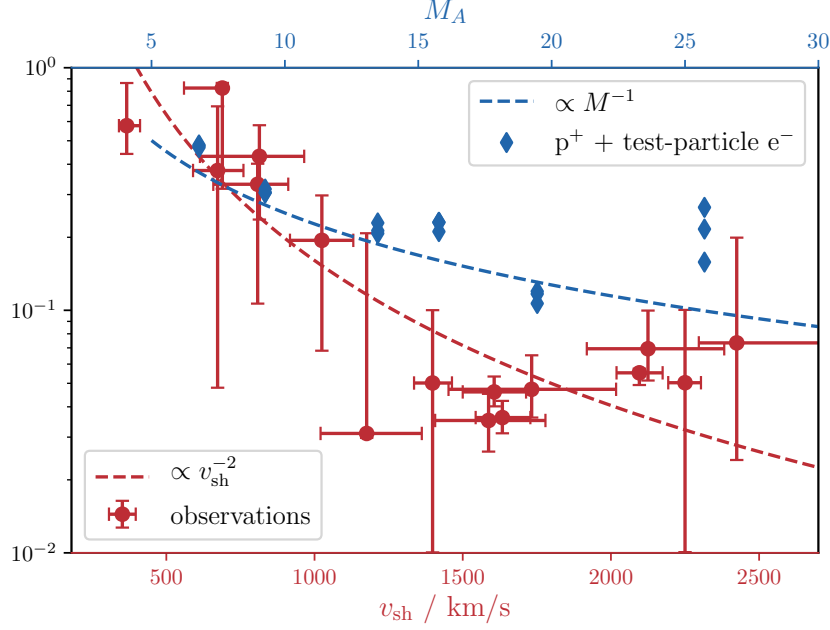
FIGURE 47: Electron-to-proton temperature ratio, T_e/T_i, extracted from the simulations (blue diamonds) compared to the temperature ratio determined from observations of Balmer-dominated shocks (red dots, data from [33, 201, 202]). The simulation results are calculated at three different times, resulting in a small spread of the data points.

6.4 Discussion

The temperature ratios obtained from observations of Balmer-dominated shocks as well as our simulation results point towards a decrease of the electron-ion temperature ratio with increasing shock velocity. Hence, an equilibration of electron and ion temperatures can only be expected at low Mach number shocks. At high Mach number shocks, on the other hand, a saturation or even upturn of the temperature ratio has been measured. The saturation level, however, does not coincide with the mass proportional heating predicted by the Rankine-Hugoniot conditions, see Eq. (13), but takes place at a higher level. The observed scaling of T_e/T_i with the inverse square of the shock velocity has been recently supported by theoretical modeling. Vink *et al.* have considered the Rankine-Hugoniot jump conditions with the assumption of separate enthalpy flux conservation for each particle species and found $T_e/T_i \sim M_s^{-2}$, where $M_s = v_{\rm sh}/c_s$ is the sonic Mach number [204]. This behavior is, however, limited to a certain range of Mach numbers, see Eq. (14) in [204],

$$\sqrt{\frac{2}{\gamma-1}\frac{\mu}{m_i}\frac{r^2}{r^2-1}} < M_s < \sqrt{\frac{2}{\gamma-1}\frac{\mu}{m_e}\frac{r^2}{r^2-1}}, \tag{103}$$

where $\mu = (m_i + m_e)/2$ denotes the average mass, γ is the adiabatic index, and r is the shock compression ratio. For our simulation parameters, including the increased electron-ion mass ratio, this translates to a predicted $T_e/T_i \sim M_A^{-2}$ behavior in the range $1.4 < M_A < 23$. Note that we have transformed Eq. (103) to a range of Alfvénic Mach numbers to allow for comparison with the simulation results. In agreement with the observations, the

theoretical work by Vink *et al.* also predicts a saturation of the electron-ion temperature ratio on a level above the mass proportional heating for high M_s in the case of efficient CR acceleration, i.e., when the pressure of cosmic rays in the precursor cannot be neglected. It is also worth noting that Eq. (103) should also have an impact on the interpretation of the results of fully kinetic simulations, since the electron and ion masses influence the range of shock Mach numbers in which the $T_e/T_i \sim M_s^{-2}$ scaling can be observed. For fully kinetic simulations of collisionless shocks which routinely use an artificially increased electron-to-proton mass ratios of $m_p/m_e = 64 - 100$, see, e.g., [95], this range is drastically reduced.

The investigation of electron energization by the electromagnetic fields generated in hybrid simulations implies the existence of independent preheating mechanisms for this electron population. Indeed, hybrid simulations treat electrons as a fluid so that they can interact with relatively long waves generated by nonequilibrium ion populations (such as shock-reflected ions) within the hybrid simulations only adiabatically. These waves cannot heat the electrons appreciably. However, these are not the only waves generated by such ions in *real shocks*. Much shorter waves with higher frequencies, not accessible to hybrid simulations, may also be generated. They can tap into thermal electrons and preheat them. Then, electrons start interacting with the waves generated in the hybrid simulations. The preheating mechanisms are not straightforward, and their thorough description is outside of the scope of this thesis[34]. Almost universally, such mechanisms invoke a combination of Cherenkov and cyclotron resonances impacting the same particle populations. Potential preheating mechanisms have already been considered in the context of magnetic fusion research and general plasma physics, e.g., [205], but also in conjunction with the electron injection into the diffusive shock acceleration [206].

The cause of the observed relation between temperature ratio and shock velocity/Mach number remains an open question and the mechanism responsible for the electron heating is also far from being fully understood. The adiabatic heating, usually employed in hybrid models to describe the temperature of the electron fluid, results in a inverse squared dependence of the temperature ratio on the shock velocity. This is due to the fact that the compression ratio depends only weakly on the shock Mach number for strong shocks with $M \gg 1$, while the ion temperature increases with M^2. However, the test-particle calculations show that the adiabatic heating does not account for a possible heating of the electrons in the shock precursor. This might be an important feature as the $T_e/T_i \propto v_{\mathrm{sh}}^{-2}$ behavior also has been attributed to electron heating in the shock precursor [201]. Additionally, the length of the precursor established by the accelerated ions could influence the heating. It was speculated in [207] that, as the precursor length depends on the shock velocity, the electron temperature should rise with increasing shock speed, allowing for a saturation of the temperature ratio at high shock velocities.

For the heating of electrons in front of SNR shocks different models have been proposed. As *in situ* observations at SNR shocks are not possible, one cannot draw direct conclusions from particle distributions in these environments, but has to rely on modeling and

---

[34] More details on possible preheating mechanisms can be found in [212].

numerical simulations. In the past mainly two scenarios have been proposed to describe electron heating at nonrelativistic collisionless shocks. A heating in the precursor due to the interaction with lower hybrid waves was proposed in [208], while counterstreaming instabilities in front of the shock were suggested to be responsible in [209]. Both mechanisms were introduced in the context of perpendicular shocks. One can, however, argue that these models are also applicable to quasi-parallel shocks if the turbulent magnetic field ahead of the shock is amplified to values on the order of the background field or even above this level [210, 211].

6.5 SUMMARY

This part of the thesis has been devoted to some aspects of the notoriously difficult problem of electron injection into the DSA. By introducing electrons as test-particles that move in the fields generated by the ion component, we investigated the acceleration and thermalization of electrons at quasi-parallel shocks.

We have observed the reflection of a considerable fraction of electrons at the shock front due to magnetic mirroring. We have found the development of nonthermal tails in the downstream velocity distribution, which can be described by κ-distributions. However, in contrast to the ion population, which exhibits the formation of prominent power-law tails in the downstream energy spectra, we could not detect the formation of such power-law tails for electron test-particles (even when considering a population of already initially suprathermal test-electrons). The comparison of the spatially resolved temperatures of test-electrons and electron fluid has revealed some differences. In the upstream a heating of the test-particles in the precursor has been observed, which is obviously absent for the electron fluid. Additionally, for a simulation with $v_0 = 10\,v_A$, the downstream temperature of the test-particles is about two times higher than the temperature of the adiabatically heated electron fluid.

By analyzing the downstream temperature for different shock velocities, we have confirmed a decreasing electron-to-ion temperature ratio with increasing shock velocity, deduced earlier from observations of Balmer-dominated shocks [201, 202, 33] and predicted theoretically [204]. The different scaling of the temperature ratio obtained in our simulations might be attributed to the fact that we only investigate the subrelativistic initial phase of particle acceleration.

The investigations on this topic [212] are still ongoing and some aspects remain open for future studies. A clarification of the exact behavior of the electron temperature could be possible with the help of fully kinetic PIC simulations, which are computationally demanding but manageable in reduced dimensionality. In this context attention has to be paid to the prescribed electron-ion mass ratio. With the input from these simulations an improved model for the temperature of the electron fluid might be developed. Additional information, which might help extending the understanding of the electron dynamics at quasi-parallel shocks, can be gained from the analysis of experimental observations of electron acceleration and heating at shocks in the solar system, see, e.g., [213], even if these shocks are smaller and weaker than SNR shocks that are responsible for CR production.

CHAPTER 7

Conclusion and Outlook

In this thesis we have used the hybrid model presented in Chapter 3 to perform extensive numerical simulations of ion acceleration at collisionless shocks with the goal of improving the understanding of the initial phase of cosmic ray (CR) acceleration, the so-called "injection". The hybrid method is well suited for the problem of ion acceleration at shocks as the ion scales are resolved and ion kinetic effects are included. In our one- and two-dimensional simulations we have observed the development of power-law tails in the downstream energy spectra as predicted by the theory of diffusive shock acceleration (DSA). By comparing data from recent high-precision observations with results extracted from the simulations we were able to enlighten some features of the complicated process of particle injection into the DSA.

First, in Chapter 4 we have investigated the injection of different ion species into the DSA. Our results have shown that the self-consistent inclusion of helium ions is crucial. These ions, while relatively small in number, drive waves, enriching the spectrum especially at low wavenumbers, which is important for resonant wave-particle interactions. We have shown that the injection rate of different elements into the DSA is a function of the mass-to-charge ratio (A/Z). However, in contrast to the strictly linear growth of the injection rate with mass-to-charge ratio reported in [156], we have observed that the injection first increases, then saturates (in a Mach dependent fashion) and afterwards decreases with A/Z. Furthermore, we have proven the earlier theoretical predictions [102] that the injection also depends on the shock Mach number, M. We calculated time integrated rigidity spectra by combining the injection efficiency obtained in our simulations, which treated both, protons and helium ions self-consistently, with theoretical DSA rigidity spectra and the shock evolution during the Sedov-Taylor phase. In this way we extended the spectra to rigidities beyond the possibilities of any simulation. The extracted dependence of the proton-to-helium ratio is in excellent agreement with the recent precise measurements [5, 7] for rigidities above 10 GV. This result indicates that the observed ≈ 0.1 difference in the spectral indices of protons and helium (and also carbon and oxygen) is an intrinsic feature of the acceleration process, caused by the A/Z dependence of the initial acceleration phase. No additional assumptions, such as environmental factors or multi-supernova remnant (SNR) scenarios, have to be made for the explanation of the "anomaly".

We have analyzed the trajectories of accelerated particles and found indications of the scatter-free acceleration process proposed by Sugiyama *et al.* [157, 158], which is based on nonlinear wave-particle interaction. This process would probably provide a good starting point for building an injection model which is highly desirable but beyond the scope of this thesis. A model for particle injection into the DSA could be developed in the future with the help of results from hybrid simulations. This is a very demanding task as this model should correctly determine the injection as function of shock Mach number, particle

species, and shock inclination.

In Chapter 5 we have investigated the influence of the variation of the magnetic field direction across the shock front on the slope of CR energy spectra. As expected, particle injection and acceleration are mainly limited to regions where the shock is quasi-parallel. Due to diffusion of energetic particles into regions where the shock is quasi-perpendicular, a fraction of particles get lost from the acceleration process. This results in a steepening of the power-law tail by $\Delta q = 0.1 - 0.15$ (likely to be scalable to larger boxes and longer simulation time so that larger Δq values are expected for realistic SNR conditions) compared to the spectrum of energetic protons accelerated at a quasi-parallel shock. This explains the observed difference of the measured spectral slope compared to the DSA prediction at least in the low energy regime. At higher energies, other mechanisms (see, e.g., [173, 174]) might be more relevant for the difference in the spectral indices. A further step would be to answer the question, how an additional minor population of helium ions alters the results. A scan of the injection as function of the shock obliquity revealed that an additional He^{2+} population slightly alters the obliquity dependence of the injection of protons. This aspect is interesting and computationally very demanding, but might be resolved in future investigations.

Finally, in Chapter 6 we have investigated the behavior of test-particle electrons in the proton-driven turbulence obtained from hybrid simulations. While we have not observed a development of a power-law tail for the test-electrons, which has been found for electrons in fully kinetic particle-in-cell (PIC) simulations of quasi-parallel collisionless shocks [95], we have detected nonthermal tails in the downstream velocity distributions of the test-particle population. Our simulations show a heating of the test-particle electrons in the shock precursor, which also has been proposed in [201] to explain the observational data of Balmer-dominated shocks. By performing parametric simulations for various shock Mach numbers, we calculated the electron-ion temperature ratio as function of M. The temperature ratio obtained from the simulations decreases with shock Mach number. A similar behavior of the electron-to-proton temperature ratio was reported recently for Balmer-dominated shocks [33]. In this context an interesting approach would be an improvement of the description of the electron fluid with input from fully kinetic PIC simulations. This might allow for a more realistic modeling of the electron pressure.

The results of this thesis clearly demonstrate that hybrid simulations provide a valuable tool for understanding the process of ion acceleration at collisionless shocks, especially the complicated problem of ion injection into the DSA. This is of particular interest nowadays as the precise measurements of CR spectra reveal new features that are not accounted for by the standard DSA theory. The results from simulations can help to determine the origin of some of these features and shed light on different aspects of the acceleration process.

A huge step forward would be the development of a complete injection model as mentioned above. While theoretical considerations have already lead to constructive approaches [101, 102, 158, 97], hybrid simulations can help to refine these models. Additionally, hybrid simulations of shocks with inhomogeneities in the upstream density can give

insights into the processes that occur at SNR shocks propagating into inhomogeneous or clumpy medium. Large scale magnetohydrodynamic simulations of SNR shocks in these environments have already revealed implications for magnetic field amplification [214, 215] as well as for the estimation of the CR production efficiency [216]. Modeling of collisionelss shocks propagating into partially ionized medium might be another interesting application for the hybrid model. This would require an extension of the model to account for charge exchange processes. Hybrid simulations of perpendicular shocks in partially ionized plasmas have already been performed, and a rapid acceleration to high energies as well as magnetic field amplification have been observed [217, 179, 218], which are typically absent in hybrid simulations of perpendicular shocks in fully ionized plasmas. Hybrid simulations of quasi-parallel shocks in partially ionized medium might also reveal some interesting features partly related to the influence of a neutral-induced precursor [219]. So, hybrid simulations will continue to contribute to the understanding of the captivating problem of CR acceleration and origin together with continuously improving observations and theory.

CHAPTER A

Appendix

The Hybrid Model in Dimensionless Variables

The equations of motion in terms of the dimensionless variables introduced in Sec. 3.2 read

$$\frac{d\vec{\tilde{v}}}{d\tilde{t}} = \frac{Z}{A}\left(\vec{\tilde{E}} + \vec{\tilde{v}} \times \vec{\tilde{B}}\right),\tag{104}$$

$$\frac{d\vec{\tilde{x}}}{d\tilde{t}} = \vec{\tilde{v}}.\tag{105}$$

Here Z and A denote the charge number and mass number, respectively. The equation for the dimensionless electric field, calculated from the momentum equation of the electron fluid, can be written as

$$\vec{\tilde{E}} = \frac{1}{\tilde{n}}\left(\left(\vec{\tilde{J}} - \vec{\tilde{J}_i}\right) \times \vec{\tilde{B}} - \frac{1}{2}\tilde{\nabla}\tilde{p}_e\right) + \tilde{\eta}\,\vec{\tilde{J}}.\tag{106}$$

Faraday's law can be expressed in the dimensionless variables as

$$\frac{d\vec{\tilde{B}}}{d\tilde{t}} = -\tilde{\nabla} \times \vec{\tilde{E}},\tag{107}$$

and Ampere's law in the Darwin approximation reads, correspondingly,

$$\vec{\tilde{J}} = \tilde{\nabla} \times \vec{\tilde{B}}.\tag{108}$$

In the following the tilde-sign for the dimensionless quantities will be omitted.

Discretized Equations for the Calculations of the Fields

In contrast to electromagnetic particle-in-cell (PIC) codes where the field are often calculated and stored on a staggered grid (Yee lattice) we use an unstaggered grid for saving the ion density as well as for calculating the electromagnetic fields. This allows for a faster interpolation of the fields to the particle position. Central second-order finite difference stencils are used to calculate the spatial derivatives,

$$(\partial_x A)_{(i,j)} = \frac{A_{(i+1,j)} - A_{(i-1,j)}}{2\Delta x}.\tag{109}$$

Here A is some quantity stored on the numerical grid, (i, j) denote the grid point index in x- and y-direction, and Δx is the grid spacing in x-direction.

The calculation of the electron pressure term in the equation of the electric field,

Eq. ([75]), can be written in discretized form as

$$
(\nabla\, p_e)_{(i,j)} = (\nabla\, n_i^{\gamma})_{(i,j)} = \gamma\, n_{i,(i,j)}^{\gamma-1}
\begin{pmatrix}
\dfrac{n_{i,(i+1,j)} - n_{i,(i-1,j)}}{2\Delta x} \\[2mm]
\dfrac{n_{i,(i,j+1)} - n_{i,(i,j-1)}}{2\Delta y} \\[2mm]
0
\end{pmatrix}. \tag{110}
$$

The current density is calculated as the curl of the magnetic field. Discretization of the spatial derivatives in the two-dimensional case yields

$$
\vec{J}_{(i,j)} = \left(\nabla \times \vec{B}\right)_{(i,j)} =
\begin{pmatrix}
\dfrac{B_{z,(i,j+1)} - B_{z,(i,j-1)}}{2\Delta y} \\[2mm]
-\dfrac{B_{z,(i+1,j)} - B_{z,(i-1,j)}}{2\Delta x} \\[2mm]
\dfrac{B_{y,(i+1,j)} - B_{y,(i-1,j)}}{2\Delta x} - \dfrac{B_{x,(i,j+1)} - B_{x,(i,j-1)}}{2\Delta y}
\end{pmatrix}. \tag{111}
$$

Similar, the curl of the electric field is calculated in order to update the magnetic field,

$$
\left(\partial_t \vec{B}\right)_{(i,j)} = -\left(\nabla \times \vec{E}\right)_{(i,j)} = -
\begin{pmatrix}
\dfrac{E_{z,(i,j+1)} - E_{z,(i,j-1)}}{2\Delta y} \\[2mm]
-\dfrac{E_{z,(i+1,j)} - E_{z,(i-1,j)}}{2\Delta x} \\[2mm]
\dfrac{E_{y,(i+1,j)} - E_{y,(i-1,j)}}{2\Delta x} - \dfrac{E_{x,(i,j+1)} - E_{x,(i,j-1)}}{2\Delta y}
\end{pmatrix}. \tag{112}
$$

The use of an unstaggered grid together with central difference stencils for the spatial derivatives nevertheless assures $\nabla \cdot \vec{B} = 0$, which can be shown by calculating

$$
\begin{aligned}
\left(\nabla\, \partial_t \vec{B}\right)_{(i,j)} &= -\frac{\left(E_{z,(i+1,j+1)} - E_{z,(i+1,j-1)}\right) - \left(E_{z,(i-1,j+1)} - E_{z,(i-1,j-1)}\right)}{4\Delta x \Delta y} \\[2mm]
&\quad + \frac{\left(E_{z,(i+1,j+1)} - E_{z,(i-1,j+1)}\right) - \left(E_{z,(i+1,j-1)} - E_{z,(i-1,j-1)}\right)}{4\Delta x \Delta y} \\[2mm]
&= 0.
\end{aligned} \tag{113}
$$

Hence, if the magnetic field fulfills $\nabla \cdot \vec{B} = 0$ at $t = 0$, it will be fulfilled at every time step up to numerical accuracy.

The Runge-Kutta Algorithm for Updating the Magnetic Field

In the two-dimensional code a Bashford-Adams extrapolation is employed by default to obtain the ion current density at integer time steps. In this case a fourth-order Runge-Kutta algorithm is used to update the magnetic field according to Faraday's law, Eq. ([107]). The electric field appearing in this equation is calculated from Eq. ([106]) and is a function of $n_i, \vec{J}_i$ and $\vec{B}$. After discretization in time and using the notation $\vec{E}^n = E(n\,\Delta t)$, one

can write

$$\vec{E}^n = \vec{E}(n_i^n, \vec{J}_i^n, \vec{B}^n). \tag{114}$$

Finally, the fourth-order Runge-Kutta algorithm reads

$$\vec{B}^{n+1} = \vec{B}^n + \frac{\Delta t}{6} \left(\vec{K}_1 + \vec{K}_2 + \vec{K}_3 + \vec{K}_4 \right), \tag{115}$$

with

$$\vec{K}_1 = -\nabla \times \vec{E}(n_i, \vec{J}_i, \vec{B}^n), \tag{116}$$

$$\vec{K}_2 = -\nabla \times \vec{E}(n_i, \vec{J}_i, \vec{B}^n + \frac{\Delta t}{2} \vec{K}_1), \tag{117}$$

$$\vec{K}_3 = -\nabla \times \vec{E}(n_i, \vec{J}_i, \vec{B}^n + \frac{\Delta t}{2} \vec{K}_2), \tag{118}$$

$$\vec{K}_4 = -\nabla \times \vec{E}(n_i, \vec{J}_i, \vec{B}^n + \Delta t \, \vec{K}_3). \tag{119}$$

REFERENCES

[1] Hess, V. F. Über Beobachtungen der durchdringenden Strahlung bei sieben Freiballonfahrten. *Phys. Z.* **13**, 1084–1091 (1912).

[2] Yoon, Y. S. *et al.* Cosmic-ray Proton and Helium Spectra from the First CREAM Flight. *Astrophys. J.* **728**, 122 (2011).

[3] Abe, K. *et al.* Measurements of Cosmic-Ray Proton and Helium Spectra from the BESS-Polar Long-duration Balloon Flights over Antarctica. *The Astrophysical Journal* **822**, 65 (2016).

[4] Murphy, R. P. *et al.* Galactic Cosmic Ray Origins and OB Associations: Evidence from SuperTIGER Observations of Elements 26Fe through 40Zr. *The Astrophysical Journal* **831**, 148 (2016).

[5] Adriani, O. *et al.* PAMELA Measurements of Cosmic-Ray Proton and Helium Spectra. *Science* **332**, 69–72 (2011).

[6] Battiston, R. The antimatter spectrometer (AMS-02): A particle physics detector in space. *Nuclear Instruments and Methods in Physics Research Section A: Accelerators, Spectrometers, Detectors and Associated Equipment* **588**, 227 – 234 (2008). Proceedings of the First International Conference on Astroparticle Physics.

[7] Aguilar, M. *et al.* Precision Measurement of the Helium Flux in Primary Cosmic Rays of Rigidities 1.9 GV to 3 TV with the Alpha Magnetic Spectrometer on the International Space Station. *Phys. Rev. Lett.* **115**, 211101 (2015).

[8] Aguilar, M. *et al.* Observation of the Identical Rigidity Dependence of He, C, and O Cosmic Rays at High Rigidities by the Alpha Magnetic Spectrometer on the International Space Station. *Phys. Rev. Lett.* **119**, 251101 (2017).

[9] Aguilar, M. *et al.* Observation of New Properties of Secondary Cosmic Rays Lithium, Beryllium, and Boron by the Alpha Magnetic Spectrometer on the International Space Station. *Phys. Rev. Lett.* **120**, 021101 (2018).

[10] Kampert, K.-H. & Unger, M. Measurements of the cosmic ray composition with air shower experiments. *Astroparticle Physics* **35**, 660 – 678 (2012).

[11] Aab, A. *et al.* Inferences on mass composition and tests of hadronic interactions from 0.3 to 100 EeV using the water-Cherenkov detectors of the Pierre Auger Observatory. *Phys. Rev. D* **96**, 122003 (2017).

[12] Mészáros, P., Fox, D. B., Hanna, C. & Murase, K. Multi-messenger astrophysics. *Nature Reviews Physics* **1**, 585–599 (2019).

REFERENCES

[13] Aartsen, M. *et al.* Multimessenger observations of a flaring blazar coincident with high-energy neutrino IceCube-170922A. *Science* **361** (2018).

[14] Aartsen, M. G. *et al.* Cosmic ray spectrum and composition from PeV to EeV using 3 years of data from IceTop and IceCube. *Phys. Rev. D* **100**, 082002 (2019).

[15] P. Desiati (IceCube Collaboration). *Neutrino Astrophysics and Galactic Cosmic Ray Anisotropy in IceCube*, 376–390 (2011).

[16] *et al.* (IceCube Collaboration), R. A. Observations of anisotropy in the arrival directions of galactic cosmic rays at multiple angular scales with IceCube. *The Astrophysical Journal* **740**, 16 (2011).

[17] Vink, J. Multiwavelength Signatures of Cosmic Ray Acceleration by Young Supernova Remnants. *AIP Conference Proceedings* **1085**, 169–180 (2008).

[18] Krymskii, G. F. A regular mechanism for the acceleration of charged particles on the front of a shock wave. *Akademiia Nauk SSSR Doklady* **234**, 1306–1308 (1977). [Sov. Phys. Dokl. 22, 327 (1977)].

[19] Axford, W., Leer, E. & Skadron, G. The acceleration of cosmic ray by shock waves. *Proc. 15th Int. Cosmic Ray Conf. (Plovdiv)* **11**, 132–7 (1977).

[20] Bell, A. R. The acceleration of cosmic rays in shock fronts – I. *Monthly Notices of the Royal Astronomical Society* **182**, 147–156 (1978).

[21] Bell, A. R. The acceleration of cosmic rays in shock fronts – II. *Monthly Notices of the Royal Astronomical Society* **182**, 443–455 (1978).

[22] Blandford, R. D. & Ostriker, J. P. Particle acceleration by astrophysical shocks. *Astrophysical Journal* **221**, L29–L32 (1978).

[23] Ohira, Y., Kawanaka, N. & Ioka, K. Cosmic-ray hardenings in light of AMS-02 data. *Phys. Rev. D* **93**, 083001 (2016).

[24] Hanusch, A., Liseykina, T. V., Malkov, M. & Aharonian, F. Steepening of Cosmic-Ray Spectra in Shocks with Varying Magnetic Field Direction. *The Astrophysical Journal* **885**, 11 (2019).

[25] Lipatov, A. S. *The Hybrid Multiscale Simulation Technology. An Introduction with Application to Astrophysical and Laboratory Plasmas* (Springer, Berlin, Heidelberg, 2002).

[26] Quest, K. B. Theory and simulation of collisionless parallel shocks. *Journal of Geophysical Research* **93**, 9649–9680 (1988).

[27] Caprioli, D. & Spitkovsky, A. Simulations of Ion Acceleration at Non-relativistic Shocks. II. Magnetic Field Amplification. *The Astrophysical Journal* **794**, 46 (2014).

[28] Panov, A. D. *et al.* Energy spectra of abundant nuclei of primary cosmic rays from the data of ATIC-2 experiment: Final results. *Bulletin of the Russian Academy of Sciences: Physics* **73**, 564–567 (2009).

[29] Hanusch, A., Liseykina, T. V. & Malkov, M. Acceleration of Cosmic Rays in Supernova Shocks: Elemental Selectivity of the Injection Mechanism. *The Astrophysical Journal* **872**, 108 (2019).

[30] Adriani, O. *et al.* Direct Measurement of the Cosmic-Ray Proton Spectrum from 50 GeV to 10 TeV with the Calorimetric Electron Telescope on the International Space Station. *Phys. Rev. Lett.* **122**, 181102 (2019).

[31] Reynolds, S. P. Synchrotron Radiation from Galactic Sources: What We Can Learn About Particle Acceleration. *Space Science Reviews* **99**, 177–186 (2001).

[32] Allen, G. E., Petre, R. & Gotthelf, E. V. X-Ray Synchrotron Emission from 10–100 TeV Cosmic-Ray Electrons in the Supernova Remnant SN 1006. *The Astrophysical Journal* **558**, 739–752 (2001).

[33] Ghavamian, P., Schwartz, S. J., Mitchell, J., Masters, A. & Laming, J. M. Electron-Ion Temperature Equilibration in Collisionless Shocks: The Supernova Remnant-Solar Wind Connection. *Space Science Reviews* **178**, 633–663 (2013).

[34] Krauss-Varban, D., Burgess, D. & Wu, C. S. Electron acceleration at nearly perpendicular collisionless shocks, 1, One-dimensional simulations without electron scale fluctuations. *Journal of Geophysical Research: Space Physics* **94**, 15089–15098 (1989).

[35] Guo, F. & Giacalone, J. The Effect of Large-Scale Magnetic Turbulence on the Acceleration of Electrons by Perpendicular Collisionless Shocks. *The Astrophysical Journal* **715**, 406–411 (2010).

[36] Trotta, D. & Burgess, D. Electron acceleration at quasi-perpendicular shocks in sub- and supercritical regimes: 2D and 3D simulations. *Monthly Notices of the Royal Astronomical Society* **482**, 1154–1162 (2018).

[37] Millikan, R. A. & Cameron, G. H. The Origin of the Cosmic Rays. *Phys. Rev.* **32**, 533–557 (1928).

[38] Clay, J. Results of the dutch cosmic-ray expedition 1933: Briefly communicated. *Physica* **1**, 363 – 382 (1934).

[39] Aguilar, M. *et al.* Antiproton Flux, Antiproton-to-Proton Flux Ratio, and Properties of Elementary Particle Fluxes in Primary Cosmic Rays Measured with the Alpha Magnetic Spectrometer on the International Space Station. *Phys. Rev. Lett.* **117**, 091103 (2016).

[40] Auger, P., Ehrenfest, P., Maze, R., Daudin, J. & Fréon, R. A. Extensive Cosmic-Ray Showers. *Rev. Mod. Phys.* **11**, 288–291 (1939).

[41] Longair, M. S. *High Energy Astrophysics* (Cambridge University Press, 2009).

[42] Gaches, B. A. L., Offner, S. S. R. & Bisbas, T. G. The Astrochemical Impact of Cosmic Rays in Protoclusters. I. Molecular Cloud Chemistry. *The Astrophysical Journal* **878**, 105 (2019).

[43] Padovani, M. *et al.* Impact of Low-Energy Cosmic Rays on Star Formation. *Space Science Reviews* **216** (2020).

[44] Elbert, J. W. & Sommers, P. In Search of a Source for the 320 EeV Fly's Eye Cosmic Ray. *Astrophys. J.* **441**, 151 (1995).

[45] Yoon, Y. S. *et al.* Proton and Helium Spectra from the CREAM-III Flight. *The Astrophysical Journal* **839**, 5 (2017).

[46] An, Q. *et al.* Measurement of the cosmic ray proton spectrum from 40 GeV to 100 TeV with the DAMPE satellite. *Science Advances* **5** (2019).

[47] Glasmacher, M. *et al.* The cosmic ray energy spectrum between 10^{14} and 10^{16} eV. *Astroparticle Physics* **10**, 291 – 302 (1999).

[48] Abu-Zayyad, T. *et al.* Measurement of the Cosmic-Ray Energy Spectrum and Composition from 1017to 1018.3eV Using a Hybrid Technique. *The Astrophysical Journal* **557**, 686–699 (2001).

[49] Fowler, J. *et al.* A measurement of the cosmic ray spectrum and composition at the knee. *Astroparticle Physics* **15**, 49 – 64 (2001).

[50] Apel, W. *et al.* KASCADE-Grande measurements of energy spectra for elemental groups of cosmic rays. *Astroparticle Physics* **47**, 54 – 66 (2013).

[51] Verzi, V. Measurement of the energy spectrum of ultra-high energy cosmic rays using the Pierre Auger Observatory. In *36th International Cosmic Ray Conference*, vol. 358, 450 (SISSA Medialab, 2019).

[52] Pizzolotto, C. *et al.* Looking for cosmic ray data? The ASI Cosmic Ray Database. *PoS* 227 (2017).

[53] Gebauer, I. *et al.* Measurement of anisotropies in cosmic ray arrival directions with the Alpha Magnetic Spectrometer on the ISS. *PoS* 186 (2017).

[54] Aab, A. *et al.* An Indication of Anisotropy in Arrival Directions of Ultra-high-energy Cosmic Rays through Comparison to the Flux Pattern of Extragalactic Gamma-Ray Sources. *The Astrophysical Journal* **853**, L29 (2018).

[55] Toscano, S. Observation of the anisotropy in arrival direction of cosmic rays with IceCube. *Nuclear Physics B - Proceedings Supplements* **212-213**, 201 – 206 (2011). Proceedings of the Cosmic Ray International Seminars (CRIS 2010).

[56] Butt, Y. Beyond the myth of the supernova-remnant origin of cosmic rays. *Nature* **460**, 701–704 (2009).

[57] Baade, W. & Zwicky, F. Cosmic Rays from Super-novae. *Proceedings of the National Academy of Science* **20**, 259–263 (1934).

[58] Diehl, R. *et al.* Radioactive 26Al from massive stars in the Galaxy. *Nature* **439**, 45–47 (2006).

[59] Vink, J. Supernova remnants: the X-ray perspective. *The Astronomy and Astrophysics Review* **20** (2011).

[60] Ackermann, M. *et al.* Detection of the Characteristic Pion-Decay Signature in Supernova Remnants. *Science* **339**, 807–811 (2013).

[61] Cardillo, M. Gamma-ray astronomy as a milestone in the cosmic ray origin issue. *Rendiconti Lincei. Scienze Fisiche e Naturali* **30**, 245–250 (2019).

[62] Burgess, D. & Scholer, M. *Collisionless shocks in space plasmas: structure and accelerated particles* (Cambridge University Press, 2015).

[63] Ferrière, K. M. The interstellar environment of our galaxy. *Rev. Mod. Phys.* **73**, 1031–1066 (2001).

[64] Sonett, C. P. & Abrams, I. J. The distant geomagnetic field: 3. Disorder and shocks in the magnetopause. *Journal of Geophysical Research (1896-1977)* **68**, 1233–1263 (1963).

[65] Ness, N. F., Scearce, C. S. & Seek, J. B. Initial Results of the Imp 1 Magnetic Field Experiment. *Journal of Geophysical Research (1896-1977)* **69**, 3531–3569 (1964).

[66] Balogh, A. & Treumann, R. A. *Physics of Collisionless Shocks* (Springer New York, 2013).

[67] Moiseev, S. S. & Sagdeev, R. Z. Collisionless shock waves in a plasma in a weak magnetic field. *Journal of Nuclear Energy. Part C, Plasma Physics, Accelerators, Thermonuclear Research* **5**, 43–47 (1963).

[68] Sagdeev, R. Z. Cooperative Phenomena and Shock Waves in Collisionless Plasmas. *Reviews of Plasma Physics* **4**, 23 (1966).

[69] Tidman, D. A. & Krall, N. A. *Shock waves in collisionless plasmas* (Wiley Series in Plasma Physics, New York: Wiley-Interscience, 1971).

[70] Haberberger, D. *et al.* Collisionless shocks in laser-produced plasma generate monoenergetic high-energy proton beams. *Nature Physics* **8**, 95–99 (2011).

[71] Ahmed, H. *et al.* Time-resolved characterization of the formation of a collisionless shock. *Phys. Rev. Lett.* **110**, 205001 (2013).

[72] Vauzour, B. *et al.* Relativistic high-current electron-beam stopping-power characterization in solids and plasmas: Collisional versus resistive effects. *Phys. Rev. Lett.* **109**, 255002 (2012).

[73] Liseykina, T., Dudnikova, G., Vshivkov, V. & Malkov, M. Ion-acoustic shocks with reflected ions: modelling and particle-in-cell simulations. *J. Plasma Phys.* **81** (2015).

[74] Malkov, M. A. *et al.* Ion-acoustic shocks with self-regulated ion reflection and acceleration. *Physics of Plasmas* **23**, 043105 (2016).

[75] Pusztai, I. *et al.* Low Mach-number collisionless electrostatic shocks and associated ion acceleration. *Plasma Physics and Controlled Fusion* **60**, 035004 (2018).

[76] Sulaiman, A. H. *et al.* Quasiperpendicular High Mach Number Shocks. *Phys. Rev. Lett.* **115**, 125001 (2015).

[77] Sundberg, T., Haynes, C. T., Burgess, D. & Mazelle, C. X. Ion Acceleration at the Quasi-Parallel Bow Shock: Decoding the Signature of Injection. *The Astrophysical Journal* **820**, 21 (2016).

[78] Bamba, A., Yamazaki, R., Ueno, M. & Koyama, K. Small-scale structure of the SN 1006 shock withChandraObservations. *The Astrophysical Journal* **589**, 827–837 (2003).

[79] Fox, W. *et al.* Filamentation Instability of Counterstreaming Laser-Driven Plasmas. *Phys. Rev. Lett.* **111**, 225002 (2013).

[80] Niemann, C. *et al.* Observation of collisionless shocks in a large current-free laboratory plasma. *Geophysical Research Letters* **41**, 7413–7418 (2014).

[81] Stockem, A., Fiuza, F., Bret, A., Fonseca, R. A. & Silva, L. O. Exploring the nature of collisionless shocks under laboratory conditions. *Scientific Reports* **4** (2014).

[82] Forslund, D. W. & Shonk, C. R. Formation and structure of electrostatic collisionless shocks. *Phys. Rev. Lett.* **25**, 1699–1702 (1970).

[83] Burgess, D., Hellinger, P., Gingell, I. & Trávníček, P. M. Microstructure in two- and three-dimensional hybrid simulations of perpendicular collisionless shocks. *Journal of Plasma Physics* **82**, 905820401 (2016).

[84] Bohdan, A. *et al.* Kinetic Simulations of Nonrelativistic Perpendicular Shocks of Young Supernova Remnants. I. Electron Shock-surfing Acceleration. *The Astrophysical Journal* **878**, 5 (2019).

[85] Fermi, E. On the Origin of the Cosmic Radiation. *Phys. Rev.* **75**, 1169–1174 (1949).

[86] Thornbury, A. & Drury, L. O. Power requirements for cosmic ray propagation models involving re-acceleration and a comment on second-order Fermi acceleration theory. *Monthly Notices of the Royal Astronomical Society* **442**, 3010–3012 (2014).

[87] Drury, L. O. An introduction to the theory of diffusive shock acceleration of energetic particles in tenuous plasmas. *Reports on Progress in Physics* **46**, 973–1027 (1983).

[88] Jones, F. C. & Ellison, D. C. The plasma physics of shock acceleration. *Space Science Reviews* **58**, 259–346 (1991).

[89] Schure, K. M., Bell, A. R., O'C Drury, L. & Bykov, A. M. Diffusive Shock Acceleration and Magnetic Field Amplification. *Space Science Reviews* **173**, 491–519 (2012).

[90] Malkov, M. A. & Drury, L. O. Nonlinear theory of diffusive acceleration of particles by shock waves. *Reports on Progress in Physics* **64**, 429–481 (2001).

[91] Parker, E. N. A quasi-linear model of plasma shock structure in a longitudinal magnetic field . *Journal of Nuclear Energy* **2**, 146–153 (1961).

[92] Tanaka, M., Goodrich, C. C., Winske, D. & Papadopoulos, K. A source of the backstreaming ion beams in the foreshock region. *Journal of Geophysical Research: Space Physics* **88**, 3046–3054 (1983).

[93] Decker, R. Computer modeling of test particle acceleration at oblique shocks. *Space Science Reviews* **48** (1988).

[94] Ellison, D. C., Giacalone, J., Burgess, D. & Schwartz, S. J. Simulations of particle acceleration in parallel shocks: Direct comparison between Monte Carlo and one-dimensional hybrid codes. *J. Geophys. Res.* **98**, 21085–21094 (1993).

[95] Park, J., Caprioli, D. & Spitkovsky, A. Simultaneous Acceleration of Protons and Electrons at Nonrelativistic Quasiparallel Collisionless Shocks. *Phys. Rev. Lett.* **114**, 085003 (2015).

[96] Guo, F. & Giacalone, J. The Acceleration of Thermal Protons at Parallel Collisionless Shocks: Three-Dimensional Hybrid Simulations. *The Astrophysical Journal* **773**, 158 (2013).

[97] Caprioli, D., Pop, A.-R. & Spitkovsky, A. Simulations and Theory of Ion Injection at Non-relativistic Collisionless Shocks. *Astrophys. J. Lett.* **798**, L28 (2015).

[98] Eichler, D. Particle acceleration in collisionless shocks: regulated injection and high efficiency. *The Astrophysical Journal* **229**, 419–423 (1979).

[99] Ellison, D. C., Jones, F. C., Eichler, D. *et al.* Monte Carlo simulation of collisionless shocks showing preferential acceleration of high A/Z particles. *Journal of Geophysics* **50**, 110–113 (1982).

[100] Ellison, D. C. Shock acceleration of diffuse ions at the Earth's bow shock: Acceleration efficiency and A/Z enhancement. *Journal of Geophysical Research: Space Physics* **90**, 29–38 (1985).

[101] Malkov, M. A. & Völk, H. J. Theory of ion injection at shocks. *Astronomy and Astrophys.* **300**, 605 (1995).

[102] Malkov, M. & Völk, H. Diffusive ion acceleration at shocks: The problem of injection. *Advances in Space Research* **21**, 551 – 554 (1998). Proceedings of the D0.3 Symposium of COSPAR Scientific Commission D which was held during the Thirty-first COSPAR Scientific Assembly.

[103] Malkov, M. A. Ion leakage from quasiparallel collisionless shocks: Implications for injection and shock dissipation. *Phys. Rev. E* **58**, 4911–4928 (1998).

[104] Somov, B. V. *Wave-Particle Interaction in Astrophysical Plasma*, 115–132 (Springer New York, New York, NY, 2006).

[105] Balogh, A. *et al.* (eds.) *Microphysics of Cosmic Plasmas* (Springer US, 2014).

[106] Landau, L. On the Vibrations of the Electronic Plasma. *J.Phys.(USSR)* **10**, 25–34 (1946).

[107] Tsurutani, B. T. & Lakhina, G. S. Some basic concepts of wave-particle interactions in collisionless plasmas. *Reviews of Geophysics* **35**, 491–501 (1997).

[108] Kulsrud, R. & Pearce, W. P. The Effect of Wave-Particle Interactions on the Propagation of Cosmic Rays. *The Astrophysical Journal* **156**, 445 (1969).

[109] McKenzie, J. & Völk, H. Non-linear theory of cosmic ray shocks including self-generated Alfven waves. *Astronomy and Astrophysics* **116**, 191–200 (1982).

[110] Ballet, J. X-ray synchrotron emission from supernova remnants. *Advances in Space Research* **37**, 1902 – 1908 (2006). Astrophysics.

[111] Uchiyama, Y., Aharonian, F. A., Tanaka, T., Takahashi, T. & Maeda, Y. Extremely fast acceleration of cosmic rays in a supernova remnant. *Nature* **449**, 576–578 (2007).

[112] Bell, A. R. Turbulent amplification of magnetic field and diffusive shock acceleration of cosmic rays. *Monthly Notices of the Royal Astronomical Society* **353**, 550–558 (2004).

[113] Reville, B., Kirk, J. G. & Duffy, P. A current-driven instability in parallel, relativistic shocks. *Plasma Physics and Controlled Fusion* **48**, 1741–1747 (2006).

[114] Zirakashvili, V. N., Ptuskin, V. S. & Völk, H. J. Modeling Bell's Nonresonant Cosmic-Ray Instability. *The Astrophysical Journal* **678**, 255–261 (2008).

[115] Riquelme, M. A. & Spitkovsky, A. Nonlinear Study of Bell's Cosmic Ray Current-driven Instability. *The Astrophysical Journal* **694**, 626–642 (2009).

[116] Malkov, M. A., Sagdeev, R. Z. & Diamond, P. H. Magnetic and Density Spikes in Cosmic-Ray Shock Precursors. *The Astrophysical Journal* **748**, L32 (2012).

[117] Reville, B., Kirk, J. G., Duffy, P. & O'Sullivan, S. A cosmic ray current-driven instability in partially ionised media. *A&A* **475**, 435–439 (2007).

[118] Pais, M., Pfrommer, C., Ehlert, K. & Pakmor, R. The effect of cosmic ray acceleration on supernova blast wave dynamics. *Monthly Notices of the Royal Astronomical Society* **478**, 5278–5295 (2018).

[119] Park, J., Workman, J. C., Blackman, E. G., Ren, C. & Siller, R. Particle-in-cell simulations of particle energization from low Mach number fast mode shocks. *Physics of Plasmas* **19**, 062904 (2012).

[120] Bohdan, A. *et al.* Kinetic Simulations of Nonrelativistic Perpendicular Shocks of Young Supernova Remnants. II. Influence of Shock-surfing Acceleration on Downstream Electron Spectra. *The Astrophysical Journal* **885**, 10 (2019).

[121] Scudder, J. D. *et al.* The resolved layer of a collisionless, high β, supercritical, quasi-perpendicular shock wave: 1. Rankine-Hugoniot geometry, currents, and stationarity. *Journal of Geophysical Research: Space Physics* **91**, 11019–11052 (1986).

[122] Leroy, M. M., Winske, D., Goodrich, C. C., Wu, C. S. & Papadopoulos, K. The structure of perpendicular bow shocks. *Journal of Geophysical Research: Space Physics* **87**, 5081–5094 (1982).

[123] Scholer, M. & Terasawa, T. Ion reflection and dissipation at quasi-parallel collisionless shocks. *Geophysical Research Letters* **17**, 119–122 (1990).

[124] Blanco-Cano, X., Omidi, N. & Russell, C. T. Global hybrid simulations: Foreshock waves and cavitons under radial interplanetary magnetic field geometry. *Journal of Geophysical Research: Space Physics* **114** (2009).

[125] Caprioli, D. & Spitkovsky, A. Simulations of Ion Acceleration at Non-Relativistic Shocks. i. Acceleration Efficiency. *The Astrophysical Journal* **783**, 91 (2014).

[126] Winske, D., Yin, L., Omidi, N., Karimabadi, H. & Quest, K. *Hybrid Simulation Codes: Past, Present and Future—A Tutorial*, 136–165 (Springer Berlin Heidelberg, Berlin, Heidelberg, 2003).

[127] Dendy, R. O. *Plasma Physics: An Introductory Course* (Cambridge University Press, 1995).

[128] Winske, D. Hybrid simulation codes with application to shocks and upstream waves. *Space Science Reviews* **42**, 53–66 (1985).

[129] Winske, D. & Omidi, N. Hybrid codes: Methods and applications. *4th International School for Space Simulation, Nara, Japan* (1991).

[130] Xie, H., Zhu, J. & Ma, Z. Darwin model in plasma physics revisited. *Physica Scripta* **89**, 105602 (2014).

[131] Birdsall, C. & Langdon, A. *Plasma Physics via Computer Simulation* (CRC Press, 2004).

[132] Boris, J. P. & Shanny, R. A. *Proceedings: Fourth Conference on Numerical Simulation of Plasmas, November 2, 3, 1970* (Naval Research Laboratory, 1970).

[133] Qin, H. *et al.* Why is Boris algorithm so good? *Physics of Plasmas* **20**, 084503 (2013).

[134] Matthews, A. P. Current Advance Method and Cyclic Leapfrog for 2D Multispecies Hybrid Plasma Simulations. *Journal of Computational Physics* **112**, 102 – 116 (1994).

[135] Cartwright, K., Verboncoeur, J. & Birdsall, C. Loading and Injection of Maxwellian Distributions in Particle Simulations. *Journal of Computational Physics* **162**, 483 – 513 (2000).

[136] Plimpton, S. J., Seidel, D. B., Pasik, M. F., Coats, R. S. & Montry, G. R. A load-balancing algorithm for a parallel electromagnetic particle-in-cell code. *Computer Physics Communications* **152**, 227 – 241 (2003).

[137] Germaschewski, K. *et al.* The Plasma Simulation Code: A modern particle-in-cell code with patch-based load-balancing. *Journal of Computational Physics* **318**, 305 – 326 (2016).

[138] The HDF5® Library & File Format. https://www.hdfgroup.org/solutions/hdf5/. (acessed 13.12.2019).

[139] Lembège, B. *Full Particle Electromagnetic Simulation of Collisionless Shocks*, 54–78 (Springer Berlin Heidelberg, Berlin, Heidelberg, 2003).

[140] Zatsepin, V. I. & Sokolskaya, N. V. Three component model of cosmic ray spectra from 10 GeV to 100 PeV. *A&A* **458**, 1–5 (2006).

[141] Blasi, P. & Amato, E. Diffusive propagation of cosmic rays from supernova remnants in the Galaxy. I: spectrum and chemical composition. *Journal of Cosmology and Astroparticle Physics* **2012**, 010–010 (2012).

[142] Ohira, Y. & Ioka, K. Cosmic-ray Helium Hardening. *Astrophys. J. Lett.* **729**, L13 (2011).

[143] Malkov, M. A., Diamond, P. H. & Sagdeev, R. Z. Proton-Helium Spectral Anomaly as a Signature of Cosmic Ray Accelerator. *Phys. Rev. Lett.* **108**, 081104 (2012).

[144] Vladimirov, A. E., Jóhannesson, G., Moskalenko, I. V. & Porter, T. A. Testing the Origin of High-energy Cosmic Rays. *Astrophys. J.* **752**, 68 (2012).

[145] Ellison, D. C., Jones, F. C. & Baring, M. G. Acceleration rates and injection efficiencies in oblique shocks. *Astrophys. J.* **453**, 873–882 (1995).

[146] Hao, Y., Lu, Q., Gao, X. & Wang, S. Ion Dynamics at a Rippled Quasi-Parallel Shock: 2d Hybrid Simulations. *The Astrophysical Journal* **823**, 7 (2016).

[147] Scholer, M., Kucharek, H. & Trattner, K. Injection and acceleration of energetic particles at collisionless shocks. *Advances in Space Research* **21**, 533 – 542 (1998). Proceedings of the D0.3 Symposium of COSPAR Scientific Commission D which was held during the Thirty-first COSPAR Scientific Assembly.

[148] Malkov, M. A. Analytic solution for nonlinear shock acceleration in the bohm limit. *The Astrophysical Journal* **485**, 638–654 (1997).

[149] Bykov, A. M., Ellison, D. C., Osipov, S. M. & Vladimirov, A. E. Magnetic Field Amplification in Nonlinear Diffusive Shock Acceleration Including Resonant and Non-Resonant Cosmic-Ray Driven Instabilities. *The Astrophysical Journal* **789**, 137 (2014).

[150] Burgess, D. Cyclic behavior at quasi-parallel collisionless shocks. *Geophysical Research Letters* **16**, 345–348 (1989).

[151] Burgess, D. & Scholer, M. *Microphysics of Quasi-parallel Shocks in Collisionless Plasmas*, 437–457 (Springer US, Boston, MA, 2014).

[152] Ohira, Y., Reville, B., Kirk, J. G. & Takahara, F. Two-Dimensional Particle-in-Cell Simulations of the Nonresonant, Cosmic-Ray-Driven Instability in Supernova Remnant Shocks. *The Astrophysical Journal* **698**, 445–450 (2009).

[153] Scholer, M., Kucharek, H. & Trattner, K.-H. Injection and acceleration of H^+ and He^{2+} at Earth's bow shock. *Annales Geophysicae* **17**, 583–594 (1999). Cited By :18.

[154] Burgess, D. Alpha particles in field-aligned beams upstream of the bow shock: Simulations. *Geophys. Res. Lett.* **16**, 163–166 (1989).

[155] Trattner, K. J. & Scholer, M. Diffuse alpha particles upstream of simulated quasi-parallel supercritical collisionless shocks. *Geophys. Res. Lett.* **18**, 1817–1820 (1991).

[156] Caprioli, D., Yi, D. T. & Spitkovsky, A. Chemical Enhancements in Shock-Accelerated Particles: Ab initio Simulations. *Phys. Rev. Lett.* **119**, 171101 (2017).

[157] Sugiyama, T. & Terasawa, T. A scatter-free ion acceleration process in the parallel shock. *Advances in Space Research* **24**, 73 – 76 (1999). Microscopic Processes in Space Plasmas and Their Role in Macroscale Phenomena.

[158] Sugiyama, T., Fujimoto, M. & Mukai, T. Quick ion injection and acceleration at quasi-parallel shocks. *Journal of Geophysical Research: Space Physics* **106**, 21657–21673 (2001).

[159] Sugiyama, T., Fujimoto, M. & Scholer, M. Injection of He^{2+} Ions at a parallel shock. *Advances in Space Research* **27**, 637 – 642 (2001).

[160] Hanusch, A., Liseykina, T. V. & Malkov, M. A. Chemistry of ion injection in supernova remnant shocks: hybrid simulations in the light of He/C/O data from AMS-02. *Journal of Physics: Conference Series* **1336**, 012010 (2019).

[161] Ohira, Y., Murase, K. & Yamazaki, R. Escape-limited model of cosmic-ray acceleration revisited. *A&A* **513**, A17 (2010).

[162] Telezhinsky, I., Dwarkadas, V. V. & Pohl, M. Time-dependent escape of cosmic rays from supernova remnants, and their interaction with dense media. *A&A* **541**, A153 (2012).

[163] Bell, A. R., Schure, K. M., Reville, B. & Giacinti, G. Cosmic-ray acceleration and escape from supernova remnants. *Monthly Notices of the Royal Astronomical Society* **431**, 415–429 (2013).

[164] Yang, Z., Lu, Q., Liu, Y. D. & Wang, R. Impact of Shock Front Rippling and Self-reformation on the Electron Dynamics at Low-Mach-number Shocks. *The Astrophysical Journal* **857**, 36 (2018).

[165] Kraichnan, R. H. Inertial Ranges in Two-Dimensional Turbulence. *The Physics of Fluids* **10**, 1417–1423 (1967).

[166] Caprioli, D. & Spitkovsky, A. Cosmic-Ray-induced Filamentation Instability in Collisionless Shocks. *Astrophys. J. Lett.* **765**, L20 (2013).

[167] Strong, A. W., Moskalenko, I. V. & Ptuskin, V. S. Cosmic-Ray Propagation and Interactions in the Galaxy. *Annual Review of Nuclear and Particle Science* **57**, 285–327 (2007).

[168] Aguilar, M. *et al.* Precision Measurement of the Boron to Carbon Flux Ratio in Cosmic Rays from 1.9 GV to 2.6 TV with the Alpha Magnetic Spectrometer on the International Space Station. *Phys. Rev. Lett.* **117**, 231102 (2016).

[169] Genolini, Y., Putze, A., Salati, P. & Serpico, P. D. Theoretical uncertainties in extracting cosmic-ray diffusion parameters: the boron-to-carbon ratio. *Astronomy & Astrophysics* **580**, A9 (2015).

[170] Funk, S. *High-Energy Gamma Rays from Supernova Remnants*, 1–14 (Springer International Publishing, Cham, 2016).

[171] Aharonian, F., Yang, R. & de Oña Wilhelmi, E. Massive stars as major factories of Galactic cosmic rays. *Nature Astronomy* **3**, 561–567 (2019).

[172] Gabici, S. *et al.* The origin of Galactic cosmic rays: Challenges to the standard paradigm. *International Journal of Modern Physics D* **0**, 1930022 (2019).

[173] Bell, A. R., Matthews, J. H. & Blundell, K. M. Cosmic ray acceleration by shocks: spectral steepening due to turbulent magnetic field amplification. *Monthly Notices of the Royal Astronomical Society* **488**, 2466–2472 (2019).

[174] Malkov, M. A. & Aharonian, F. A. Cosmic-ray spectrum steepening in supernova remnants. i. loss-free self-similar solution. *The Astrophysical Journal* **881**, 2 (2019).

[175] Omidi, N., Blanco-Cano, X. & Russell, C. T. Macrostructure of collisionless bow shocks: 1. Scale lengths. *Journal of Geophysical Research: Space Physics* **110** (2005).

[176] Dieckmann, M. E. *et al.* Expansion of a radially symmetric blast shell into a uniformly magnetized plasma. *Physics of Plasmas* **25**, 052108 (2018).

[177] Guo, F., Jokipii, J. R. & Kota, J. Particle Acceleration by Collisionless Shocks Containing Large-Scale Magnetic-Field Variations. *The Astrophysical Journal* **725**, 128–133 (2010).

[178] Giacalone, J. The Efficient Acceleration of Thermal Protons by Perpendicular Shocks. *The Astrophysical Journal* **628**, L37–L40 (2005).

[179] Ohira, Y. Injection to Rapid Diffusive Shock Acceleration at Perpendicular Shocks in Partially Ionized Plasmas. *The Astrophysical Journal* **827**, 36 (2016).

[180] Feldman, W. C. *et al.* Electron velocity distributions near interplantary shocks. *Journal of Geophysical Research: Space Physics* **88**, 9949–9958 (1983).

[181] Burch, J. L. *et al.* Electron-scale measurements of magnetic reconnection in space. *Science* **352** (2016).

[182] Burgess, D. *Particle Acceleration at the Earth's Bow Shock*, 161–191 (Springer Berlin Heidelberg, Berlin, Heidelberg, 2007).

[183] Amano, T. *et al.* Observational Evidence for Stochastic Shock Drift Acceleration of Electrons at the Earth's Bow Shock. *Phys. Rev. Lett.* **124**, 065101 (2020).

[184] Masters, A. *et al.* Electron acceleration to relativistic energies at a strong quasi-parallel shock wave. *Nature Physics* **9**, 164–167 (2013).

[185] Riquelme, M. A. & Spitkovsky, A. Electron Injection by Whistler Waves in Non-Relativistic Shocks. *The Astrophysical Journal* **733**, 63 (2011).

[186] Shimada, N. & Hoshino, M. Strong Electron Acceleration at High Mach Number Shock Waves: Simulation Study of Electron Dynamics. *The Astrophysical Journal* **543**, L67 (2000).

[187] Hoshino, M. & Shimada, N. Nonthermal Electrons at High Mach Number Shocks: Electron Shock Surfing Acceleration. *The Astrophysical Journal* **572**, 880 (2002).

[188] Amano, T. & Hoshino, M. Electron Shock Surfing Acceleration in Multidimensions: Two-Dimensional Particle-In-Cell Simulation of Collisionless Perpendicular Shock. *The Astrophysical Journal* **690**, 244–251 (2008).

[189] Matsumoto, Y., Amano, T. & Hoshino, M. Electron accelerations at high mach number shocks: Two-dimensional particle-in-cell simulations in various parameter regimes. *The Astrophysical Journal* **755**, 109 (2012).

[190] Matsumoto, Y., Amano, T., Kato, T. N. & Hoshino, M. Electron Surfing and Drift Accelerations in a Weibel-Dominated High-Mach-Number Shock. *Phys. Rev. Lett.* **119**, 105101 (2017).

[191] Matsukiyo, S. & Scholer, M. On reformation of quasi-perpendicular collisionless shocks. *Advances in Space Research* **38**, 57 – 63 (2006). Dynamical Processes in Critical Regions of the Heliosphere.

[192] Guo, X., Sironi, L. & Narayan, R. Electron Heating in Low Mach Number Perpendicular Shocks. II. Dependence on the Pre-shock Conditions. *The Astrophysical Journal* **858**, 95 (2018).

[193] Burgess, D. Simulations of Electron Acceleration at Collisionless Shocks: The Effects of Surface Fluctuations. *The Astrophysical Journal* **653**, 316–324 (2006).

[194] Mann, G. & Claßen, H.-T. Electron acceleration to high energies at quasi-parallel shock waves in the solar corona. *Astronomy and Astrophysics* **304**, 576 (1995).

[195] Claßen, H.-T. & Mann, G. Electron acceleration at steepened magnetic field structures in the vicinity of quasi-parallel shock waves. *Astronomy and Astrophysics* **322**, 696 (1997).

[196] Pierrard, V. & Lazar, M. Kappa Distributions: Theory and Applications in Space Plasmas. *Solar Physics* **267**, 153 (2010).

[197] Oka, M. *et al.* Electron Power-Law Spectra in Solar and Space Plasmas. *Space Science Reviews* **214**, 82 (2018).

[198] Livadiotis, G., Desai, M. I. & III, L. B. W. Generation of Kappa Distributions in Solar Wind at 1 au. *The Astrophysical Journal* **853**, 142 (2018).

[199] Wilson III, L. B. *et al.* Electron Energy Partition across Interplanetary Shocks. I. Methodology and Data Product. *The Astrophysical Journal Supplement Series* **243**, 8 (2019).

[200] Livadiotis, G. (ed.) *Kappa distributions: Theory and applications in plasmas* (Elsevier, 2017).

[201] Ghavamian, P., Laming, J. M. & Rakowski, C. E. A Physical Relationship between Electron-Proton Temperature Equilibration and Mach Number in Fast Collisionless Shocks. *The Astrophysical Journal Letters* **654**, L69 (2007).

[202] van Adelsberg, M., Heng, K., McCray, R. & Raymond, J. C. Spatial Structure and Collisionless Electron Heating in Balmer-dominated Shocks. *The Astrophysical Journal* **689**, 1089 (2008).

[203] Schwartz, S. J., Thomsen, M. F., Bame, S. J. & Stansberry, J. Electron heating and the potential jump across fast mode shocks. *Journal of Geophysical Research: Space Physics* **93**, 12923–12931 (1988).

[204] Vink, Jacco, Broersen, Sjors, Bykov, Andrei & Gabici, Stefano. On the electron-ion temperature ratio established by collisionless shocks. *Astronomy and Astrophys.* **579**, A13 (2015).

[205] Shapiro, V. & Shevchenko, V. Quasilinear theory of relaxation of an electron beam in a magnetoactive plasma. *Sov. Phys. JETP* **27**, 635 (1968).

[206] Galeev, A., Malkov, M. & Völk, H. J. Macroscopic electric fields driven by lower-hybrid turbulence and acceleration of thermal electrons in the foot of quasi-perpendicular shocks. *J. Plasma Phys.* **54**, 59 (1995).

[207] Laming, J. M., Hwang, U., Ghavamian, P. & Rakowski, C. Electron Heating, Magnetic Field Amplification, and Cosmic-Ray Precursor Length at Supernova Remnant Shocks. *The Astrophysical Journal* **790**, 11 (2014).

[208] Laming, J. M. Electron Heating at SNR Collisionless Shocks. *The Astrophysical Journal Supplement Series* **127**, 409 (2000).

[209] Cargill, P. J. & Papadopoulos, K. A mechanism for strong shock electron heating in supernova remnants. *The Astrophysical Journal Letters* **329**, L29–L32 (1988).

[210] Rakowski, C. E., Laming, J. M. & Ghavamian, P. The Heating of Thermal Electrons in Fast Collisionless Shocks: The Integral Role of Cosmic Rays. *The Astrophysical Journal* **684**, 348 (2008).

[211] Malkov, M. A., Galeev, A. A. & Völk, H. J. Electrostatic Shocks Driven by Accelerated Electrons. *International Cosmic Ray Conference* **3**, 273 (1995).

[212] Hanusch, Adrian, Liseykina, Tatyana V. & Malkov, Mikhail A. Electron energization in quasi-parallel shocks - test-particle electrons in a proton-driven turbulence. *A&A* **642**, A47 (2020).

[213] Liu, T. Z., Angelopoulos, V. & Lu, S. Relativistic electrons generated at Earth's quasi-parallel bow shock. *Science Advances* **5**, eaaw1368 (2019).

[214] Giacalone, J. & Jokipii, J. R. Magnetic Field Amplification by Shocks in Turbulent Fluids. *The Astrophysical Journal* **663**, L41–L44 (2007).

[215] Inoue, T., Yamazaki, R. & ichiro Inutsuka, S. Turbulence and Magnetic Field Amplification in Supernova Remnants: Interactions Between a Strong Shock Wave and Multiphase Interstellar Medium. *The Astrophysical Journal* **695**, 825–833 (2009).

[216] Shimoda, J. *et al.* On Cosmic-Ray Production Efficiency at Supernova Remnant Shocks Propagating Into Realistic Diffuse Interstellar Medium. *The Astrophysical Journal* **803**, 98 (2015).

[217] Ohira, Y. Simulations of Collisionless Perpendicular Shocks in Partially Ionized Plasmas. *Phys. Rev. Lett.* **111**, 245002 (2013).

[218] Ohira, Y. Magnetic Field Amplification by Collisionless Shocks in Partially Ionized Plasmas. *The Astrophysical Journal* **817**, 137 (2016).

[219] Blasi, P., Morlino, G., Bandiera, R., Amato, E. & Caprioli, D. Collisionless Shocks in a Partially Ionized Medium. I. Neutral Return Flux and its Effects on Acceleration of Test Particles. *The Astrophysical Journal* **755**, 121 (2012).

Danksagung

Eidesstattliche Versicherung

Ich versichere eidesstattlich durch eigenhändige Unterschrift, dass ich die Arbeit selbstständig und ohne Benutzung anderer als der angegebenen Hilfsmittel angefertigt habe. Alle Stellen, die wörtlich oder sinngemäß aus Veröffentlichungen entnommen sind, habe ich als solche kenntlich gemacht. Die Arbeit ist noch nicht veröffentlicht und ist in gleicher oder ähnlicher Weise noch nicht als Studienleistung zur Anerkennung oder Bewertung vorgelegt worden. Ich weiß, dass bei Abgabe einer falschen Versicherung die Prüfung als nicht bestanden zu gelten hat.

Rostock

_____   _____
(Abgabedatum)   (Vollständige Unterschrift)